Nanoscale Analysis of Natural and Artificial Magnetic Objects: Particles, Thin Films and Recording Heads

Dissertation

zur Erlangung des Grades

des Doktors der Naturwissenschaften

der Naturwissenschaftlich-Technischen Fakultät II

– Physik und Mechatronik –
der Universität des Saarlandes

von

Jiandong Wei

Saarbrücken

2009

Tag des Kolloquiums: 12th. March. 2010

Dekanin/Dekan: Univ.-Prof. Dr. Thomas Wichert

Mitglieder des
Prüfungsausschueeses:

Vorsitzender: Univ.-Prof. Dr. Rolf Pelster

Gutachter: Univ.-Prof. Dr. Uwe Hartmann
Univ.-Prof. Dr. Rainer Birringer

Akademischer Mitarbeiter: Dr. Frank Müller

To my beloved parents and big family

Contents

Zusammenfassung

Untersuchungen auf der Nanometerskala wurden durchgeführt an Magnetit-Nanopartikel-Aggregaten biologischen und künstlichen Ursprunges, epitaktischen Magnetitfilmen sowie an Festplatten-Schreibköpfen. Das Hauptziel war die präzise Charakterisierung der magnetischen Strukturen und die Untersuchung des Einflusses der magnetischen Strukturen auf die magnetischen Eigenschaften. Die wichtigsten in dieser Arbeit verwendeten Untersuchungsmethoden sind Rasterkraftmikroskopie (*atomic force microscopy*, AFM) und Magnetokraftmikroskopie (*magnetic force microscopy*, MFM). Zwei Varianten des MFM, Hochfrequenz-Magnetokraftmikroskopie (*high-frequency magnetic force microscopy*, HF-MFM) und ferromagnetische Resonanzkraftmikroskopie (*ferromagnetic resonance force microscopy*, f-MRFM) wurden verbessert bzw. für eine neue Anwendung angepasst.

Magnetit-Nanopartikel biologischen Ursprungs

Untersuchungen mit dem AFM belegen die enge Größen- und Formverteilung der vom Bakterium *Magnetospirillum gryphiswaldense* MSR-1 produzierten Magnetit-Nanopartikel. Der Einfluss der Spitzenkrümmung auf die scheinbare Partikelgröße wurde untersucht. Auf Basis geometrischer Modelle ließ sich die durchschnittliche Partikelgröße zu 35.8±5 nm bestimmen. Das Ergebnis stimmt mit einer Analyse elektronenmikroskopischer Aufnahmen überein. Anhand von MFM-Bildern ließ sich zeigen, dass die Magnetitpartikel aus einer einzelnen Domäne bestehen. In Remanenz werden einzelne Partikel leicht durch die MFM Spitze polarisiert, während in Ketten ausgerichtete Partikel durch die Spitze weniger beeinflusst werden. Der Grund hierfür liegt in der dipolaren Wechselwirkung zwischen den Partikeln. Im externen Magnetfeld waren die dipolaren Streufelder der Magnetit-Nanopartikel deutlich mit dem MFM beobachtbar. Die Dipolmomente kehrten sich bei Umpolung des äußeren

Feld um. Die Ummagnetisierung einer Zwei-Teilchen-Kette wurde mittels MFM in einem Feldbereich von ±68 mT aufgenommen. Die Änderung des magnetischen Kontrasts der Zwei-Teilchen-Kette bei Änderung des Magnetfeldes wurde aus den Bildern quantitativ abgeschätzt. Die maximale Änderung trat bei 26mT auf. Diese Feldstärke ist vergleichbar mit dem Streufeld, das von einem magnetischen Nanopartikel auf seine Nachbarn ausgeübt wird. Die Sättigung der Kette wurde bei 60mT erreicht – in Übereinstimmung mit dem Resultat, das mit einem Cantilever-Magnetometer gewonnen wurde.

Magnetitpartikel, die aus Lachsen extrahiert wurden, sind bei den typischen Lebensraumtemperaturen ferromagnetisch und AFM/MFM-Messungen zufolge in dicht gepackten Clustern angeordnet. Die Größe einzelner Magnetitpartikel liegt bei etwa 30-60nm. Die Cluster sind sphärisch und weisen einen Durchmesser von 200-300nm auf. Die Anzahl der Partikel pro Cluster liegt bei 100-200. Der MFM Kontrast ist an den Rändern der Cluster erhöht und sättigt zwischen 10 und 35mT. Einer Modellierung zufolge ist der Remanenzzustand des Clusters ein Vortex mit vernachlässigbarem Gesamtmoment. In einem Magnetfeld geht der Vortexzustand durch kohärente Rotation in einen nahezu gesättigten Zustand über. Bei niedrigen Feldern können die Cluster als Kugeln konstanter Permeabilität betrachtet werden. Sie ähneln in ihrem Verhalten superparamagnetischen Clustern, obwohl eine thermisch stabile Domänenstruktur gegeben ist. Sensormodelle, die auf einem Ensemble superparamagnetischer Partikel beruhten, sind folglich auf die untersuchten Lachsproben anwendbar.

Magnetitpartikel in verschiedenen Formen, Größen und Anordnungen wurden auf glatten Oberflächen für FMR Untersuchungen deponiert. Während der Deposition und des Trocknungsprozesses sind die Nanopartikel-Aggregate externen Magnetfeldern ausgesetzt und richten sich teilweise aus. Im trockenen Zustand wurden FMR-Messungen mit verschiedenen Magnetfeldorientierungen durchgeführt. Die Anordnung der Magnetitpartikel bestimmt die magnetostatische Wechselwirkung, welche die FMR- Spektren beeinflusst. Spektren von Magnetitpartikeln in Bakterien unter Einschluss dipolarer Wechselwirkung wurden modelliert. Die Resultate belegen,

dass die charakteristische Form eines Bakterien- FMR- Spektrums von der Kettenanordnung der Partikel herrührt. Andere Proben mit einer eher ungeordneten Anordnung der Magnetitpartikel konnten unter Annahme einer zufälligen uniaxialen Anisotropie modelliert werden. In allen Fällen reproduzieren die Modelle gut die experimentellen FMR Spektren für verschiedene Magnetfeldorientierungen. Kettenstrukturen in Proben biologischen Ursprungs können folglich durch spezifische FMR- Linienformen identifiziert werden.

Es wurde versucht, magnetisches Material in Gewebe *in situ* zu detektieren. Magnetisches Material wurde in Tilapia und in Zebrafisch nachgewiesen. Nach den Daten aus der isothermen Remanenzmagnetisierung und der Entmagnetisierung im Wechselfeld könnte das detektierte magnetische Material aus Gruppen wechselwirkender magnetischer Partikel bestehen. Das magnetische Material im Tilapia ist Magnetit, während andere metallische Eisenverbindungen im Zebrafisch nicht ausgeschlossen werden können. MFM wurde durchgeführt an Gewebeschnitten aus den Geruchslamellen des Tilapia. Eingebettetes magnetisches Material, das möglicherweise in elongierten Strukturen ausgerichtet ist, wurde gefunden. Die lokale Anordnung magnetischen Materials in biologischen Proben zu detektieren ist allerdings sehr zeitaufwändig. Gründe hierfür sind die notwendige große Anzahl von Gewebeschnitten und der langsame Scanprozess des MFM. Weiterhin wird, wie zusätzliche Experimente zeigen, die Fähigkeit des MFM, eingebettete magnetische Partikel zu entdecken, stark beeinflusst von der Rauhigkeit der Probe und der Entfernung der eingebetteten Partikel von der Oberfläche.

Ein ferromagnetisches Resonanzkraftmikroskop wurde aufgebaut mit dem Ziel der Detektion magnetischen Materials in Organismen *in situ*. Die Konstruktion des f-MRFM wurde im Detail erklärt. Der Aufbau wurde erfolgreich an einer Dünnschichtprobe aus Yttrium- Eisen- Granat getestet. Zwei Methoden wurden entwickelt um eine kontrollierbare Anzahl von Bakterien auf einen weichen Cantilever aufzubringen. Es hatte sich gezeigt, dass die Detektion tausender Bakterien durch f- MRFM schwierig ist. Wegen des Feldgradienten kann zu einer gegebenen Zeit nur ein Teil der Magnetitpartikel der Resonanzbedindung gehorchen.

Eine weitere Verbesserung des Aufbaus ist notwendig für die Detektion von Magnetit in Gewebe, insbesondere große Felder und Feldgradienten durch supraleitende Magnete, bessere Abschirmung von Störungen und Betrieb in Vakuum, um eine hohe Güte des Cantilevers zu erhalten. Die Feldmodulationsamplitude sollte auf die Größe der FRM- Linienbreite erhöht werden, um die Wirksamkeit des Doppelmodulationsverfahrens zu erhöhen.

Künstlich hergestellte Nanopartikel

Synthetische Magnetit-Nanopartikel wurden verwendet um die Strukturbildung und die magnetischen Eigenschaften von dipolar gekoppelten Partikelaggregaten zu untersuchen.

Aggregate magnetischer Nanopartikel auf Festkörperoberflächen wurden in vier verschiedenen Typen von externen Magnetfeldern erzeugt. Die Bildung von Partikelanhäufungen wird stark durch dipolare Wechselwirkungen beeinflusst. In statischen in-plane- Magnetfeldern bilden sich gestreckte Inseln mit geraden Kanten entlang der Feldachsen aus. Unregelmäßig geformte Inseln mit rauher Topographie entwickeln sich unter statischem senkrechtem Magnetfeld. Sphärische Cluster relativ geringer Größe bilden sich unter dem Einfluss rotierender in-plane- Felder. In Abwesenheit externer Magnetfelder wurden verschiedene Strukturen von individuellen Partikeln mit Durchmessern von einigen zehn Nanometern bis hin zu irregulären Clustern mit einer Größe von einigen Mikrometern beobachtet. Die typische Größe und die Höhe der Partikel hingen von der angelegten Feldstärke ab. Die experimentellen Ergebnisse stützen eindeutig Ergebnisse numerischer Simulationen von Ferrofluiden in einem zweidimensionalen diffusionslimitierten System.

Suspensionen von Magnetit- Nanopartikeln verschiedener Konzentration, Größe und Dispersionsmedien wurden untersucht. Aufgrund der dipolaren Wechselwirkung

können diese Parameter die Eigenschaften von Nanopartikel-Aggregaten signifikant modifizieren. Eine höhere Konzentration magnetischer Partikel im gleichen Dispersionsmedium führt zu einer höheren Suszeptibilität pro Gewichtseinheit magnetischen Materials. Die dipolaren Wechselwirkungen spielen eine Rolle bei der Stabilisierung der Magnetisierung gegen die Wärmebewegung, was sich als Vergrößerung der effektiven Partikelgröße in der Langevinformeln beschreiben lässt. Das Dispersionsmedium kann die Partikelmobilität und die Anordnung der Partikel erheblich beeinflussen. Dies erklärt, warum bei gleicher Konzentration in Flüssigkeiten dispergierte magnetische Partikel eine größere magnetische Suszeptibilität aufweisen als diejenigen, die in einer elastischen Matrix eingebettet sind.

Magnetit- Dünnschichtfilme

Epitaktisch gewachsene, in Luft wärmebehandelte Magnetit- Dünnschichtfilme wurden mittels MFM untersucht. Die Wärmebehandlung führt in Remanenz zu “schwachen Streifendomänen”. Kleine Normalkomponenten der Magnetisierung bilden die beobachteten Streifen, die sich unter dem Einfluss eines externen Feldes in Bubble-Domänen umwandeln. Die schwachen Streifendomänen sind die Folge einer moderaten senkrechten Anisotropie, die durch die Wärmebehandlung auftritt. Eine mögliche Ursache ist eine chemische Modifikation der Antiphasengrenzen (*anti-phase boundaries*, APB), welche die antiferromagnetische Kopplung zwischen den APB beeinflusst.

Unter Magnetfeldern von ±175 mT zeigen MFM Aufnahmen ein gestörtes Gitter von Bubbles mit entgegengesetzter Magnetisierung. Die meisten Bubbles sind gepinnt: Die Bubble-Strukturen in entgegengesetzten Feldern gehen durch inkrementelle und reversible Veränderung ineinander über. Einige wenige Bubbles entgegengesetzter Orientierung erfahren während der Feldänderung simultane Ummagnetisierung. Solche ‚dipolaren Zentren’ wurden isoliert und in kleinen Gruppen beobachtet. Bei

größerer Filmdicke ist die Auflösung des MFM hoch genug, um eine Domänenstruktur auf der Größenskala der Antiphasendomänen zu beobachten. Die abgebildete magnetische Domänenstruktur wird zumindest teilweise verursacht durch die antiferromagnetische Austauschkopplung über Antiphasengrenzen. Durch eine Reduzierung der antiferromagnetischen Kopplung durch Deaktivierung der APB ließen sich die Eigenschaften von Magnetitfilmen hinsichtlich potenzieller *spin valve*-Magnetfeldsensoren verbessern.

Hochfrequenz-Magnetokraftmikroskopie

Superscharfe MFM Spitzen können die räumliche Auflösung von HF-MFM deutlich verbessern. In der interessierenden Gapregion des Festplattenschreibkopfes können mehr Details aufgelöst werden. Zur Abbildung von Hochfrequenzfeldern mit einigen hundert MHz sind superscharfe Spitzen die beste Wahl. Allerdings lässt bei Einsatz von Standard (CoCr)- Cantileverbeschichtungen die Sensitivität des Verfahrens mit steigender Frequenz zu stark nach, um Festplatten Schreibköpfe oberhalb von 1 GHz abzubilden.

Ferritbeschichtete Cantilever weisen eine deutlich höhere HF-MFM-Empfindlichkeit als Standard CoCr- Spitzen auf. Sie erlauben die Abbildung von Schreibköpfen mit Trägerfrequenzen von 2GHz. Die geringe Koerzivität, hohe Suszeptibilität und der hohe elektrische Widerstand der Ferrite bewirken das verbesserte Hochfrequenzsignal (Ni, Zn)- ferrit- beschichteter Spitzen. Aufgrund ihrer hohen cut-off- Frequenz bringen Beschichtungen aus $Ba_3Co_2Fe_{24}O_{41}$ bessere Ergebnisse als (Ni, Zn)-Ferritbeschichtungen. Allerdings sollte die Gesamtschichtdicke reduziert werden, um eine höhere räumliche Auflösung zu erzielen. Dies setzt eine bessere Kontrolle über das Wachstum von Ferriten auf Silizium voraus. Eine Alternative wäre eine superscharfe MFM Spitze, die mittels *focused ion beam* direkt aus einer ferritbeschichteten MFM-Spitze geschnitten wird.

Chapter 1

Introduction

Motivation for the study of magnetism on the nanoscale

The understanding of magnetism on the nanoscale is an essential part of the physics of nanostructures and crucial for many modern technologies.

The continuously progressing miniaturization in information technology, electronics and automotive industries has pushed the limits of technology into the nanoscale, as exemplified by the use of nanostructured media for ultra-high density magnetic recording [Hay96, Com99, Kir00, Sel02]. Further development of novel devices, like quantum computers based on magnetic semiconductors [Len93, Orl97, Aml99] or sensors using magnetoresistance effects in metallic thin films [Bin89, Bai88, Par91], granular systems [Coe98] and magnetic oxides [Coe05], increasingly relies on techniques to fabricate nanostructured magnetic materials, which possess unique new properties distinct from bulk materials.

Fluids exhibiting unusual magnetic properties became increasingly important for industry, medicine and bio-engineering after the successful synthesis of a vast range of magnetic nanoparticles and their composites. Magnetic fluids provide a smart way to precisely control the physical properties of fluids externally by using magnetic fields. When subjected to a magnetic field, the fluid greatly increases its apparent viscosity, to the point of becoming a viscoelastic solid [Ros69]. This unique feature makes magnetic fluids perfect as liquid seals, dampers and shock absorbers being widely applied in modern automotive industries and aerospace [Bac01, Zah01]. The use of ferrofluids in so-called “hyperthermia therapy” has been developed recently as a novel

technique to treat cancer. In this technique, heat generated from the interaction between bio-compatible magnetic nanoparticles and a high-frequency magnetic field [Sne91, Mor01] is used to destroy the tumors, which are targeted by the magnetic particles. In bio-engineering, cell isolation and purification, biomolecular labelling and immobilization can be carried out efficiently via magnetic interactions [Meh97, Ede00, Pan03].

Due to a spectrum of new physics, the study of magnetism on the nanoscale is also of great fundamental interest. Numerous exciting physical phenomena become possible by reduction of at least one dimension to the nanoscale. The revolutionary event starting the era of novel magnetism is related to the discovery of Giant Magnetoresistance (GMR) in the late 1980s [Bin89]. The resistance of alternating magnetic-nonmagnetic layers changes enormously when placed in a magnetic field. Other magnificent examples of novel physics are: thickness-dependent domain wall and coercive phenomena [Fer99], interlayer exchange coupling [Bai88, Bin89, Par91], and finite-temperature magnetic ordering [Ban88].

Besides new physical phenomena, in low dimensional systems, effects of demagnetization and dipolar interaction start to play a critical role giving rise to a dramatic change in magnetic properties of materials with comparison to the bulk ones. The stability of magnetization and the effect of the dipolar interaction are of central importance for magnetic nanoparticles applied in ultra-high density magnetic recording mediums and magnetic fluids.

In this study, we will focus on one of the most important magnetic materials: magnetite.

(1) Magnetite is a magnetic material, which can be produced by a broad spectrum of organisms [Die00, Kir01]. Magnetite nanoparticles in organisms are supposed to be involved in magnetoreception for

orientation and migration, but the mechanism is poorly understood till now [Kir01, Mor04, Rit04].

(2) Because of its biocompatibility, magnetite has the unique advantage to be widely used in novel medical approaches and bio-engineering [Sne91, Meh97, Ede00, Mor01, Pan03]. Magnetite is also one of the most applied materials in magnetic fluids for industry.

(3) Due to the features of nearly full spin polarization and a very high Curie temperature (858 K) [Ver41, Yan84], magnetite thin films are promising to be a key element in future spintronic devices. Meanwhile, unusual magnetic properties are discovered in magnetite thin films [Mar96, Mar97]. These unexpected properties have been related to anti-phase boundaries (APB) existing in epitaxial films [Mar97]. However, the influence of APB on the magnetic structure and properties of magnetite films is still not very clear.

Biogenic magnetite nanoparticles are mostly characterized by scanning electron microscopy (SEM) and transmission electron microscopy (TEM) [Kir85a, Man88, Kob95, Her05]. The shape, size and crystalline structure of the biogenic magnetite nanoparticles can be precisely obtained by SEM and TEM. However, standard SEM and TEM are not sensitive to magnetic structures. Furthermore, these two imaging techniques provide only two-dimensional information. Atomic force microscopy (AFM) has been employed to characterize biogenic magnetite particles in three dimensions, and its variation, magnetic force microscopy (MFM), to investigate the magnetic properties of individual particles [Alb05, Ebe05]. The obtained AFM results are likely to deviate from those obtained by SEM or TEM, according to comparative experiments done for other nanoparticles [Ras02, Ped03]. The magnetic structures of magnetite nanoparticles obtained by MFM are dependent on the external magnetic field [Alb05], but detailed information is still lacking. In this work, a systematic AFM and MFM study has been

performed for biogenic magnetite materials in forms of individual particles, chains and clusters and also for those in tissues. Magnetite particles were extracted from magnetotactic bacteria. The AFM results of individual biogenic particles have been precisely analyzed in combination with geometric models. The magnetic structures of individual biogenic particles, chains and clusters of biogenic particles were investigated in remanence and various external magnetic fields by MFM. Based on the MFM measurements and simulation, the suitability of clusters made of magnetite nanoparticles as elements in a magnetoreceptor is discussed. In this work, magnetic material isolated from the olfactory epithelium of salmons is investigated. Though MFM has been suggested since years as an unique tool to *in situ* detect magnetic material buried in tissues, only few reports demonstrate its successful applications [Die00]. In this work, the capability of MFM to detect embedded magnetic materials is analyzed by artificial samples. Combined with global magnetic measurements, MFM has been employed to explore the magnetic material in tissue slices of the Tilapia fish. For non-destructive analysis, the special features of biogenic magnetite particles can be rapidly distinguished by ferromagnetic resonance (FMR) measurements [Wei04, Kop06a, Kop06b]. Previous FMR experiments were performed in aqueous environment. In this work, FMR measurements were carried out with samples on solid surfaces. In this way, FMR simulations can be done directly based on the dipolar interaction and more actual information on the particle arrangement and properties can be obtained.

The dipolar interaction between magnetic particles plays an important role to determine the properties of magnetic particle assemblies [Raj80, Mor99]. The interplay of the dipolar interaction and physical properties of the particle assemblies has been shown in numerous magnetic measurements, whereas the influence of dipolar interaction on the structure formation of assemblies is mostly discussed in the simulations [Hel88, Eri89, Jun95, Mor00]. Recently,

cryogenic TEM observations provided first direct proofs of the existence of dipolar chains of magnetic nanoparticles in fluids [But03]. With this technique, the particle arrangement could be fixed in an undisturbed way during the drying process. This method requires low temperature and high vacuum. Observation has also been tried with AFM, but the result is not quite convincing due to the weak dipolar interaction [Jey01, Ape05]. In this work, the dipolar interaction between magnetite nanoparticles was enhanced by external fields. The influence of the dipolar interaction on the particle arrangement is clearly revealed by the AFM results obtained under various external magnetic fields. In addition, comparative experiments have been performed to study how the particle concentration, the particle size and the dispersion medium tune the properties of systems of interacting nanoparticles.

MFM has been employed to investigate the domain structure of magnetite thin films, which is supposed to be in association with APB [Bob01, Zie02, Pan02, Bol05]. However, most of the results show magnetic domain structures with a 100-300 nm characteristic length scale, which is considerably larger than the average size of APB as mapped by TEM [Cel03, Eer03]. Furthermore, the observed magnetic structures in early studies are irregularly shaped preventing a deeper understanding of the role of APB in magnetite films. Recently, the magnetic properties of magnetite thin films were found to be changed greatly by a short-time annealing in air [Zho04]. Such a treatment results in an increase of the magnetization at 1 T by 14% and in a decrease of coercive fields by 40% with respect to as-grown samples. In this work, a MFM study was carried out for magnetite thin films annealed in air. Regular magnetic domain structures were found in such magnetite thin films. The development of the magnetic structure of magnetite films in external magnetic fields is also investigated. Based on the new observations, the influence of APB on the magnetic structures and properties of magnetite films is discussed.

Measurement techniques and method development

In terms of measurement techniques all magnetic properties can be divided into two categories: global properties (magnetization, magnetic anisotropy, transition temperature, etc.) and local properties (local distribution of magnetic moments, stray field, etc.). As the individual behavior of nanostructured material becomes more and more important, novel techniques are rapidly developed to realize accurate and precise magnetic measurements on the nanoscale.

The global properties can e.g. be characterized by alternating gradient magnetometers (AGM) [Fla88], vibration sample magnetometer (VSM) [Fon96], superconducting quantum interference device (SQUID) magnetometers [Jac64] and magneto-optical Kerr effect (MOKE) [Wil51]. Global dynamic properties are usually obtained by means of ferromagnetic resonance (FMR) [Gif46].

The local properties of nanostructured magnetic materials are investigated by techniques that were mostly invented in the age of nanotechnology.

The domain observation by Lorentz electron microscopy (LEM) [Cha84] is based on the deflection of electron beams by the Lorentz force. The unique features of LEM are high resolution, high contrast, and a direct measurement of the magnetization vector. Special sample preparation (flat and electron transparent) limits the application of this technique. As any magnetic field will change the electron beam trajectory, it is challenging to observe changes of the magnetization via external magnetic field in LEM.

Scanning electron microscopy with polarization analysis (SEMPA) collects the spin-polarized secondary electrons emitted by a magnetic sample [Ung82]. Unlike traditional SEM, SEMPA is sensitive to the polarization of secondary

electrons. SEMPA can directly detect the sample magnetization component with a high spatial resolution of 10 nm [Abr87]. The major limitation of using SEMPA is also sample preparation, as the experiment must be performed under ultra high vacuum conditions on a clean conducting surface.

By using a magnetic probe tip, the spin-polarized scanning tunneling microscope (SP-STM) is sensitive to the spin of the tunneling electrons: the conductivity of a tunnel junction depends on the relative orientation of magnetization directions in the tip and sample [Wie90]. The SP-STM realizes an ability to look directly at the interplay between magnetism and atomic structure with sub-nanometer resolution [Wie93]. However, in practice, tip preparation and the separation of artefacts from the measurements have been great challenges. The SP-STM experiment must be performed under ultra-high vacuum conditions.

X-ray photoemission electron microscopy (X-PEEM) achieves magnetic contrast using X-ray magnetic circular dichroism (XMCD) spectroscopy, in which the asymmetry in photon-absorption depends on the orientation of local magnetization relative to the optical helicity of incident circularly polarized soft x-rays [Kon88]. X-PEEM is element-specific due to the characteristic binding energies of the atomic core electrons. X-PEEM can reach a spatial resolution of less than 20 nm [And99]. The technique of X-PEEM requires an X-ray source, high vacuum conditions, clean and flat surfaces.

The sensitivity of magnetic x-ray diffraction to magnetic structures is based on interpreting the intensity and location of magnetic Bragg reflections in the reciprocal space, which contain the information on the location of magnetic atoms (atoms carrying net magnetic moments) and the spatial spin-density distribution. With new developments in x-ray optics, magnetic x-ray diffraction technique is able to produce three-dimensional maps with tens of nanometers spatial resolution [Var05]. The combination of the magnetic x-ray diffraction

technique with synchrotron sources producing picosecond-scale short x-ray pulses has lead to novel tools for research on the dynamics of magnetic systems [Dec01]. Magnetic x-ray diffraction requires an X-ray source and high vacuum conditions.

Fast imaging within nanosecond scale can be achieved by time-resolved scanning Kerr microscopy measurements [Wil51, Ele96, Cho01], allowing the dynamics of domain pattern formation to be studied. However, the spatial resolution of the magneto-optical Kerr effect technique is limited to a few hundreds of nanometers by the wavelength of the light source used.

MFM records the magnetostatic forces between a magnetic sample and a small magnetic tip (typical radius of 10-50 nm). The detailed principle of MFM will be presented in chapter 2. The advantages of this technique are: (1) it can work under ambient conditions without special sample preparation; (2) a spatial resolution down to 10 nanometers is achievable [Grü90, Kob03]. However, the interpretation of the observed magnetic contrast is not straightforward, since MFM does not directly measure the magnetization distribution but rather the stray field.

These above-mentioned techniques are complementary. A combination of these techniques is always necessary to fully understand the properties and behavior of magnetic objects on the nanoscale.

In this study, MFM is the mainly concerned technique for its applications and technical improvement. Two offsprings of MFM have been set up, namely, ferromagnetic resonance force microscopy (f-MRFM) and high-frequency magnetic force microscopy (HF-MFM).

F-MRFM combines the magnetic resonance imaging technique with MFM, which is promising to non-destructively, three-dimensionally image magnetic

materials inside an object with high sensitivity and high spatial resolution [Sid91, Sut04]. It has been successfully applied on micrometer-scale magnetic samples [Zha96, Zha98, Mid00]. In this work, f-MRFM is attempted to detect magnetite particles in magnetotactic bacteria to demonstrate its first application to complete organisms. A self-made f-MRFM is presented in detail and tested. Methods have been developed to prepare a controllable number of bacteria on cantilevers for measurements. The challenge of detecting magnetite nanoparticles in bacteria by the current f-MRFM set-up is discussed.

HF-MFM is developed as a novel approach to characterize dynamic magnetic fields from hard disk write heads [Wag91]. Detection methods of HF-MFM, like the phase detection method and the deflection method, have been continuously improved to obtain higher spatial resolution and higher sensitivity at frequencies above MHz [Wag91, Abe01, Li02]. However, conventional CoCr MFM tips limit these efforts due to their poor properties with respect to the high frequency applications. In this work, ferrites have been employed as optimal coating materials for MFM tips for better sensitivity at high frequencies above GHz. Super sharp MFM tips have been employed in order to obtain higher spatial resolution.

Structure of thesis

The structure of this thesis is as following: Chapter 2 gives a brief introduction to micromagnetism, magnetite, MFM and MRFM, which are the main objects under study. Chapter 3 demonstrates the capability of HF-MFM to characterize magnetic recording heads up to the GHz range after optimization. Chapter 4 presents the construction of a self-made f-MRFM and the attempt to apply it to *in situ* detect biogenic magnetic materials. Chapter 5 discusses the various parameters affecting magnetic properties of systems made of magnetite nanoparticles through three comparative experiments by means of AFM,

vibrating sample magnetometer and ferromagnetic resonance. Chapter 6 presents a systematic investigation of biogenic magnetite particles from bacteria and fish by AFM and MFM. MFM is also employed as a unique tool to explore magnetic material in fish tissues combined with global magnetic measurements. Chapter 7 deals with magnetite thin films, where the influence of anti-phase boundaries on the magnetic structure and “magnetic dipolar centers” are discussed based on MFM observations. Finally a summary is given in Chapter 8.

Chapter 2

Theoretical and experimental fundamentals

In this chapter, introductions to micromagnetism, magnetite, magnetic force microscopy and magnetic resonance force microscopy are given.

2.1 Micromagnetism

Intrinsic properties and atomistic theory

The magnetic moment, **m**, of solids nearly exclusively originates from the electrons in partly filled inner electron shells of transition-metal atoms. Of particular importance are the iron series transition metals (*3d* elements) and the rare-earth elements (*4f* elements) [Giv96, Blu01]. There are two sources of the atomic magnetic moment: the currents associated with the orbital motion of the electrons and the electron spin. The magnetic moments of insulating transition-metal oxides and rare-earth metals are located on well-defined atomic sites. However, in Fe, Co and Ni, as well as in many alloys, the moment is delocalized or itinerant. A large Coulomb repulsion between electrons with the same orbital occupation favors magnetic moment formation by preventing non-magnetic electron pairs. Itinerant ferromagnetism is realized by narrow electronic bands, where the intra-atomic exchange is stronger than the bandwidth-related gain in single-electron hybridization [Giv96]. In ferromagnets, the competition between magnetic coupling and thermal disorder leads to the vanishing of the spontaneous magnetization at the Curie temperature, T_C.

Anisotropy (usually characterized by the first uniaxial anisotropy constant K_1) is another physical quantity which is determined on the atomic scale [Blu01]. The anisotropy of most materials is of magnetocrystalline origin, reflecting the competition between electrostatic crystal-field interaction and spin-orbit coupling.

The crystalline field reproduces the local symmetry of the crystal and acts on the orbits of the inner-shell *d* and *f* electrons. Due to the crystalline field, the electron orbits depend on the anisotropic crystalline environment. The magnitude of the magnetocrystalline anisotropy depends on the ratio of crystal field energy and spin–orbit coupling. In *3d* atoms, the spin–orbit coupling of $\lambda \approx 50$ meV is much smaller than the crystal-field energy of $E_0 \geq 1$ eV. The magnetic anisotropy plays a major role [Giv96].

Extrinsic properties

Extrinsic properties, such as the remanence, M_r, and the coercivity, H_c, are non-equilibrium properties, i.e., related to magnetic hysteresis, and exhibit pronounced real-structure dependence. For example, the coercivity of technical iron doubles by adding 0.01 wt% of nitrogen. Such small concentrations have little effect on the intrinsic properties but lead to inhomogeneous lattice strains on a scale of many interatomic distances, affecting the propagation of magnetic domain walls and explaining the observed coercivity increase. Magnetic nanostructures exhibit a particularly rich extrinsic behavior, including phenomena such as random-anisotropy scaling [Chu86], remanence enhancement [Coe88], micromagnetic localization [Sko98], bulging-type nucleation modes [Sko99], and exchange-coupling effects [Had99, Liu00]. This large set of magnetic properties is particularly industrially relevant.

The most important micromagnetic phenomenon is the hysteresis, $\mathbf{M}(H)$, the dependence of the magnetization on the external magnetic field. Hysteresis reflects the existence of anisotropy-related metastable energy minima separated by field-dependent energy barriers. On the atomic scale, the barriers are easily overcome by thermal fluctuations, but on the macroscopic length scale the excitations are usually too weak to overcome the barriers. The overall shape of the hysteresis loop $\mathbf{M}(H)$ is determined by the structure of materials (defect structure, morphology and

history). The coercive force describes the stability of the remanent state and gives rise to the classification of magnetic materials into hard (permanent magnets), semi-hard (storage media) and soft (sensors) magnetic materials. A widely used phenomenological coercivity expression [Giv96] is

$$H_{\mathrm{c}} = \alpha_{\mathrm{K}} \frac{2K_1}{\mu_0 M_{\mathrm{s}}} - D_{\mathrm{eff}} M_{\mathrm{s}} - \Delta H(T,\eta), \tag{2.1}$$

where α_{K} is the real-structure-dependent Kronmüller parameter [Kro87, Kro88], M_{s} is the saturation magnetization, D_{eff} is a magnetostatic interaction parameter, ΔH is a fluctuation-field correction due to thermal activation, and $\eta = \mathrm{d}H/\mathrm{d}t$ is the sweep rate of the external field. Normally, ΔH is comparatively small and negligible. A key problem is to determine H_{c} from the structure of magnetic materials. In the simplest case of small particles, the exchange is sufficiently strong to ensure that $M(r)$ is constant throughout the particles. The magnetization reversal in the small particles occurs by a coherent rotation or Stoner-Wohlfarth reversal [Sto48, Aha62, Bro63]. For particles exhibiting a coherent rotation the coercive field is

$$H_{\mathrm{c}} = \frac{2K_1}{\mu_0 M_{\mathrm{s}}} + \frac{(1-3D_{eff})}{2} M_s . \tag{2.2}$$

Magnetic energy

The total energy of a ferromagnet involves exchange (E_{EX}), magnetocrystalline anisotropy (E_{MCA}), magnetostatic (E_{MS}), Zeeman (E_Z), and magnetoelastic (E_{ME}) energy terms:

$$E_{\mathrm{total}} = E_{\mathrm{EX}} + E_{\mathrm{MCA}} + E_{\mathrm{MS}} + E_Z + E_{\mathrm{ME}} . \tag{2.3}$$

The exchange energy is the energy required to rotate one atomic spin with respect to its neighbors. The exchange energy has a quantum mechanical origin and reflects an

effective spin-spin interaction resulting from symmetry rules and orbital overlap [Hub98, Blu01]:

$$E_{\mathrm{EX}} = -\sum_{i>j} 2J_{ij}\mathbf{S}_i \cdot \mathbf{S}_j , \tag{2.4}$$

where J_{ij} is the exchange integral linking the ith atom with spin $\mathbf{S}_i$ to the jth atom with spin $\mathbf{S}_j$. Using this expression and assuming interaction only between the nearest neighbors, the energy per unit volume can be determined for a specific crystal lattice (e.g. simple cubic) [Hub98, Blu01]

$$E_{\mathrm{EX}} = \int_V \frac{JS^2}{a}(\nabla \mathbf{M})^2 dr^3 = A\int_V (\nabla \mathbf{M})^2 dr^3 , \tag{2.5}$$

where $A = J S^2/a$ is the exchange parameter and a is the lattice spacing.

The magnetocrystalline anisotropy energy is the result of the interaction between the crystalline fields of the ferromagnet with spin-orbit coupling. Therefore, the energy is minimized when the magnetic moments are directed along certain axes called the easy axes, which are determined by the symmetry of the crystal. Along other directions, called the hard axes, the energy is maximized. In the case of a cubic crystal, the anisotropy energy density can be written as [Kit49, Hub98]

$$E_{\mathrm{MCA}} \approx K_1[M_1^2M_2^2 + M_1^2M_3^2 + M_2^2M_3^2] + K_2M_1^2M_2^2M_3^2 , \tag{2.6}$$

where K_i is the magnetocrystalline anisotropy constant along the i direction and M_i is the corresponding projection of the magnetization vector $\mathbf{M}$.

The magnetostatic energy arises due to the dipolar interaction between magnetic free poles. If a magnetic body of finite size is magnetized, free magnetic poles are induced, which gives rise to a demagnetizing field H_{d} and, therefore, magnetostatic energy. This energy is given by [Hub98, Blu01]

$$E_{\mathrm{MS}} = -\frac{1}{2}\mu_0 \int_V \mathbf{H}_{\mathrm{d}} \cdot \mathbf{M} dV \,. \tag{2.7}$$

In general, the demagnetizing field H_d is related to the magnetic charge density ρ_M and to the magnetization **M** through $\nabla \cdot \mathbf{H}_{\mathrm{d}} = \rho_{\mathrm{M}} = -\nabla \cdot \mathbf{M}$. For simple geometries, the demagnetizing field $\mathbf{H}_{\mathrm{d}}$ can be written in terms of a demagnetizing tensor $\widetilde{N}$ as [Hub98, Blu01]

$$\mathbf{H}_{\mathrm{d}} \approx -\widetilde{N} \cdot \mathbf{M} \,. \tag{2.8}$$

For an uniformly magnetized ellipsoid or for an infinite thin film, $\widetilde{N}$ can be calculated analytically.

The fourth energy contributor in Eq. (2.3) is the Zeeman energy, arising from the interaction of the magnetization with the external field $\mathbf{H}_{\mathrm{ext}}$. This is given by [Hub98, Blu01]

$$E_{\mathrm{Z}} = -\mu_0 \int \mathbf{H}_{\mathrm{ext}} \cdot \mathbf{M} dV \,. \tag{2.9}$$

For a uniform external field, this depends only on the magnetic moment of the sample, and not on the particular domain structure or the sample shape, unlike the magnetostatic energy term.

The fifth energy contributor in Eq. (2.3) is the magnetoelastic energy. This energy is the result of the deformation that a magnetic body experiences under the influence of a magnetic interaction. In general, this is described by an asymmetric tensor of elastic distortion as [Hub98, Blu01]

$$E_{\mathrm{ME}} \approx b_0(\varepsilon_{xx} + \varepsilon_{yy} + \varepsilon_{zz}) + b_1(\alpha_x^2 \varepsilon_{xx} + \alpha_y^2 \varepsilon_{yy} + \alpha_z^2 \varepsilon_{zz}) + b_2(\alpha_x \alpha_y \varepsilon_{xy} + \alpha_x \alpha_z \varepsilon_{xz} + \alpha_y \alpha_z \varepsilon_{yz}) \,, \tag{2.10}$$

where b_i are the magnetoelastic coefficients, α_i are the direction cosines of the

magnetization vectors relative to the coordinate system axes and ε_{ij} are the components of the strain tensor. For a majority of conventional ferromagnets, this effect is generally small and plays a less significant role as compared to the other four contributions. However, in some particular systems, the magnetoelastic energy can be large enough to strongly influence the magnetization.

Equation (2.3) could then be extended to

$$E_{\text{total}} = \int_V \{A[\nabla(\frac{\mathbf{M}}{M_s})]^2 - K_1 \frac{(\mathbf{n}\cdot\mathbf{M})^2}{M_s^2} - \frac{1}{2}\mathbf{M}\cdot\mathbf{H}_d(M) - \mathbf{M}\cdot\mathbf{H}_{\text{ext}}\} dV \,, \tag{2.11}$$

where **n** is the unit vector of the anisotropy axis.

A special case of magnetostatic interaction is the dipolar interaction. Two magnetic dipoles $\mathbf{m}_1$ and $\mathbf{m}_2$ separated by **r** have an energy equal to [Hub98, Blu01]

$$E_{\text{dipolar}} = \frac{\mu_0}{4\pi r^3}[\mathbf{m}_1\cdot\mathbf{m}_2 - \frac{3}{r^2}(\mathbf{m}_1\cdot\mathbf{r})(\mathbf{m}_2\cdot\mathbf{r})] \,, \tag{2.12}$$

which therefore depends on their separation and their degree of mutual alignment.

Magnetic domains

From the above-mentioned micromagnetic equations, one can expect the existence of magnetic domains, i.e., parts of a ferromagnet of uniform magnetization.

The main subdivisions, multi-domain (MD) and magnetically stable single domain (SD), are determined by the number of magnetic domains within one magnetic entity [Hub98]. The magnetic domains of a MD particle and a SD particle are shown in Fig. 2.1. A MD particle can have zero remanence, if the magnetization in opposite directions can cancel each other. A magnetically stable SD, on the other hand, is always magnetized to saturation and shows a remanent magnetization at room temperature.

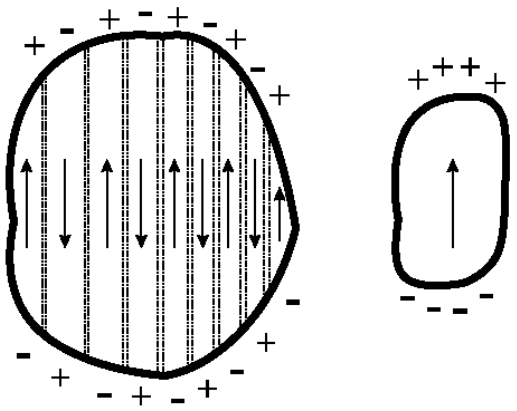

Fig. 2.1 Magnetic multi-domains (left) and stable single domain (right).

The formation of a domain wall (interface between magnetic domains) is energetically costly since the non-parallel alignment of the magnetization increases energy. Therefore, the ground state of an infinite single crystalline material would be a homogeneously magnetized single domain. However, real materials have finite boundaries, which involve a discontinuity in the magnetization, and produce surface magnetic poles that give rise to demagnetization fields. The tendency to reduce these surface demagnetization fields ultimately gives rise to the formation of multiple domains, where the reduction in demagnetization energy and the cost of forming a wall are balanced against each other. Inside the wall, a continuous variation of magnetization vector direction costs less energy than an abrupt transition. There are two main types of domain walls [Hub98]: Bloch and Néel walls (shown in Fig. 2.2). In a Bloch wall, the magnetization rotates parallel to the wall plane. In a Néel wall, the magnetization rotates in the plane perpendicular to the wall plane. Bloch walls are favored in bulk materials, but Néel walls can be preferable in thin films and in applied fields. The width of the domain wall is again determined by an energy competition. The compromise between the exchange and anisotropy energies imposes a thickness λ of the domain wall [Hub98]:

$$\lambda \propto a\sqrt{\frac{E_{\mathrm{EX}}}{E_{\mathrm{MCA}}}}, \tag{2.13}$$

where a is the lattice constant.

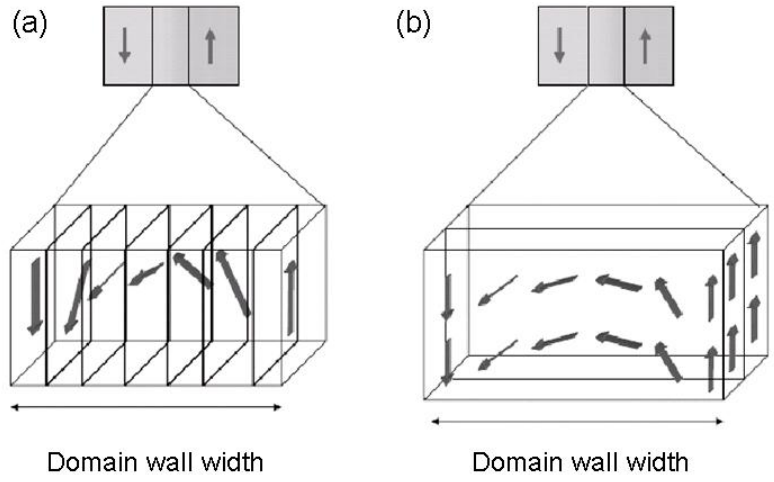

Fig. 2.2 Magnetic domain walls. (a) Bloch wall and (b) Néel wall.

When ferromagnetic particles are sufficiently small, the reduction in demagnetizing field energy does not overwhelm the energy cost of domain wall formation. As a result, the particles remain in a SD state.

Superparamagnets

The magnetic moment within a SD ferromagnetic particle can be rotated away from its low energy states by external magnetic fields or thermal activation. The characteristic energy barrier value $\Delta E \approx KV$ (K: anisotropy constant, V: particle volume) is the activation energy to flip the magnetization of a SD ferromagnetic particle between stable low-energy states. When ferromagnetic particles are small enough, ΔE is comparable to the characteristic energy of thermal fluctuation, $k_B T$. In this case, the magnetic moment within a particle is able to fluctuate rapidly. The relaxation time τ of the magnetic moment is given by [Kha91]

$$\tau = \tau_0 \exp(\frac{KV}{k_B T}), \tag{2.14}$$

where τ_0 is typically 10^{-9} s. When τ is much shorter than the experimental measuring

time *t*, the magnetic moment of a particle is zero in time average. Such a SD ferromagnetic particle is called a superparamagnet [Kha91].

2.2 Magnetite

Crystalline structure

Magnetite is the most abundant magnetic mineral on earth. Magnetite crystallizes in the inverse spinel structure, which has a face-centered cubic lattice of O^{2-} anions as its basis [Wyc82, Voo98a] with a lattice constant of 0.83963 nm. The structure formula of magnetite is $Fe^{3+}{}_A\,[Fe^{3+}\,Fe^{2+}]_B\,O^{2-}{}_4$. This formula unit indicates that one half of the ferric Fe^{3+} ions occupy 1/8 of the available tetrahedral *A* sites, whereas the other ferric ions, together with an equal amount of ferrous Fe^{2+} ions, occupy one half of the octahedral *B* sites. As shown in Fig. 2.3, the Fe_3O_4 unit cell consists of four (001) layers, each layer containing the oxygen anions and the octahedral iron ions, whereas the tetrahedral sites are located halfway between these layers. The octahedral sites containing the Fe ions are arranged in chains, all running in the <110> and <-110> directions.

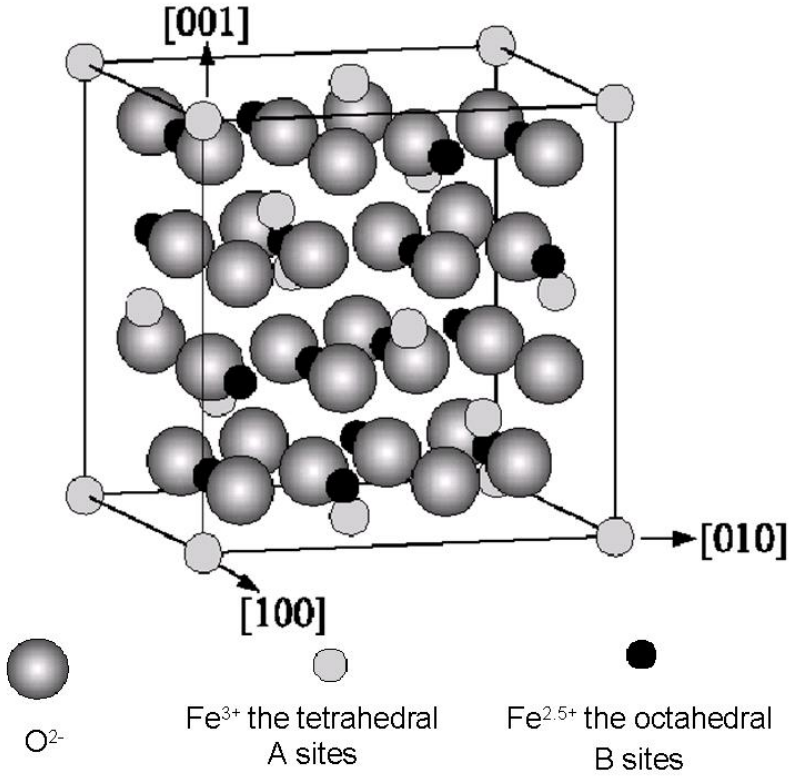

Fig. 2.3 Crystalline structure of magnetite

General properties

The high temperature phase of Fe_3O_4 is characterized by a rapid electron hopping between the Fe^{2+} and Fe^{3+} ions in the above-mentioned chains [Eva03]. Both the Fe^{2+} and Fe^{3+} ions are in the high-spin state, i.e., $S = 5/2$ and $S = 2$, respectively. However, the Fe^{2+} ions have one extra electron in an anti-bonding t_{2g} orbital as compared to Fe^{3+} ions; the electronic configurations are $3d^{6}$ and $3d^{5}$, respectively. It is this extra electron that can move around from site to site, but only if two neighboring *B* site ions are aligned ferromagnetically. Otherwise, the electron hopping would have to be accompanied by a spin-flip, making the energy barrier for hopping much higher. In bulk magnetite, the *B* site ions are indeed aligned parallel, as a result of the dominant antiferromagnetic *A*-*B* super-exchange coupling. At room temperature, the resulting conductivity is comparable to metals, i.e., ~ 200 $\Omega^{-1}m^{-1}$ [Cox95]. This high conductivity decreases by about two orders of magnitude below the Verwey temperature T_V [Ver39, Ver47]. This phase transition, occurring in bulk crystals at

around 120 K, has been the subject of massive research over the last 60 years. It is now generally believed that at T_V the electron hopping freezes out, leading to an ordered array of Fe^{2+} and Fe^{3+} ions with static charges. However, many details of the transition are still not known.

The magnetic properties of Fe_3O_4 were already known in China as long as 3000 years ago, where it was used for crude compasses. The magnetism arises from the localized magnetic moments of the Fe ions in the *A* and *B* sublattices [Eva03]. These two sublattices couple anti-ferromagnetically via superexchange, giving a net magnetic moment of ~ 4 μ_B per formula unit Fe_3O_4. In fact, this is the magnetic moment of an octahedral *B* site Fe^{2+} ion, since the moments of the Fe^{3+} ions in *A* and *B* sites are opposite and cancel each other out.

Spontaneous magnetization (or saturation magnetization), $J_s = M_s/\rho$ of magnetite is about 90 Am^2/kg [Smi59]. The Curie point (T_c) of magnetite is about 850 K (580 ^oC) [Smi59].

For magnetite films or particles, some magnetic parameters, such as the saturation magnetization, M_s, remanent saturation magnetization (maximum remament magnetization after being magnetized by pulsed magnetic fields), M_{rs}, coercive field, H_c, and coercivity of remanence (coercivity in the curve of remanent magnetization versus pulsed magnetic fields), H_{cr}, and their ratios (M_{rs}/M_s and H_{cr}/H_c) serve to define domain states. In the case of non-interacting, uniaxial SD crystals of magnetite, the theoretical values of the remanence ratio and the coercivity ratio are $M_{rs}/M_s \sim 0.5$ and $H_{cr}/H_c \sim 1$, respectively [Woh58]. For SD magnetite, these ratios are essentially temperature invariant, except in the temperature range just below T_c, where M_{rs}/M_s falls and H_{cr}/H_c rises steeply [Dum97]. In the case of MD particles, $M_{rs}/M_s \leq 0.05$ and $H_{cr}/H_c \geq 4$ [Day77]. By definition, SP particles have both M_{rs} and $H_{cr} = 0$. But particle interactions or small mixtures of SP and SD particles often occur, giving finite, albeit low, values for M_{rs} and H_{cr} [Was73, Ban85, Eva03].

The ratios M_{rs}/χ_0 and M_s/χ_0 (where χ_0 is the low field magnetic susceptibility) are also useful in distinguishing SP from non-SP behavior. In SD and MD particles of magnetite, M_s/χ_0 varies from ~ 2 to 70 mT, whereas for SP particles $M_s/\chi_0 < 0.01$ mT [Tho80]. Table 2.1 shows characteristic values and behaviors for some magnetic parameters of magnetite particles in the different domain states.

Tab. 2.1 Characteristic values and behavior for some magnetic parameters of magnetite particles depending on the domain state. From [Ban85].

Parameter	SP	SD	MD
M_{rs}/M_s	<< 0.01	~ 0.5	$\leqslant$ 0.01
H_{cr}/H_c	>> 10	~ 1.5	$\geqslant$ 4
M_{rs}/χ_0	< 0.01 mT	2 - 70 mT	2 - 70 mT
χ_0 / J_s	> 7 x 10^{-4} mT^{-1}	~ 7 x 10^{-4} mT^{-1}	~ 7 x 10^{-4} mT^{-1}
$\chi_0(T)$	large decrease	small decrease	peak at ~ 118 K
H_c/T	large increase	small increase	decrease at ~ 118 K
$J_r(T)$	large increase	small increase	decrease at ~ 118 K

The coercive force (H_c), strongly depends on particle interactions. Single SD particles show a maximum H_c whereas for SP particles H_c is zero. However, interacting SP particles behave differently [Rad73] yielding relatively large values of H_c and interacting SD particles can collectively act as MD particles, and thus act to diminish H_c values [Ban85].

Biogenic magnetite

Biogenic magnetite is the densest ($\rho \sim 5.1\times10^3$ kg/m^3), hardest, electrically best conducting ($\sigma = 2 \times10^4$ S/m), and only ferromagnetic mineral found in a wide range of living organisms [Shu75].

One proposed model for magnetite biomineralization in *Magnetospirillum* bacteria is shown in Fig. 2.4 [Sch99].

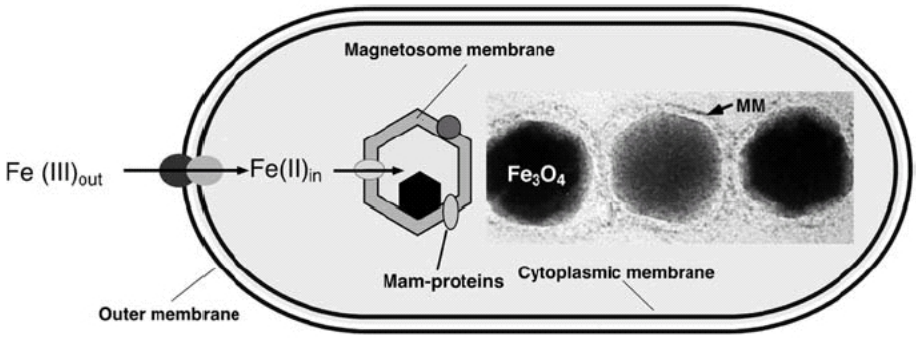

Fig. 2.4 Model for magnetite biomineralization in *Magnetospirillum* bacteria. After [Sch99].

Fe^{3+} is actively taken up by the cell, possibly via a reductive step. The iron is then thought to be reoxidized. In the last step, one-third of the Fe^{3+} ions are reduced, and magnetite is produced within the magnetosome vesicle. The magnetosome membrane contains specific Mam proteins, which are thought to have crucial functions in the accumulation of iron, nucleation of minerals, and redox and pH control.

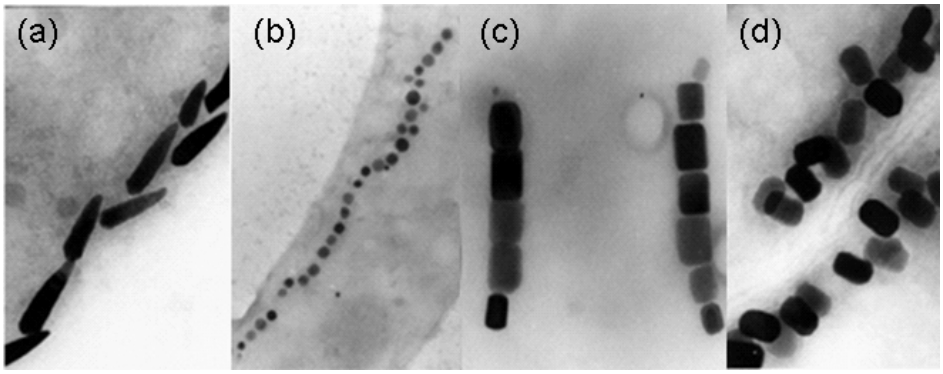

Fig. 2.5 Morphologies of magnetosomes include (a) bullet-shaped, (b) cubooctahedral and (c, d) prismatic crystals. After [Sch99].

Produced by a strictly controlled biochemical process, biogenic magnetite has three main features distinct from magnetite formed through geological processes [Kir85].

First, biogenic magnetite appears as nearly perfect crystals. Crystals are usually arranged in chains and orient their [111] direction parallel to the chain axes. Inorganically produced magnetite is usually composed of small octahedral crystals, often with lattice dislocations and other crystal defects. This feature of biogenic

magnetite serves to maximize the net magnetic moment of the particles.

Second, the morphology of biogenic magnetite is species-specific and the size distribution is narrow, as shown in Fig. 2.5. Many biogenic magnetite crystals are found in a size range from 20 to 100 nm, with shapes confining them to the magnetically stable SD. Some exceptions are crystals found in pigeons and bees with sizes of only several nanometers. Figure 2.6 presents a diagram of the grain size range of magnetite crystals discovered in some organisms well-known for their orientation behavior. Inorganic magnetite tends to have log-normal size distributions, and range from SP to MD in size.

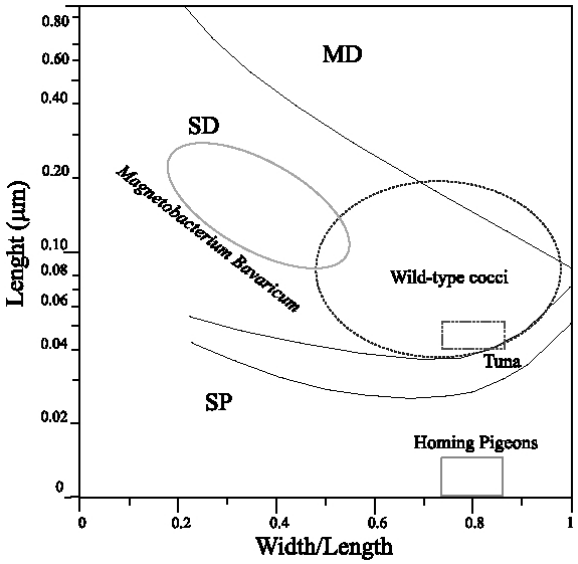

Fig. 2.6 Grain-size ranges of biogenic magnetite particles discovered in magnetotactic bacteria, tuna and homing pigeons. Modified after [Kir85a].

Third, biogenic magnetite tends to be rather pure iron oxide, with no detectable concentrations of titanium, which is typically present in geologically produced magnetite.

There are several methods for localizing, purifying, and identifying magnetite in organisms [Kir81]. If enough material is present (e.g. several milligrams), X-ray powder diffraction and/or Mössbauer absorption will suffice. Atomic absorption or

microprobe analysis can give the elemental composition of small quantities. Magnetite is the only iron oxide which is optically black as a fine powder. Thermal agitation destroys the ferromagnetic properties near 850 K, which can be measured on a sensitive magnetic balance and is usually distinctive for magnetite.

Transmission electron microscopy (TEM) is the best technique yet available to identify biogenic magnetite, since it allows for direct morphological, crystallographic and chemical characterization of minerals.

Biogenic magnetite particles in natural environments usually occur in minute quantities, often at the level of detection limit of the instruments. Many instruments used in rock magnetism fail to detect biogenic magnetite particles in the samples. A possible solution to this problem is to prepare magnetic extracts, where only the magnetic fraction of the sample is analyzed. However, in organic samples, even magnetic extracts often do not yield sufficient concentrations of material for analysis.

Magnetite thin film

Fe_3O_4 thin films are of special interest nowadays. The electron transport in Fe_3O_4 is predicted to be fully spin-polarized [Yan99] such that it is half metallic. This, combined with the very high Curie temperature, makes Fe_3O_4 thin films very promising candidates for spin-valve applications.

A spin-valve consists of a multilayer of magnetic materials, separated by a thin non-magnetic material. The current within the magnetic materials is spin-polarized. In their ground state, the magnetic materials are coupled antiferromagnetically and the resistance through the structure is high. On application of a magnetic field, the two magnetic layers align ferromagnetically, enhancing the electron transport through the structure and consequently the resistance decreases.

Due to the development of ultra-high vacuum techniques, the deposition of

high-quality thin films has spread widely. Epitaxial Fe_3O_4 films have been grown on both cleaved and polished MgO (001) substrates. Because of the common fcc oxygen sublattice, the epitaxial match between Fe_3O_4 and MgO is almost perfect. However, attempts to apply Fe_3O_4 thin films in spin-valves were not very successful up to now, as the observed magneto-resistance effect was very low [Zaa00]. Meanwhile, Fe_3O_4 thin films exhibit properties that quite deviate from the bulk ones. The magnetization does not saturate in high fields [Mar97] and ultra-thin films below 5 nm become superparamagnetic [Voo98b]. The resistivity is increased with respect to the bulk [Vee96, Eer02a] and epitaxial films show a specific magneto-resistance [Gup96, Zie00]. In addition to these new findings, a high density of so-called anti-phase boundaries (APBs) [Mar97, Voo98b, Hib99, Eer02b] was discovered in the epitaxial films. At a significant fraction of these boundaries, an anti-ferromagnetic coupling is present and the APBs thus are supposed to lead to complex magnetic structures, influencing the spin-polarized conduction electrons of Fe_3O_4. Even though the presence of APBs reduces the efficiency of Fe_3O_4 spin-valve multilayers, they also open up a new type of spin-valve application. The APBs themselves will act as a spin-valve, giving rise to magnetoresistance within a single layer. However, to fully understand the magneto-resistance properties of epitaxial Fe_3O_4 films requires intensive research on the relationship between the microstructure and the physical properties.

2.3 Magnetic force microscopy

Shortly after its invention, magnetic force microscopy (MFM) has been widely applied in the research of micromagnetism and the associated applications. To understand the principles of MFM, we first look at a class of scanning probe microscopes (SPM), from which the MFM technique is derived.

2.3.1 Scanning probe microscopy

SPM has developed into a field of powerful tools for the emerging disciplines of nanoscience and nanotechnology. The SPM field was essentially founded in 1982, with the invention of the scanning tunneling microscope at IBM Zurich by Gerd Binnig and Heinrich Rohrer [Bin82].

The main reason for the great success of SPM lies in its unsurpassed resolution in three dimensions, versatility and simple sample preparation. In Fig. 2.7, SPM is compared with other microscopic techniques used today: transmission electron microscope (TEM), scanning electron microscope (SEM), optical microscope (OM), field ion microscope (FIM), and phase contrast microscope (PCM) [Fle94]. It is worth noting that SPM unlike most other microscopes gives unique information along the additional third dimension, namely the vertical- or z direction.

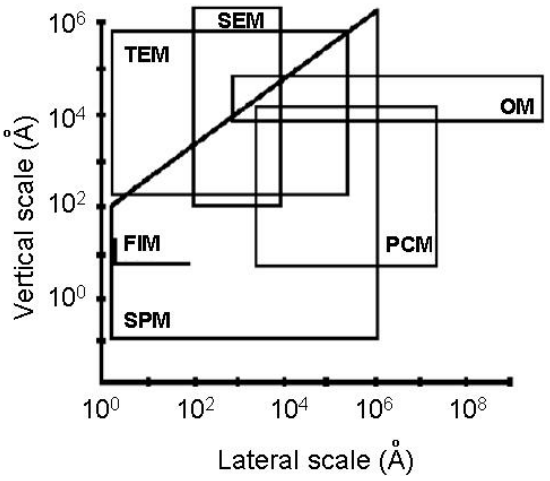

Fig. 2.7 Comparison between SPM and some other microscopic techniques. After [Fle94].

The SPMs are based on mechanically scanning a sharp tip over a sample surface. One of the most successful SPMs is the scanning force microscope (SFM). As shown in Fig. 2.8, the basic idea of the SFM is simple. A sharp tip mounted on a soft cantilever spring is employed as a force probe. The tip is brought to the sample and a piezoelectric scanner moves the sample relative to the tip in a raster pattern.

Interaction forces between the tip and sample cause some measurable change in the cantilever status, such as deflection or shift in the resonant frequency. By recording the changes, the sample-tip interaction is mapped as a function of position. The lateral resolution of SFM depends very much on the sharpness of the tip.

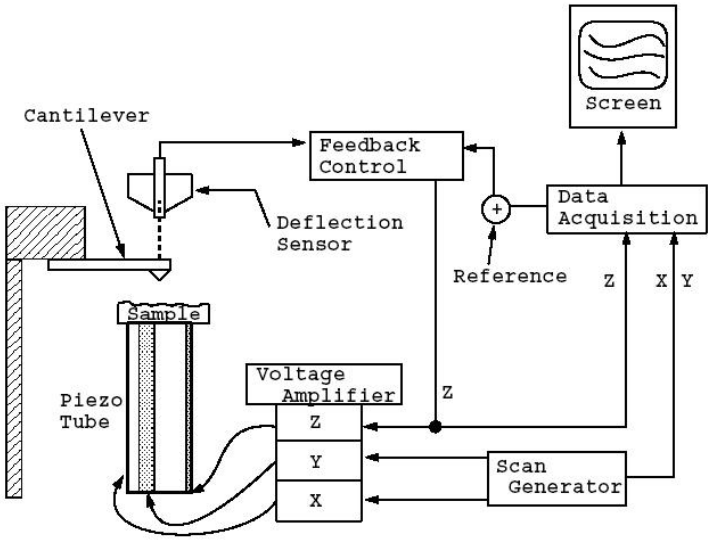

Fig. 2.8 Diagram of a scanning force microscope.

2.3.1.1 Force detection

The most straightforward method detecting the force is to measure the static deflection of the cantilever. According to Hooke's law, the deflection Δz of the cantilever is proportional to the force $F = k\Delta z$, where k is the spring constant. The minimum detectable force is determined by the sensitivity of the deflection sensor, which is typically better than 0.01 nm in a DC to 1 kHz bandwidth [Wie92]. With a spring constant of 1 N/m, a minimum detectable force F_{min} is then 10^{-11} N.

2.3.1.2 Force gradient detection

When a cantilever is driven to be oscillating, the spatially varying force modifies the effective spring constant of the cantilever according to $k_{eff} = k - \partial F/\partial z$. The change in the effective spring constant k_{eff} causes, in turn, a shift in the resonant frequency of

the cantilever. The resonant frequency of the cantilever in the presence of a force gradient is given by [Mcl87, Mar87, Erl88]

$$\omega_0' = (k_{\text{eff}} / m)^{1/2} = [(k - \partial F / \partial z) / m]^{1/2}, \tag{2.15}$$

where m is an effective mass. As $\partial F/\partial z$ is small compared to k, we get

$$\omega_0' = \omega_0[1 - (\partial F / \partial z) / 2k], \tag{2.16}$$

where ω_0 is the resonant frequency in the absence of a force gradient. The shift in resonant frequency due to the force gradient is illustrated in Fig. 2.9.

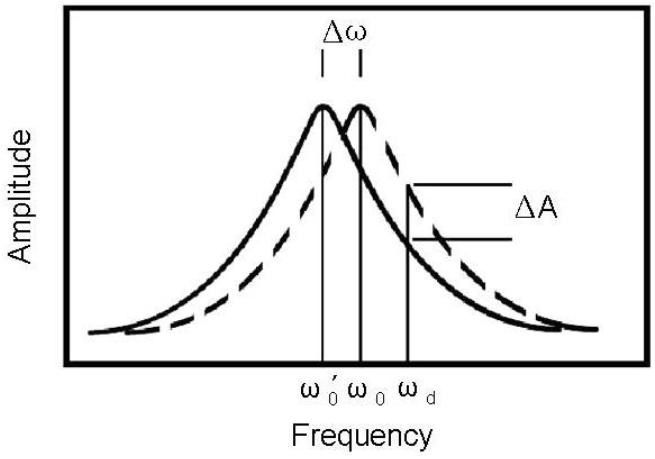

Fig. 2.9 Principle of resonance detection in non-contact force microscopy

Slope detection

In the slope detection method, the cantilever is driven by a piezoelectric bimorph at a fixed frequency, ω_d, with an amplitude typically on the order of 1-10 nm [Mar87, Erl88]. The amplitude or phase of the oscillation is measured with a position detection sensor and a lock-in amplifier. According to the usual behavior of a damped harmonic oscillator, the amplitude of the cantilever depends on the resonant frequency as following [Mar87, Grü92]:

$$A(\omega_0') = \frac{A_0(\omega_0'/\omega_d)}{[1+Q^2(\omega_d/\omega_0' - \omega_0'/\omega_d)^2]^{1/2}}, \tag{2.17}$$

where A_0 is the cantilever amplitude for $\omega_0' = \omega_d$ and Q is the quality factor of the resonance. For the maximum sensitivity to the change in ω_0', the drive frequency is chosen at $\omega_d \approx \omega_0'(1 \pm 1/2\sqrt{2}Q)$, where $A(\omega_0')$ has the steepest slope. With this choice of ω_d, the resonant frequency shift due to the force gradient results in an amplitude change of [Mar87, Grü92]

$$\Delta A = \frac{2\sqrt{3}}{9}\frac{A_0 Q}{k}\frac{\partial F}{\partial z}. \tag{2.18}$$

The oscillation phase of a damped harmonic oscillator is determined by [Mar87, Grü92]

$$\mathrm{tg}(\varphi) = \frac{\omega_0 \omega_d}{Q(\omega_d^{\,2} - \omega_0'^2)}. \tag{2.19}$$

With $\omega_d \approx \omega_0'(1 \pm 1/2\sqrt{2}Q)$, the phase shift due to the force gradient is then given by [Mar87, Grü92]

$$\Delta\varphi = -\frac{Q}{k}\frac{\partial F}{\partial Z}. \tag{2.20}$$

Frequency modulation (FM) detection

In the FM detection method, the amplitude of the oscillation is kept constant by an amplifier with automatic gain control. Variation in the force gradient causes an instantaneous change in the oscillation frequency, which can be measured by a phase locked loop, frequency counter or FM discriminator. The change in the resonant frequency of a cantilever due to the force gradient could be derived from Eq. (2.16), and re-written in the form

$$\Delta\omega_0 = -\frac{\omega_0}{2k}\frac{\partial F}{\partial z}. \tag{2.21}$$

The minimum detectable force gradient depends on the noise in the detection system. For a soft cantilever, noise from the deflection sensor is negligible compared to the thermal oscillations of the cantilever. The minimum detectable force gradient has been calculated for both the slope detection and the FM detection. Within a factor of $\sqrt{2}$, the detection limits for the two methods are the same.

For the FM detection, Albrecht et al. found [Alb91]

$$F'_{\min} = \frac{1}{A}\sqrt{\frac{4kk_BT\Delta\nu}{\omega_0 Q}}, \tag{2.22}$$

where A is the rms amplitude of the cantilever oscillation and $\Delta\nu$ is the detection bandwidth.

2.3.1.3 Position detection sensors

Optical detection is currently the most prevalent sensing method for microscopy. Among the optical methods, beam deflection [Mey88, Sar94] and interferometry [Mar87, Sar94] are commonly used due to their high sensitivity and ease of implementation. Figure 2.10 shows diagrams of the both methods.

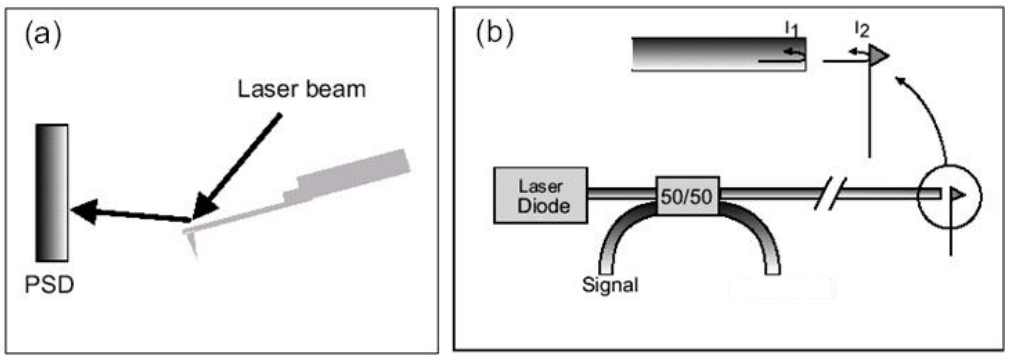

Fig. 2.10 Schematic diagrams of position detection sensors. (a) Beam deflection method and (b) optical interferometer.

In the beam deflection method, a laser beam is reflected by the end of the cantilever into a segmented photodiode array (position sensitive detector). Photodiodes produce a current that is proportional to the light falling on it. This current is converted and amplified to a useable voltage. The resulting voltages are then processed to provide a measure of deflection of the laser spot. Vertical and twisting motions of the cantilever are measured as vertical and horizontal shifts of the laser beam position.

The optical interferometer can directly measure the motion of cantilevers. Light from a diode laser is coupled into a glass fiber, which guides the laser light of wavelength λ in a monomode filter. The light is directed via a beam splitter towards the cantilever. The end surface of the fiber and the reflecting backside of the cantilever form a Fabry-Perot interferometer. The reflected light will be transferred back to the coupler side, out-coupled and measured with a photo detector. The intensity variations can be recognized with a periodicity of λ/2 and deflections can be detected with an accuracy of 0.01 nm [Mar87, Sar94].

2.3.2 Magnetic force microscopy

One of the first forces investigated using scanning force techniques was the magnetic force [Mar87, Sae87]. Consequently, magnetic force microscopy (MFM) was developed. The main advantages of MFM are: high resolution, high sensitivity and simple sample preparation.

Reviews of the principles and methods of MFM can be found in the papers of Hartmann et al. [Har91], Dahlberg [Dah95], and Grütter et al. [Grü92]. A comparison with other techniques for imaging magnetic microstructures is given in a review by Dahlberg and Proksch [Dah99].

2.3.2.1 Basic principle of MFM

The basic principle of MFM is illustrated in Fig 2.11. The magnetic stray field emanating from the surface of a sample exerts a force on a magnetic tip, which is

attached to a soft cantilever. The force (or force gradient) is measured by one of the detection methods described in the section 2.3.1. To get an image, the strength of the sample-tip interaction is mapped as a function of position on the sample.

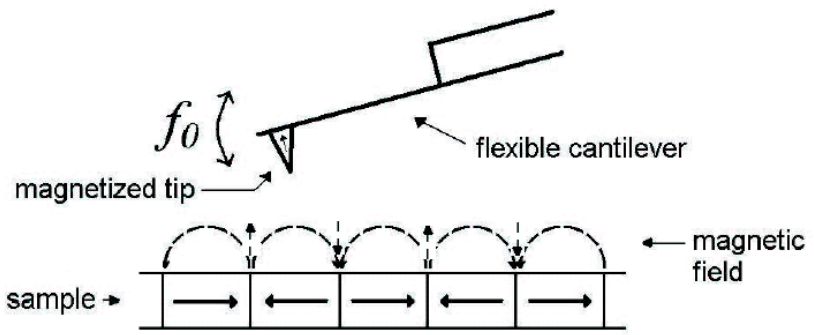

Fig. 2.11 Basic principle of MFM

For simplicity, the tip is approximated as a point dipole, the force **F** acting on the tip is then given by the gradient of the energy

$$\mathbf{F} = -\mu_0 \nabla(\mathbf{m} \cdot \mathbf{H}), \tag{2.23}$$

where **m** is the magnetic moment of the tip and **H** is the field from the sample. In the absence of electrical currents, $\nabla \times \mathbf{H} = 0$, which allows Eq. (2.23) to be written as

$$\mathbf{F} = -\mu_0 (\mathbf{m} \cdot \nabla)\mathbf{H}. \tag{2.24}$$

A real tip has an extended geometry and the total force can be calculated by integrating Eq. (2.22) over all of the dipole moments in the tip.

Since MFM responds to the magnetic field gradient, it is not a direct measure of the magnetization of samples. The detected force is strongest in regions where the magnetization is a rapidly changing function of spatial coordinates.

As pointed out by Hartmann [Har88], the mutual magnetostatic interaction may disturb the tip and sample magnetic configuration. One condition for non-destructive

MFM imaging is

$H^{T} < H^{KS}$ and $H^{S} < H^{KT}$,

where H^{T} and H^{S} are the stray fields from the tip and sample, respectively. H^{KT} and H^{KS} are the anisotropy fields of the tip and sample, respectively. Sufficiently large tip-sample separations can be chosen in order to avoid large stray fields. An alternative approach is to employ magnetic tips with thin film coatings instead of bulk magnetic tips. The stray field of the former tips falls off with distance much more rapidly than the latter ones [Har88].

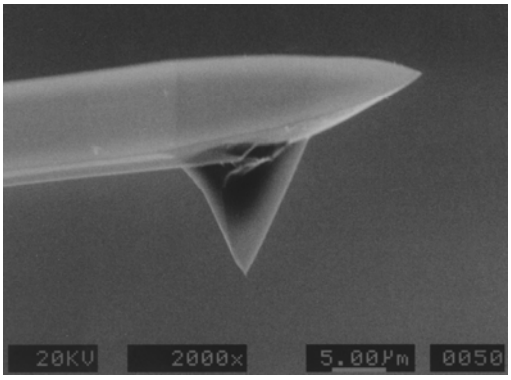

Fig. 2.12 SEM image of a tip with magnetic coating.

One tip with a magnetic coating is shown in Fig. 2.12. If not mentioned otherwise, the employed magnetic tips in this thesis are all micro-fabricated silicon probes coated with 30 nm $Co_{85}Cr_{15}$.

2.3.2.2 Theory of MFM response

The coordinate system shown in Fig. 2.13 is used in determining magnetic forces between a magnetic tip and a sample. The magnetic stray field, $\mathbf{H}(r)$, from the sample can be calculated from a given sample magnetization, $\mathbf{M}^{S}$, according to [Bro62]

$$\mathbf{H}(r) = \int_{\text{sample volume}} \left(\frac{3\mathbf{R}(\mathbf{R} \cdot \mathbf{M}^{S}(r''))}{|\mathbf{R}^{5}|} - \frac{\mathbf{M}^{S}(r'')}{|\mathbf{R}^{3}|} \right) dV'', \tag{2.25}$$

where $\mathbf{R} = r - r''$ and $\mathbf{M}^{S}(r'')$ is the sample magnetization at position r''.

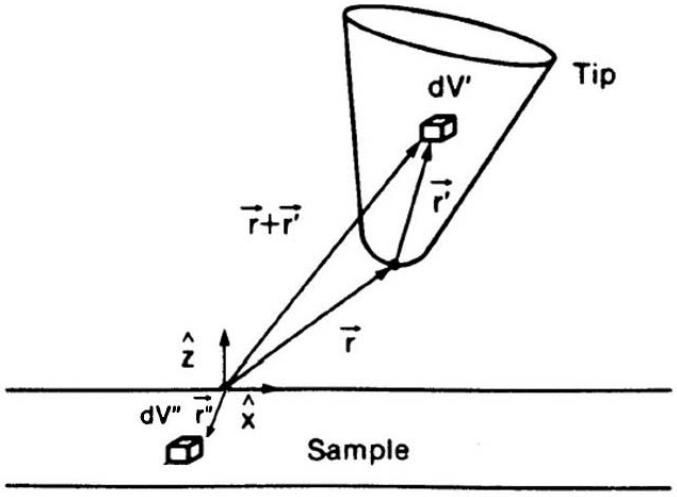

Fig. 2.13 Coordinate system used in the determination of magnetic forces. Modified after [Rug90].

In calculating and interpreting the magnetic forces, it is often assumed that the magnetizations of the tip and the sample do not affect each other, that is, $\mathbf{M}^{S}$ and $\mathbf{M}^{T}$ are constant during measurements. Once the sample stray field is known, we can calculate the force and force gradient acting on the tip [Grü92]

$$\mathbf{F}_{\text{mag}} = \int_{\text{tip volume}} \nabla_r [\mathbf{M}^{T}(r') \cdot \mathbf{H}(r + r')] dV', \tag{2.26}$$

where $\mathbf{M}^{T}(r')$ is the tip magnetization at position r' inside the tip. The force gradient along the vibrating direction of the cantilever is

$$\partial F_{\text{mag}} / \partial z = \mathbf{n} \cdot \nabla_r (\mathbf{n} \cdot \mathbf{F}_{\text{mag}}), \tag{2.27}$$

where $\mathbf{n}$ is the unit vector in the vibrating direction the cantilever.

Equations (2.26) and (2.27) show that the MFM image interpretation requires detailed information about the internal micromagnetic structure of the tip. Since this information is generally not experimentally available, image interpretation is more speculative than rigorously quantitative.

Several assumptions have been used to simplify the calculations. Among them, the "point-probe approximation" is well-known to simplify the calculation with satisfactory results in most cases. It assumes that a multipole expansion of Eq. (2.26) could be reduced to effective monopole and dipole moments of the probe. The effective monopole and dipole moments are projected into a fictitious probe of infinitesimal size with an appreciated distance away from the sample surface. With this assumption, the force acting on the probe is then given by [Har94]

$$\mathbf{F}_{\text{mag}} = \mu_0 \sum_{j=1}^{3} \mathbf{n}_j (qH_j + \sum_{k=1}^{3} m_k \frac{\partial H_k}{\partial x_k}), \tag{2.28}$$

where q and m are the probe's effective monopole and dipole moments.

The force gradient is then

$$\frac{\partial F_{\text{mag}}}{\partial z} = \mu_0 \sum_{i=1}^{3} \sum_{j=1}^{3} n_i n_j [(\frac{\partial q}{\partial x_i} + q \frac{\partial}{\partial x_i}) H_j(r) + \sum_{k=1}^{3} (\frac{\partial m_k}{\partial x_i} \frac{\partial}{\partial x_j} + m_k \frac{\partial^2}{\partial x_i \partial x_j}) H_k(r)]. \tag{2.29}$$

It is worth noting that items of $\partial q / \partial x_i$ and $\partial m_k / \partial x_i$ involved in Eq. (2.27) are "pseudo-potentials" and "pseudo-charges", respectively [Har94]. These pseudo-contributions result from the fact that the actual magnetic response of a real probe of finite size clearly depends on its position with respect to the sample surface. Eqs. (2.26) and (2.27) are the basis of contrast modeling for the MFM is operated in the static mode and in the dynamic mode, respectively.

2.3.2.2 Signal separation

As the tip-sample interaction has various origins, not only the magnetic structure of samples is reflected in standard MFM images. Sample topography is common to be mixed with the magnetic structure, if van der Waals forces between the tip and the sample change in the same way as magnetic forces.

The van der Waals force and its gradient between a spherical tip and a semi-finite flat

sample can be expressed as [Isr92]

$$F_{\text{van}} = A_{\text{H}} R^{\text{T}} / 6z^2 , \tag{2.30}$$

$$F'_{\text{van}} = -A_{\text{H}} R^{\text{T}} / 12z^3 , \tag{2.31}$$

where R^{T} is the effective radius of the tip, z is the tip-sample separation and A_{H} is the Hamaker constant with a typical value of 1 eV for metals. In case of a sharp MFM tip, the van der Waals force is usually very small for a tip-sample separation larger than 10 nm. For example, for a tip radius of 10 nm and a tip-sample separation of 50 nm, the force gradient is about 1×10^{-6} N/m. Even if the tip becomes blunt with a radius of 50 nm, the force gradient will only be 5×10^{-6} N/m.

The magnetic force (force gradient) between a magnetic tip and a sample depends on the moment distributions in both the tip and the sample as shown in Figs. 2.11 and 2.13. The gradient of magnetic forces between the tip and the sample normally decays much slower than that of van der Waals forces [Grü92]. For example, the force gradient above the center of a transition of a longitudinal recording medium with a long dipole tip is [Rug90]

$$F'_{\text{mag}} \sim \frac{1}{(a+z)^2} , \tag{2.30}$$

where z is the tip-sample separation, and a is the transition width on the order of 100 nm.

In order to ensure the magnetic force dominating the tip-sample interaction, relatively large tip-sample separations and sharp MFM tips are normally applied. For a sharp magnetic tip, the magnetic interaction can be dominant even at a small tip-sample separation of 20 nm.

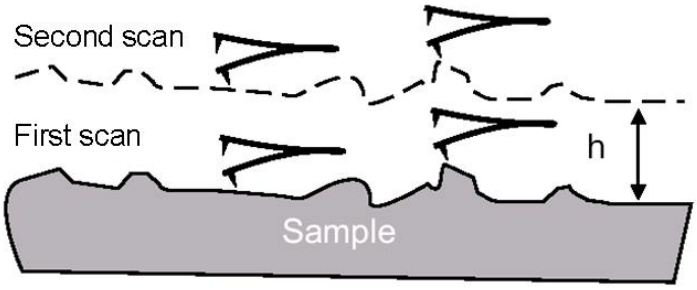

Fig. 2.14 Sketched diagram of "Tapping/lift" mode.

A very elegant method called "Tapping/Lift" mode was developed by Digital Instruments (Veeco), which allows a clear separation of magnetic signals without sacrificing the signal intensity [Zho93]. As shown in Fig. 2.14, the sample is scanned twice: the sample's topography is obtained in the first scan, where the tip is made to strike the surface on each oscillation (the tapping mode) and the repulsive van der Waals force is dominating. Magnetic contrast is subsequently obtained in the second scan at a constant height *h* above the sample surface (the life mode). In the second scan, the van der Waals force for each measuring point is almost constant. The magnetic contrast is then nicely separated from the topography.

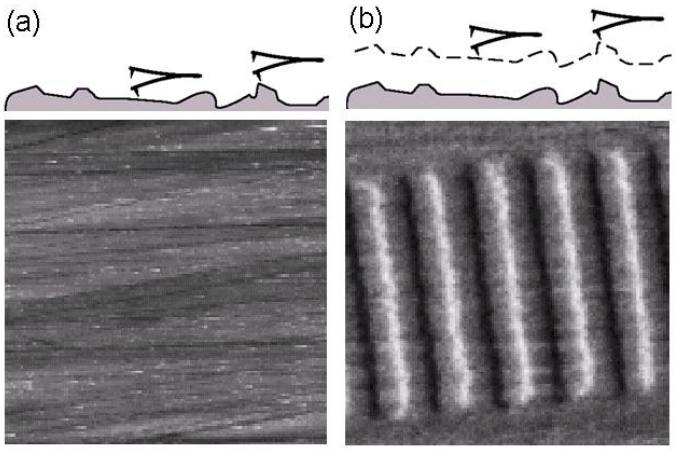

Fig. 2.15 (a) Topographic and (b) magnetic structures of a hard disk.

Fig. 2.15 shows the topographic and magnetic images of a hard disk obtained by the "Tapping/lift" method, where topographic and magnetic signals are clearly separated.

In this work, a multimode SPM (including SFM, namely, AFM and MFM modes) from Digital Instruments (Veeco) is employed. MFM is performed in the "Tapping/lift" mode with a typical lift height of 30 nm.

2.4 Magnetic resonance force microscopy

The concept of magnetic resonance force microscopy (MRFM) was first proposed by Sidles in 1991 [Sid91], by which magnetic resonance spin signals are detected mechanically via force detection. The idea was soon proved to be very promising by Rugar et al in 1992 [Rug92]. They first demonstrated the capability of MRFM by detecting the electron spin resonance signal from a 30 ng crystal of diphenylpicrylhydrazil. Two years later, Rugar et al. reported the mechanical detection of H^1 nuclear magnetic resonance in 12 ng ammonium nitrate [Rug94]. Later on, Zhang et al. mechanically detected ferromagnetic resonance signals in yttrium iron garnet [Zha96]. According to the types of detected magnetic resonance, MRFM is classified as e-MRFM (electron spin resonance), n-MRFM (nuclear magnetic resonance) or f-MRFM (ferromagnetic resonance).

Significant progress has been made in many aspects in the following years: applying MRFM at low temperature and in high vacuum [Wag97], developing ultra-soft cantilevers [Sto97] and creating huge gradient fields by small permanent magnets [Bru98]. With continuous optimization, a historic milestone was made by the successful detection of one single electron spin in Ruger's group [Rug04]. The MRFM had a strong impact in a broad range of fields, including spin electronics [Rug04], quantum computers [Ber00] and microscopic ferromagnets [Kle03].

The principle of MRFM

A sketch of MRFM is shown in Fig. 2.16. From the sketch, MRFM can be recognized as an extension of MFM. Both techniques are based on the magnetic interactions of a

magnetic tip and a sample, and the high force sensitivity is gained from the micro-mechanical resonator (cantilever). The detected force is $\mathbf{F} = -\mu_0(\mathbf{m}\cdot\nabla)\mathbf{H}_{\text{probe}}$, the same as in Eq. (2.22). In MFM, the magnetic moment of the tip is constant and the gradient field from the specimen is detected. While in MRFM, the magnetic gradient field provide by a small permanent magnet is constant and the change in the net magnetic moment of the sample due to resonance is detected.

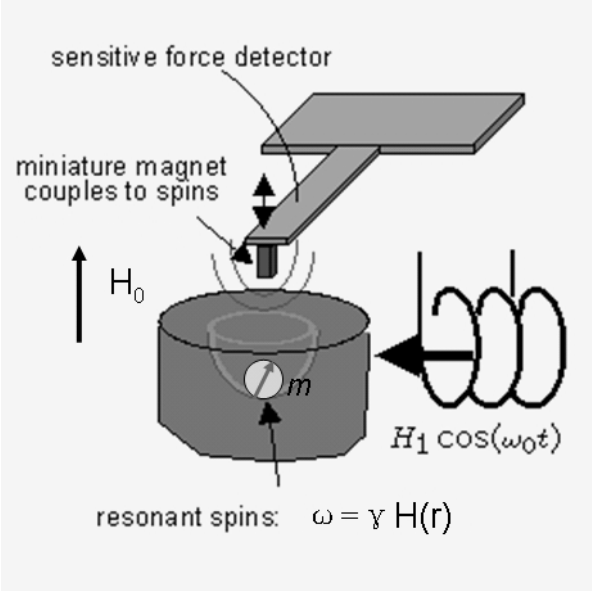

Fig. 2.16 Principle of MRFM

In order to get the sample resonating, the sample is immersed both in an external magnetic field H_0 and a high frequency ac field H_1 normal to the external field.

The steady-state vertical (along the tip vibration direction) magnetization is given by [Gar55]

$$M = \chi_0 H_0[1 - \frac{2\gamma^2 H_1^2 \tau^2}{4 + 4(\gamma H_0 - \omega)^2 \tau^2 + \gamma^2 H_0^2 \tau^2}], \tag{2.31}$$

where χ_0 is the susceptibility, γ is the gyromagnetic ratio, ω is the angular frequency of the ac field, τ is the relaxation time. M is a linear function of H_0 except in the

vicinity of resonance. When the condition for magnetic resonance is met (see Eq. (2.37)), the vertical magnetization is sharply suppressed.

As the spin resonant frequency is usually much higher than the resonant frequency of the employed cantilever, modulation techniques are required to bringing the spins in the sample in and out of resonance [Rug92, Bru95] at the resonant frequency of the cantilever. From Eq. (2.31), an oscillating M at the modulation frequency can be created by modulating the amplitude of $H_{1,}$ the frequency of $H_{1,}$ or modulating H_0. However, direct modulation of these parameters at the resonant frequency of the cantilever always creates large and even unacceptable spurious vibration in the cantilever (probably due to eddy currents or electrostatic force effects) [Rug92]. In order to eliminate modulation noise, an excitation scheme called the "anharmonic modulation technique" was developed [Bru95]. In this scheme, two parameters determining the sample magnetization are simultaneously modulated at two different frequencies. The difference or the sum of these two different frequencies is equal to the resonant frequency of the cantilevers. The individual modulations produce no modulation noise because they are off-resonance. To be more specific, modulating the external magnetic field

$$H_{\text{ext}} = H_0 + H_{\text{mod}}^0 \cos(\omega_{\text{ext}} t) \tag{2.32}$$

and further modulating the ac field

$$H_{\text{ac}} = H_1 + H_{\text{mod}}^1 \cos(\omega_{\text{ac}} t) \tag{2.33}$$

will lead via mixing to

$$M(t) = M[H_{\text{ext}}(t), H_{\text{ac}}(t)] = M^0 + M^{\text{res}} \cos\omega_0 t + \text{off-resonant harmonics,} \tag{2.34}$$

where $\omega_0 = \omega_{\text{ext}} \pm \omega_{\text{ac}}$ is the resonant frequency of the cantilever.

If thermal excitation of the cantilever is the only noise source, the signal-to-noise ratio

(SNR) for MRFM is [Sid95]

$$\text{SNR} = MV\nabla H\sqrt{\frac{Q\omega_0}{8kk_BT\Delta\nu}}, \tag{2.35}$$

where M is the rms signal of the magnetization, V the involved volume, Q the quality factor of the cantilever, ω_0 the resonant frequency of the cantilever, k the spring constant of the cantilever, k_B the Boltzmann constant, T the temperature, and $\Delta\nu$ the detection bandwidth.

When the SNR equals 1, the minimum detectable magnetic moment is obtained

$$m_{\min} = (MV)_{\min} = \sqrt{\frac{8kk_BT\Delta\nu}{Q\omega_0}}/\nabla H\,. \tag{2.36}$$

From Eq. (2.36), the high sensitivity of MRFM could be realized by using low temperature, high field gradients and sensitive cantilevers. For the following parameters, which are believed to be realizable (T = 10 mK, k = 0.01 N/m, Q = 10^5, ∇H = 10^8 T/m, ω_0 = 100 kHz and $\Delta\nu$ = 0.1 Hz), the magnetic moment sensitivity will be 1.7×10^{-27} Am^2, already lower than the magnetic moment of a single proton of 1.4×10^{-26} Am^2. Though achieving this level of sensitivity is a challenge, the single-electron-spin sensitivity has been realized as mentioned above.

The high sensitivity is not the only advantage to MRFM. Due to the gradient field, MRFM is also able to distinguish magnetic resonance signals arising from different locations in the sample, in the same way as the magnetic resonance imaging (MRI) technique. When magnetic moments in the sample are resonant, this should satisfy the condition

$$\omega = \gamma H(r)\,, \tag{2.37}$$

where ω is the frequency of the applied ac field, γ is the gyromagnetic ratio of the sample material, and $H(r)$ is the total magnetic field at the investigated location. In

MRFM experiments, if the frequency of the ac field is kept constant, the resonance only occurs within the region where the local magnetic field meets the resonance condition. The resonance region is defined by the gradient field from the magnet, and in fact normally looks like a bowl-shape slice as shown in Fig. 2.17 [Sid95]. Upon sweeping the strength of the external magnetic field, the position of the resonance slice will be moved accordingly and also magnetic resonance signals in other regions will be detected. By knowing the values of the external magnetic field and the field gradient, the locations of the magnetic resonance signals are thus determined. As the resonance slice can penetrate into the samples, it implies that MRFM can provide subsurface information.

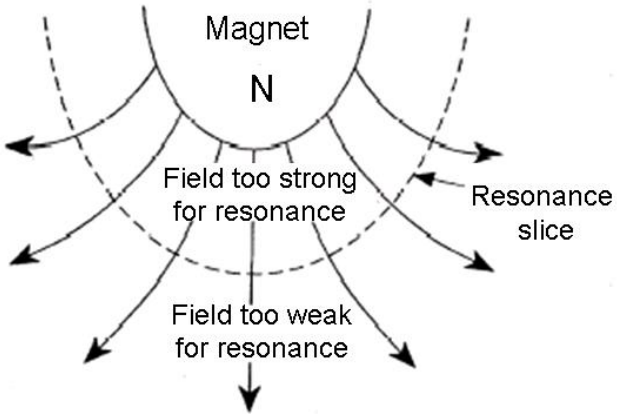

Fig. 2.17 The resonance slice in MRFM

However, in case of f-MRFM, the location of the magnetic resonance signals can not be determined straightforwardly. Due to the strong exchange coupling of the spins in ferromagnetic substances, the resonant frequency is not a local function of the applied magnetic field. In order to resolve this problem, a small magnetic probe should be applied to create a strong local magnetic inhomogeneity, by which a local modification of magnetic resonance modes can be accomplished and recognized by f-MRFM [Mid00]. Thus, with a local modification field, spatially resolved f-MRFM measurements are also possible.

Chapter 3

Characterization of hard disk write heads by high-frequency magnetic force microscopy

In this chapter, high-frequency MFM (HF-MFM), an extension of the standard MFM, is employed to visualize the high-frequency stray fields of hard disk write heads. Special effort is devoted to develop magnetic tips, which enable the observation of stray fields at high frequencies up to 2 GHz. However, no magnetic tip is found to be ideal in order to achieve both high spatial resolution and high sensitivity in the GHz range. Further optimization steps of the HF-MFM technique are suggested.

3.1 Introduction

With the growth of the storage density of magnetic recording, the hard disk bit size is becoming smaller, the data rate is getting higher, and the writing frequency is approaching the GHz range. Measuring dynamics of magnetic stray fields in the submicron region has played an important role in further developing write heads [Li03, Abe04, Kob06]. Electron beam tomography [Mat90, Shi92] and magneto-optical methods [Cor88, Fre96, Liu96, Fre97] have been employed for this purpose. The electron beam tomography should be performed in vacuum. The magneto-optical methods provide only indirect observations and the spatial resolution is limited [Abe02]. HF-MFM, as an extension of the standard MFM, was proposed to observe the time-averaged high frequency magnetic stray fields emanating from hard disk write poles [Wag91, Pro99, Qia99]. The striking feature of this method is that the experiment can be carried out with minor modifications to a conventional MFM system. The force interaction, which is directly induced by the high frequency magnetic field, is detectable under ambient conditions. The spatial resolution of HF-MFM is expected to be as high as that of MFM. Up to now, HF-MFM is

employed as a quasi-commercial investigation tool for hard disk write heads [Abe01, Abe02, Abe04].

There are basically two methods in the literature: the direct phase detection method [Wag91] and the amplitude-modulation method [Pro99]. In the direct phase detection method, the cantilever is oscillated solely by the piezoelectric element as in conventional MFM. The time-averaged effective force acting on the magnetic tip is $F_{\text{eff}} = \mu_0 (\partial/\partial z) < \mathbf{m}_t(t) \cdot \mathbf{H}(t) >$, where μ_0 is the permeability of free space, $\mathbf{m}_t(t)$ is the magnetic moment of the MFM tip, and $\mathbf{H}(t)$ is the high-frequency magnetic field of the write head, and < > denotes the time average. The phase shift of the cantilever oscillation is proportional to the effective force gradient. As the detected force is time-averaged, the optimal conditions for the high frequency field evaluation by this method are obtained if the tip magnetic moment can follow the write head field with constant phase shift of values near either 0 or π. Otherwise, there is no well-defined time-averaged effective force. In practice, the optimal conditions are not always met. Thus, the direct phase detection method is not reliable. In the amplitude-modulation method, an amplitude-modulated high frequency current is applied to the write head. The modulation frequency ω_m is selected so to fall into the cantilever excitation bandwidth. The piezoelectric element is switched off, and the driving force is solely from the high-frequency magnetic field. In this way, a cantilever oscillation is produced and the amplitude of the oscillation does not depend on the phase shift between $\mathbf{m}_t(t)$ and $\mathbf{H}(t)$. Its amplitude is proportional to the amplitude of the high frequency magnetic field [Pro99, Li02]. The reliability of HF-MFM is improved by the amplitude-modulation method. Its spatial resolution is poor as compared to the phase detection method. The reason is that the force field $\propto \partial H/\partial z$ measured by the amplitude detection method (see Eq. (3.1)) is not as sharp as the gradient field $\propto \partial^2 H/\partial z^2$ measured by the phase detection method [Wag91, Li02]. Recently, a dual-vibrational method [Li02] was introduced, which is in fact a modified phase detection method. In the dual-vibrational method, the cantilever is driven by both the piezoelectric element and the amplitude-modulated high-frequency stray field. By

taking advantages of the former two methods, the dual-vibrational method can provide high spatial resolution and high sensitivity to magnetic fields of high frequencies [Li02, Kob06]. In this study, measurements are performed by the dual-vibrational method.

Apart from the detection methods, the magnetic coating of the MFM tips is essential in order to achieve maximum MFM signals at high frequencies. Eddy currents, hysteresis loss and reduced permeability of magnetic coatings in the high frequency regime (> MHz) may considerably decrease the interaction between the MFM tip and the high frequency field. The magnetic coating of the "standard" MFM cantilevers employed in the HF-MFM measurements is mainly CoCr [Pro99, Abe01, Abe02, Li02, Abe04], partly also CoPtCr [Har99, Wic00]. However, the magnetic properties of these magnetic materials are not optimal for applications at high frequencies. In order to improve the sensitivity of HF-MFM, the employed magnetic coating should exhibit high electrical resistivity and high permeability at high frequencies. Ferrites are suitable materials working in the high frequency range as they have been employed in write heads to generate strong high frequency magnetic fields [Ash97]. In order to figure out the suitability of ferrite coatings for the cantilevers used in HF-MFM, we employ the Z-type hexaferrite $Ba_3Co_2Fe_{24}O_{41}$ (BCFO) and the spinell-type $NiZnFe_2O_4$ [(Ni, Zn) ferrite] as test materials. The bulk BCFO material has a very high cut-off frequency of about 2 GHz. Though the bulk (Ni, Zn) ferrite has a relatively low cut-off frequency about 300 MHz [Gol90], (Ni, Zn) ferrite thin film exhibits a considerably increased cut-off frequency of 1 GHz [Mat02].

In order to improve the spatial resolution of HF-MFM, the advanced tips developed for MFM within the ASPRINT (Advanced scanning probes for innovative nanoscience and technology) project will be considered for HF-MFM. The spatial resolution of MFM is related to both the magnetized part of the probe that is actually exposed to the sample stray field and to the probe–sample distance. In order to improve the resolution, it is necessary to decrease the magnetically sensitive part of

the probe to the possibly smallest size and to operate the probe in close proximity to the sample surface. Super sharp MFM tips prepared by focused ion beam (FIB) can provide a very small apex radius. They are employed for the optimization of HF-MFM in this study.

3.2 Preparation and characterization of magnetic tips

3.2.1 Super sharp MFM tips

As a starting point to prepare advanced MFM tips, the micro-machined Si cantilevers were employed. By means of FIB milling, high-aspect-ratio tips were fabricated first, like needle-type tips in Ref. [Har99]. In order to improve the stability of high-aspect-ratio tips, the shape of the tip shaft was changed slightly. In another approach so-called super sharp tips were coated with a 10 nm thick CoCr coating by evaporation. A relative thin coating was chosen in order to keep the tip sharpness. Super sharp tips prepared by Dr. Sulzbach from Nanoworld service GmbH were employed in this work [Kob08]. SEM images of one super sharp tip before and after evaporation are presented in Fig. 3.1. Figure 3.1 (a) illustrates the shape of the tip shaft, which has a broad base for a better stability and an extremely small apex radius less than 10 nm. Figure 3.1 (b) is an image of a super sharp tip with magnetic coating, which shows a little increased tip radius.

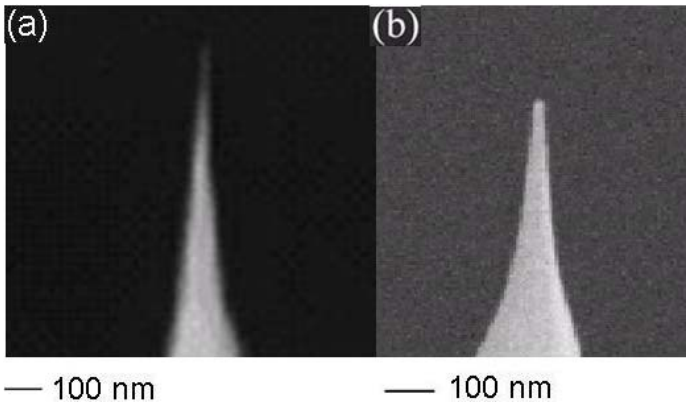

Fig. 3.1 SEM images of a super sharp tip. (a) Original tip and (b) with magnetic coating.

Similar super sharp MFM tips have been tested by Nanosensors GmbH with a hard disk sample consisting of customer-written tracks on a perpendicular recording medium [Gua03]. The details of the 22 nm track are revealed clearly, as shown in Fig. 3.2. This demonstrates the capability of the super sharp magnetic tip to resolve very fine magnetic structures.

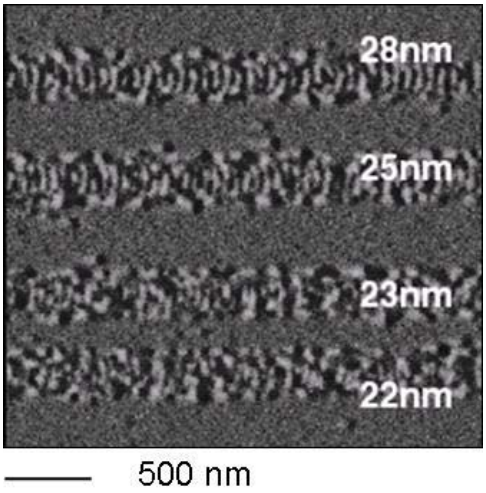

Fig. 3.2 MFM image of the customer-written bit tract with high densities. (22 nm means a bit size of 22 nm, and the same for the other values, from Ref. [Kob08]).

3.2.2 Ferrite-coated MFM tips

By radio frequency (RF) sputtering, we prepared BCFO films and (Ni, Zn) ferrite films (film thickness between 50 and 100 nm) on Si substrates analogous to the cantilevers, e.g., on (1 0 0) and (1 1 1) surfaces. A subsequent annealing in air was performed to form the desired crystal structure. The annealing temperature in air (15 min) was 1050 ^{o}C for BCFO, and 800 ^{o}C for (Ni, Zn) ferrite. These ferrite films on Si substrates were used for magnetic measurements and comparison.

After optimization of the magnetic properties of the films on the Si substrates, we

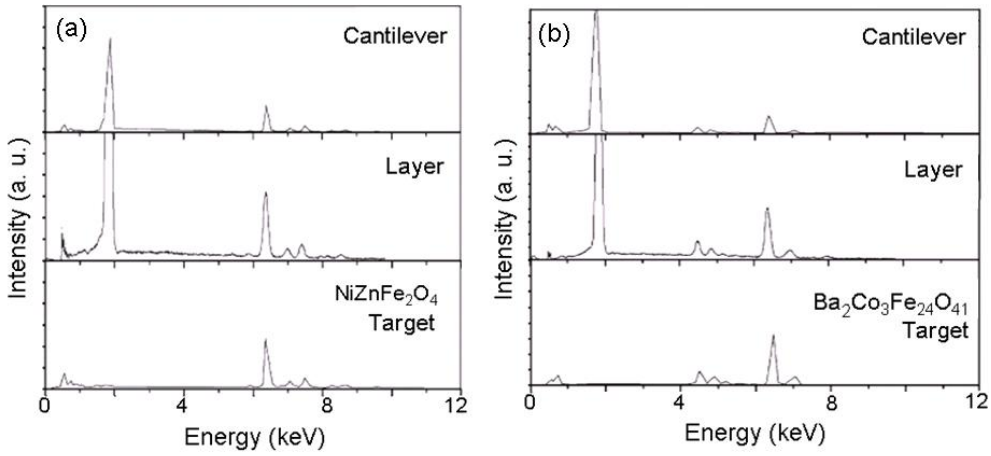

Fig. 3.3 EDX analysis of a coated cantilever, a thin film on a (1 1 1) Si substrate, and the target. (a) For $NiZnFe_2O_4$ coating and (b) for $Ba_2Co_3Fe_{24}O_{41}$ coating.

prepared a 50 nm thick coating on the micro-machined Si cantilever in a similar way. The high annealing temperature did not influence the mechanical properties of the cantilevers as the cantilever resonant frequencies varied only by 0.14% after annealing. An energy dispersive X-ray spectroscopy (EDX) analysis of the targets and the prepared coatings is presented in Fig. 3.3. All important spectral lines of the target are also present in the spectrum of the cantilever. SEM images of the cantilevers coated with ferrite films are shown in Fig. 3.4. The (Ni, Zn) ferrite coating is relatively smooth, while individual grains are clearly visible on the BCFO coating. From the SEM images, the apex radius of the ferrite-coated cantilevers was estimated to be between 60 and 80 nm.

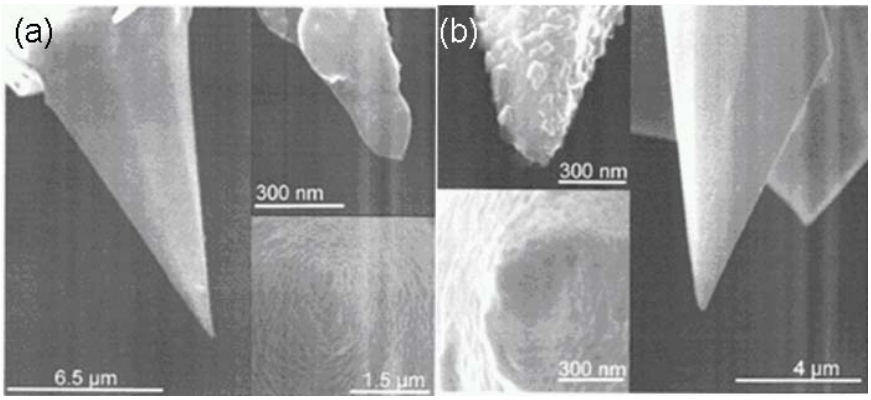

Fig. 3.4 Ferrite-coated tips of HF-MFM cantilevers. (a) A 50 nm thick (Ni, Zn) ferrite-coated tip and (b) a 50 nm thick BCFO-coated tip.

The magnetic imaging property of the ferrite-coated cantilevers was tested using the bit structure of commercial hard disks. As shown in Fig. 3.5, cantilevers with both types of ferrite material are able to perform MFM imaging. However, the difference between these two types of cantilevers is obvious. Figure 3.5 (a) shows the image obtained by the (Ni, Zn) ferrite-coated tip. Most bits in the image show a dark contrast. The result indicates a small coercivity of (Ni, Zn) ferrite, because the dark contrast is due to the tip remagnetization by the hard disk field. Figure 3.5 (b) presents the MFM result obtained by the BCFO-coated cantilever. The magnetic contrast achieved by the BCFO-coated cantilever is similar to that obtained by CoCr-coated ‘‘standard’’ MFM cantilevers.

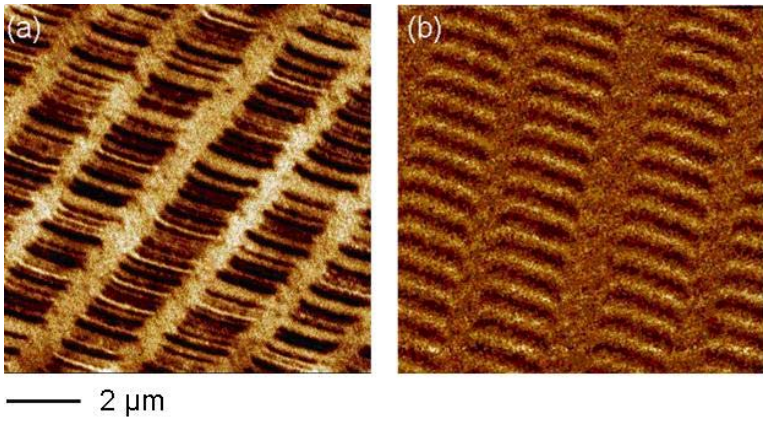

Fig. 3.5 MFM images of the bits of a hard disk (13 Gbyte capacity) obtained by ferrite-coated tips. (a) Obtained by a (Ni, Zn) ferrite-coated tip and (b) by a BCFO-coated tip.

3.3 Optimization of HF-MFM by super sharp tips and ferrite-coated tips

3.3.1 Experimental procedure

Figure 3.6 presents the schematic drawing of the HF-MFM setup. The dual-vibrational method was employed. An amplitude-modulated carrier current was generated by a high frequency generator. A modulation frequency of 1 kHz (i.e.,

smaller than the cantilever resonant frequency) was applied. The current fed into the writer pole was controlled by a current probe (Tektronix CT-6). The phase shift of the cantilever was measured as the cantilever was scanned in the MFM mode across the air-bearing surface of the recording head. The tip-to-sample distance was set to 50 nm. Hard disk write heads from Seagate (type: Seagate Barracuda) were employed in the HF-MFM measurements. These write heads were designed for longitudinal recording. With help of an optical microscope, the conductive pads of the write heads were connected to coaxial cables by two wires. These wires are short so that electrical noise from circumstance is reduced.

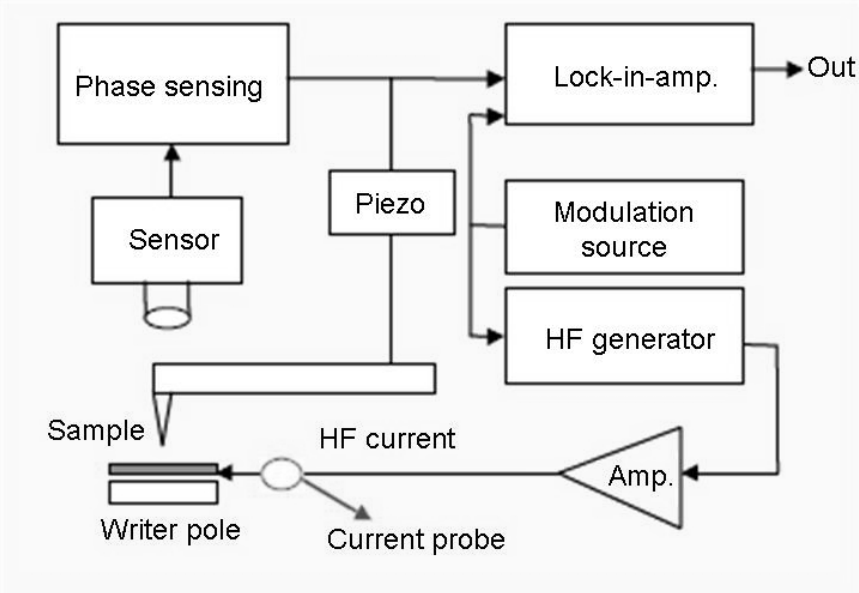

Fig. 3.6 Schematic drawing of the HF-MFM setup.

3.3.2 Results and discussion

3.3.2.1 High special resolution obtained by super sharp MFM tips

Figure 3.7 presents the AFM and HF-MFM image of a hard disk write head obtained by a super sharp tip. The carrier frequency is 100 MHz, and the HF current is 25 mA. The topography of the writer pole is quite clear, and several details are resolved. The image reveals that recent longitudinal hard disk write heads have overall dimensions

of few micrometers in length, and ~300 nm in width. The HF-MFM image shows the entire head structure: the leading and trailing edge of the gap, the shared pole (P1) and the free trailing pole (FTP or P2). The arrows point to the same location at the gap in both images. The maximum stray field is concentrated at the gap. A certain stray field also appears along the edges of the P2 pole on the air-bearing surface. According to the obtained feature of the high frequency field image, the writing gap between P1 and P2 poles can be estimated to be about 100 nm. The achieved resolution of the HF-MFM image compares well with that by the standard MFM technique.

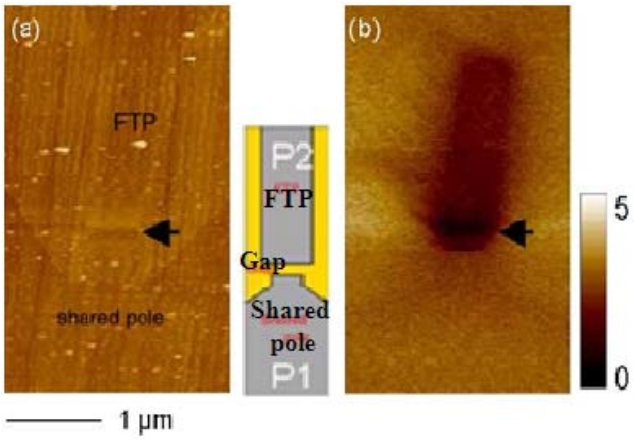

Fig. 3.7 (a) AFM image and (b) HF-MFM image of a hard disk write head recorded by a super sharp MFM tip. Black arrows mark the gap at the same location in both images. The small figure right to (a) gives a schematic drawing of the write head. The carrier frequency is 100 MHz. Scale bar of the phase shift is given right to (b).

In Fig. 3.8, the HF-MFM images obtained by a super sharp tip and by a standard MFM tip are presented. Both tips are covered by CoCr coating and hard disk write heads under study are from the same batch. The carrier frequency in both cases is 100 MHz. The HF-MFM image recorded by the standard tip yields a strong HF-MFM signal, but the region around the gap is blurred. The image obtained by the super sharp tip yields a relatively small MFM signal as compared to the standard tip, but more details of the head structure are resolved in this image, e.g., a two-peak structure at the writing gap. The HF-MFM image obtained by the super sharp tip demonstrates also an improved signal-to-noise ratio.

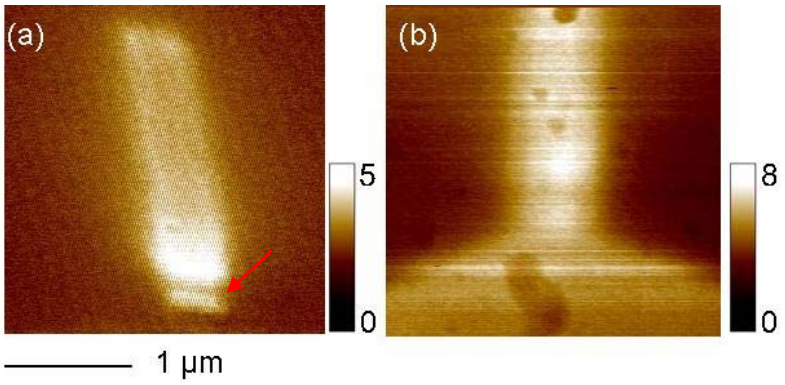

Fig. 3.8 Comparison of HF-MFM images obtained (a) by a super sharp MFM tip and (b) by a standard MFM tip. The carrier frequency is 100 MHz. The arrow indicates the two-peak structure at the writing gap. Scale bars of the phase shift are given right to the both images.

Figure 3.9 presents the frequency dependence of the HF-MFM signal for carrier frequencies between 100 and 1000 MHz, and constant current. At frequencies below 500 MHz, the super sharp tip delivers a very detailed view of the emanating stray field from the write head. However, the MFM signal decays at frequencies above 500 MHz. When the frequency is above 1000 MHz, the HF-MFM signal vanishes completely. The property of the CoCr material limits the frequency response of the super sharp tips.

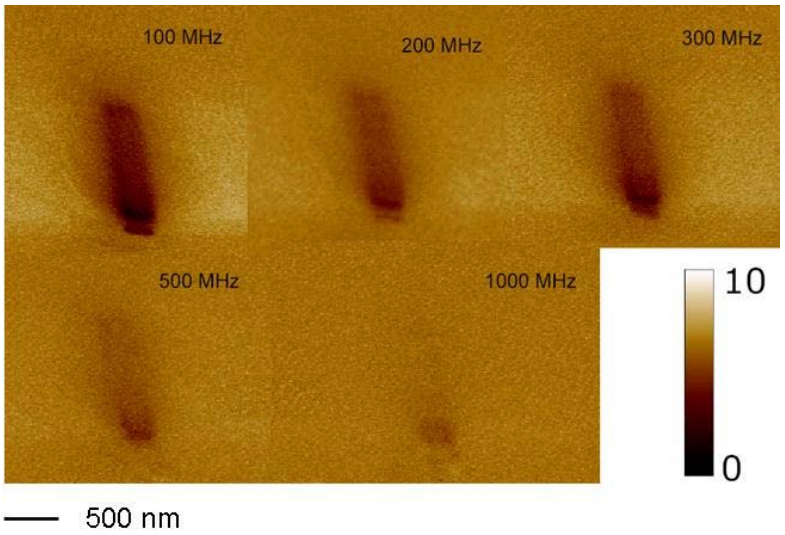

Fig. 3.9 Frequency dependence of the HF-MFM signal of the hard disk write head for the super sharp MFM tip. The carrier frequencies are noted in the corresponding images. Scale bar of the phase shift is given in the left-down corner.

3.3.2.2 High-frequency response of ferrite-coated MFM tips

Figure 3.10 presents the AFM and HF-MFM images of a hard disk write head obtained by (Ni, Zn) ferrite- and CoCr-coated MFM-tips. The feeding HF current is set to 1 GHz. Figure 3.10 (b) shows the HF-MFM image obtained by the (Ni, Zn) ferrite-coated tip. With the (Ni, Zn) ferrite-coated tip, a clear distribution of the stray field from the write head is displayed, which is similar to those images obtained at lower frequencies. In Fig. 3.10 (b), the strongest field is found directly at the writing gap. The downtrack profile clearly demonstrates the stray field distribution through the P1 and P2 poles. In contrast, the HF-MFM image obtained by the CoCr-coated tip is ambiguous and the magnetic signal is close to the noise level from the downtrack profile shown in Fig. 3.10 (c).

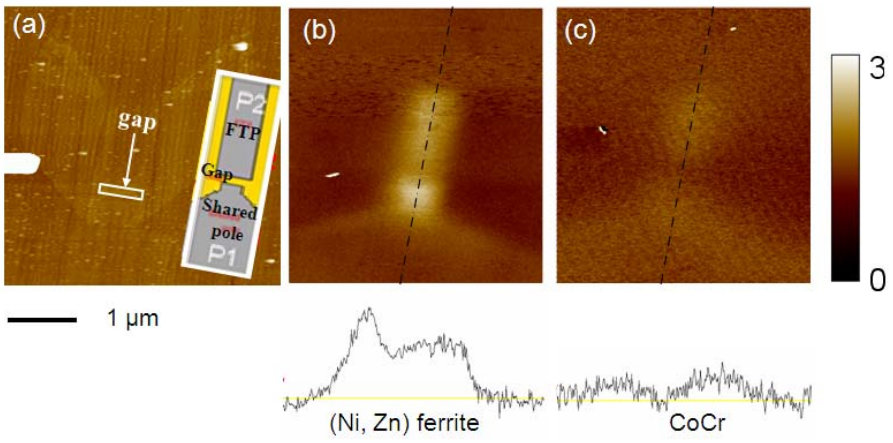

Fig. 3.10 (a) AFM image of a Seagate write head. (b) and (c) are HF-MFM images of the same write head at 1 GHz recorded by (Ni, Zn) ferrite- and CoCr-coated MFM tips, respectively. The corresponding down track profiles of the stray fields are presented below the images. The inset in (a) gives a schematic drawing of the write head. The arrow marks the location of the gap between P1 and P2. Scale bar of the phase shift is given for the images of (b) and (c).

The behavior of the hard disk write head working at high frequencies is further investigated by the (Ni, Zn) ferrite-coated MFM tip. The magnetic signals of the P1 and P2 poles are measured with various intensities of feeding currents at 1 GHz. The maximum values of the MFM signals of the P1 and P2 poles are determined by the analysis software from Digital Instrument. They are plotted versus the applied feeding

currents as shown in Fig. 3.11. The fitted lines in the plot show that the maximum signals are polygonal functions of the feeding current. According to the first orders calculation [Li02]: $H_a = NI/l_c$ is the magnitude of the applied field produced by the coil current I with a core length l_c; $H_g \propto (\kappa_0/\mu_0)H_a+(v/\mu_0) H_a^2$ is the magnitude of the gap field from the write head, where κ_0 is the initial susceptibility of the core material and v the Rayleigh constant. The Rayleigh constant describes the irreversible Barkhausen jumps. From the above relations, it is easy to find out that the gap field has a similar polygonal function of the feeding current as to the experimental results. However, both curves in Fig. 3.11 have different slope. This may indicate that the material properties of the core materials and the Reyleigh constants are different at the two poles. Though a deep insight into the relation between the gap field and the feeding current needs further investigation, the agreement between the experiment and the model suggests that both the tested hard disk write head and the (Ni, Zn) ferrite-coated MFM tip can work properly in the GHz range. Furthermore, the monotonous increase of the magnetic signal with the feeding current indicates that the write head is not yet saturated, even at a relatively large feeding current of 90 mA.

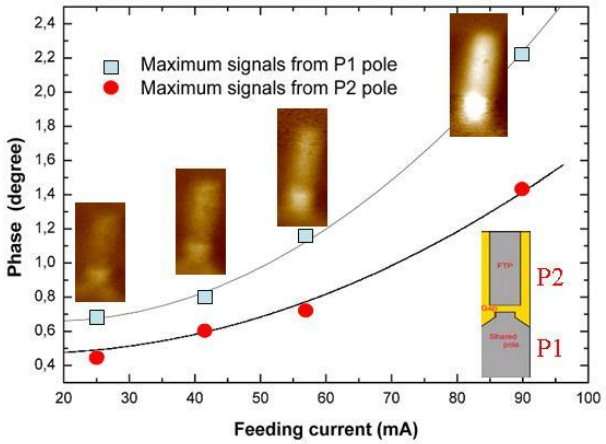

Fig. 3.11 Maximum magnetic signals of P1 and P2 poles versus the feeding current for the (Ni, Zn) ferrite-coated tip. The carrier frequency is 1 GHz.

The HF-MFM signals versus the carrier frequencies for (Ni, Zn) ferrite- and CoCr-coated tips are displayed in Fig. 3.12. The signals are normalized to the

reference one measured at 100 MHz by the (Ni, Zn) ferrite-coated tip. The measurements have been performed at frequencies of 100, 300, 400, 500, 900 and 1000 MHz. A constant feeding current of 26 mA is kept by adjusting the power of the applied carrier wave. Both curves in Fig. 3.12 follow the same trend: HF-MFM signals are reduced with increasing carrier frequency, especially a dramatic drop of the HF-MFM signal at around 400 MHz is observed. The operating frequency of the write head is 650 MHz. Above this frequency, the low efficiency of the write head leads to a low gap field. From the plot, it is obvious that the (Ni, Zn) ferrite-coated tip is more sensitive to the change of stray fields than the CoCr-coated tip over the whole frequency range under study. Therefore, the (Ni, Zn) ferrite-coated tips are suitable to characterize the high frequency performance of hard disk write heads. However, the reason for the dramatic drop is not very clear. At around 400 MHz, the write head might get resonant due to the inductance and capacitance of the write core. The perpendicular element of the stray field from the gap will then be strongly suppressed.

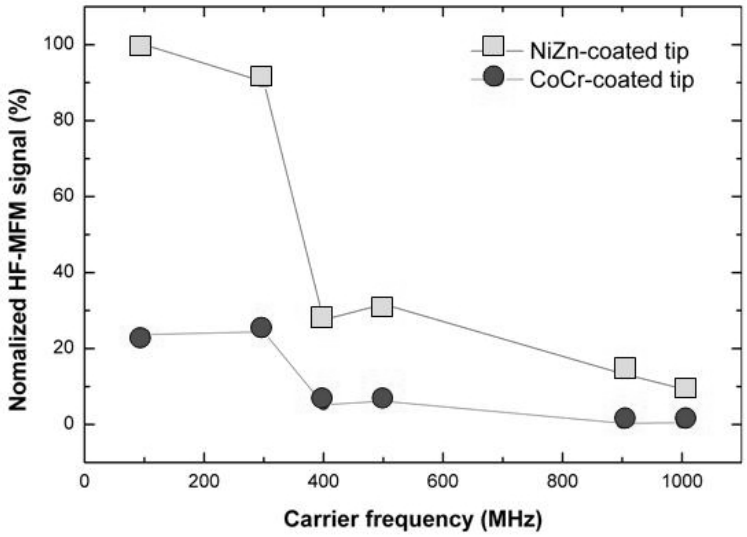

Fig. 3.12 HF-MFM signals versus carrier frequencies for (Ni, Zn) ferrite- and CoCr-coated tips with 26 mA feeding current.

From the mechanism of HF-MFM, the advantage of (Ni, Zn) ferrite-coated tips can be easily understood. The time-averaged effective force sensed by MFM tips could be expressed as

$$F_{\text{eff}} = \mu_0 (\partial/\partial z) < \mathbf{m}_t(t) \cdot \mathbf{H}(t) >$$
$$= 2\, \mu_0\, \chi V\, \mathbf{H}_1 \cdot \partial \mathbf{H}_1/\partial z < f_1(t) f_2(t) >, \qquad (3.1)$$

where μ_0 is the permeability of free space, χ is the susceptibility of the tip material at the corresponding frequency, $\mathbf{H}_1$ is the amplitude of the high-frequency magnetic field of the write head, and V is the volume of the interacting part of the magnetic tip with the write head field. The magnetic moment of the MFM tip is $\mathbf{m}_t(t) = \mu_0 \chi \mathbf{H}_1 V f_1(t)$. The magnetic field of the write head is $\mathbf{H}(t) = \mathbf{H}_1 f_2(t)$.

From Eq. (3.1), the effective force depends on the time correlation of $f_1(t)$ and $f_2(t)$. The maximum HF-MFM signal is obtained when $f_1(t)$ and $f_2(t)$ are equal. With a low coercivity of less than 0.3 kA/m [Ash97], the magnetization of the (Ni, Zn) ferrite-coated tip can be easily switched and, therefore, follows the external magnetic field very effectively. In contrast, the usually employed CoCr is a hard magnetic material with a coercivity of ~ 95 kA/m [Hem86]. The high coercivity creates a large hysteresis loss during each magnetization switching process. Other important factors in the frequency range of interest are the susceptibility and the electrical resistivity of the tip material. Ferrite materials are well known for their high permeability (normally from 100 to 1000 for (Ni, Zn) ferrite) and high electrical resistivity (about 10^{11} μΩcm for (Ni, Zn) ferrite), for which ferrites are employed as core materials for broad applications at high frequencies [Ash97]. In contrast, CoCr material has a relatively low permeability and a 9 orders of magnitude lower electrical resistivity than (Ni, Zn) ferrite [Ash97]. High permeability assures strong magnetic interactions between the magnetic tip and the magnetic field, and high electrical resistivity can greatly reduce the loss from eddy currents at high frequencies. Thus, the improvement of high frequency response by the (Ni, Zn) ferrite-coated tips is clearly due to the low coercivity, high permeability and high electrical resistivity.

Figure 3.13 presents the HF-MFM images of hard disk write heads obtained by (Ni, Zn) ferrite-coated tips and BCFO-coated tips at 1 GHz and 2 GHz. From Fig. 3.13(a)

and (b), the (Ni, Zn) ferrite-coated tip is obviously sensitive to a high frequency field of 2 GHz, but the achieved HF-MFM contrast decrease strongly. In this high frequency range, the BCFO-coated tip shows a better performance, as the HF-MFM contrast at 2 GHz is almost the same as that at 1 GHz. The results are in agreement with the fact that the BCFO material has a much higher cut-off frequency than the (Ni, Zn) ferrite [Gol90].

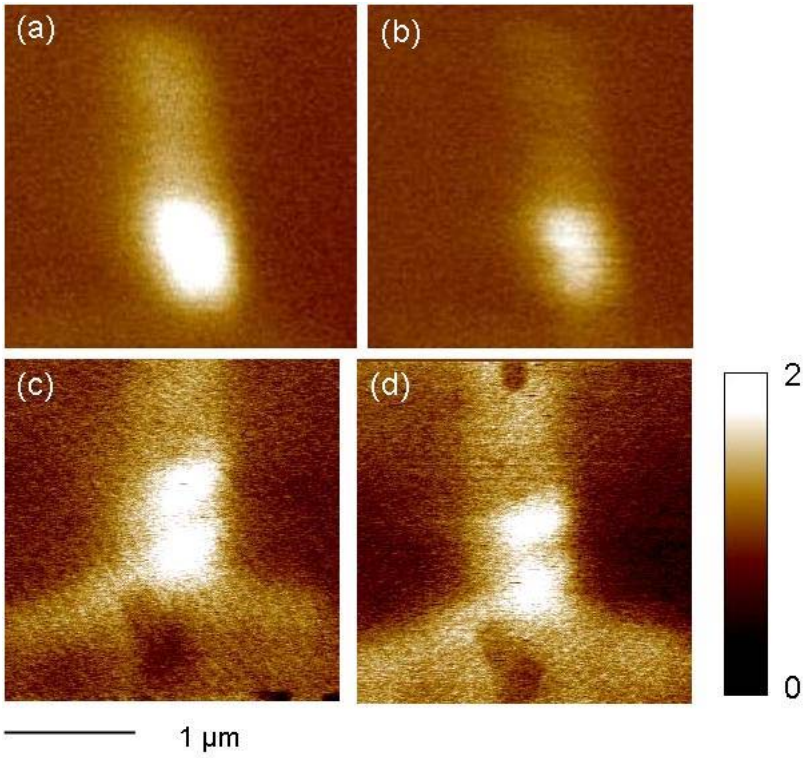

Fig. 3.13 HF-MFM images of hard disk write heads (a, b) taken by (Ni, Zn) ferrite-coated tips and (c, d) by BCFO-coated tips at two different carrier frequency (1 GHz and 2 GHz). Scale bar of the phase shift is given right to the images.

However, the BCFO coating was found difficult to be prepared on the Si cantilevers. Many grains are formed on the tip surface as shown in Fig. 3.4(b), leading to a bad reproducibility of the final MFM tips [Kir07]. The grains on the tip cause also the deterioration of the spatial resolution of HF-MFM, which is clearly seen from the down track profiles shown in Fig. 3.10.

3.3.3 Conclusion

The super sharp MFM tips can greatly improve the spatial resolution of the HF-MFM. More details can be resolved in the interesting gap region of hard disk write heads. To image high frequency fields at hundreds of MHz, super sharp tips will be the best choice. However, the high frequency response of thin CoCr coatings (10 nm) is insufficient to image hard disk write heads above 1 GHz. For operating HF-MFM at higher frequencies, a super sharp tip fabricated directly from a ferrite-coated MFM tip by the FIB milling technique could be a possible solution.

The ferrite-coated cantilevers can considerably improve the HF-MFM sensitivity as compared to the standard CoCr-coated ones. They allow HF-MFM imaging of hard disk write head with carrier frequencies of 2 GHz. The improvement of high-frequency response by the (Ni, Zn) ferrite-coated tips is due to their low coercivity, high susceptibility and high electrical resistivity. The BCFO-coated tip shows a better performance than that of (Ni, Zn) ferrite-coated one due to its high cut-off frequency. However, the overall thickness of these two coatings should be reduced in order to further improve the spatial resolution. This would require a better control of the growth process of ferrites on Si.

Chapter 4

Construction of a ferromagnetic resonance force microscope for the detection of biogenic magnetic particles

In this chapter, ferromagnetic resonance force microscopy (f-MRFM), a variant of MFM, is discussed with respect to the potential of *in situ* detecting magnetic nanoparticles in organisms. The construction of our self-made f-MRFM is explained in detail. The set-up of f-MRFM has been tested with a piece of yttrium iron garnet (YIG) film. Magnetotactic bacteria are considered as a suitable sample to demonstrate the applications of f-MRFM in the field of biology. Two methods have been developed to prepare a controllable number of magnetotactic bacteria on cantilevers for investigation. Performing f-MRFM measurements on magnetotactic bacteria proves to be difficult under ambient conditions. Suggestions are given for the further development of f-MRFM to fullfil the purpose.

4.1 Introduction

Magnetic resonance force microscopy (MRFM) is a novel scanning probe method that combines the three-dimensional imaging capability of magnetic resonance imaging with the high sensitivity and resolution of scanning probe microscopy (SPM). In the nuclear magnetic resonance mode or the electron spin resonance mode, MRFM enables nondestructive, chemically specific studies of materials [Sid95]. MRFM has realized single electron spin sensitivity (9.27×10^{-24} Am^2) and a spatial resolution of 25 nm [Rug04]. More details on MRFM are presented in Chapter 2. F-MRFM is related to the ferromagnetic resonance mode and is developed to characterize the properties of magnetic microstructures. Zhang et al. first detected ferromagnetic resonant signals in YIG by using f-MRFM [Zha96]. With f-MRFM, variations in the magnetic anisotropy field and the inhomogeneity of microscopic magnetic thin films

were observed [Zha98]. f-MRFM can also provide direct measurements of both longitudinal and transverse relaxation rates in micron-sized ferromagnetic samples [Kle03]. So far, most studies on ferromagnetic materials by f-MRFM were focused on YIG structures [Zha96, Mid00, Cha02, Kle03] and metallic films [Zha98, Mor03, Vol04].

Magnetite (Fe_3O_4) and related iron oxide nanoparticles are the only magnetic materials found in a wide range of organisms, many of which show the ability of migration or homing by using the extremely weak magnetic field of the earth [Kir01]. After long years of investigation and debate, the role of the magnetite nanoparticles in the magnetoreception of organisms still remains unclear [Die00, Rit00, Mor04, Rit04]. In order to ultimately understand the correlation between biogenic magnetite nanoparticles and the magnetoreception, *in situ* observation of the arrangement of magnetite nanoparticles in tissues is mostly of interest. However, this is not possible by most techniques due to the lack of sensitivity or spatial resolution. MRFM was originally proposed to *in situ* three-dimensionally image individual biological molecules [Sid91, Sid95] by nuclear magnetic resonance [Sid91]. However, the nuclear magnetic moment of biological molecules is extremely weak (about 3 orders of magnitude smaller than that of a single electron spin), and not yet detectable by the current MRFM technique [Sid91, Rug04]. MRFM was rarely applied to biological samples. In contrast, biogenic magnetite nanoparticles contain much more magnetic moments than other organic materials in the biological tissues and are plausibly detectable by f-MRFM. In this study, f-MRFM is concerned with two purposes:

(1) *in situ* and non-destructive detection of biogenic magnetite nanoparticles;
(2) demonstration of the capability of f-MRFM in biological studies.

There are also two challenges in this task: (1) magnetite has a large ferromagnetic resonance (FMR) linewidth, which will considerably reduce the FMR signal and (2) magnetite nanoparticles are distributed in the tissues, so that only a fraction is in resonance at a given time in an applied gradient field for f-MRFM measurements.

Magnetotactic bacteria are ideal for the purposes, as this kind of bacteria is well known to produce cellular magnetite nanoparticles [Sch99]. One TEM image of magnetotactic bacteria is shown in Fig. 4.1. More details on the magnetotactic bacteria are presented in Chapter 2.

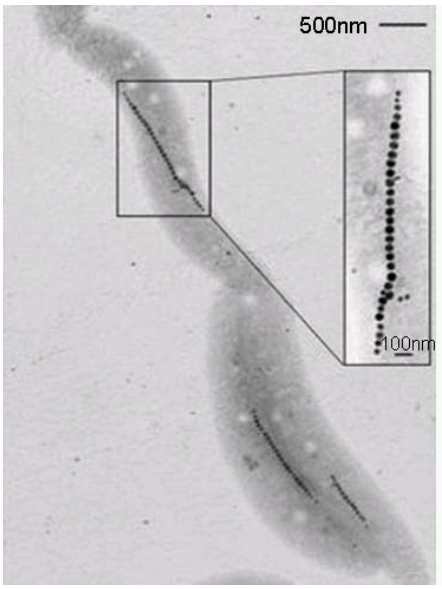

Fig. 4.1 TEM image of a magnetotactic bacterium. The inset shows a chain of magnetite nanoparticles at a higher resolution. From [Sch99]

4.2 Construction and test of a ferromagnetic resonance force microscope

4.2.1 Construction of f-MRFM

The schematic diagram of MRFM is shown in Fig. 4.2. In MRFM, either a sample or a small permanent magnet (that provides a gradient field) is fixed to a cantilever. In the "sample on cantilever" approach, the sample is mounted on the cantilever and the permanent magnet with spatial dimensions comparable or larger than the actual sample is placed nearby. This approach is employed in most experiments, as the result analysis is straightforward [Rug94, Zha96, Zha98]. The force stemming from each

volume element is approximately equal and the resonant locations selected by the gradient field can be easily analyzed [Sut04]. In order to apply MRFM as an actual high spatial resolution imaging technique for samples of arbitrary size and shape, the permanent magnet needs to be mounted to the cantilever. This approach is called "magnet on cantilever" approach (more details are described in section 2.4). However, the "magnet on cantilever" approach often gives rise to large and unwanted direct couplings between the magnet and various time-dependent applied fields [Zha96]. In this study, the "sample on cantilever" approach is taken for simplicity.

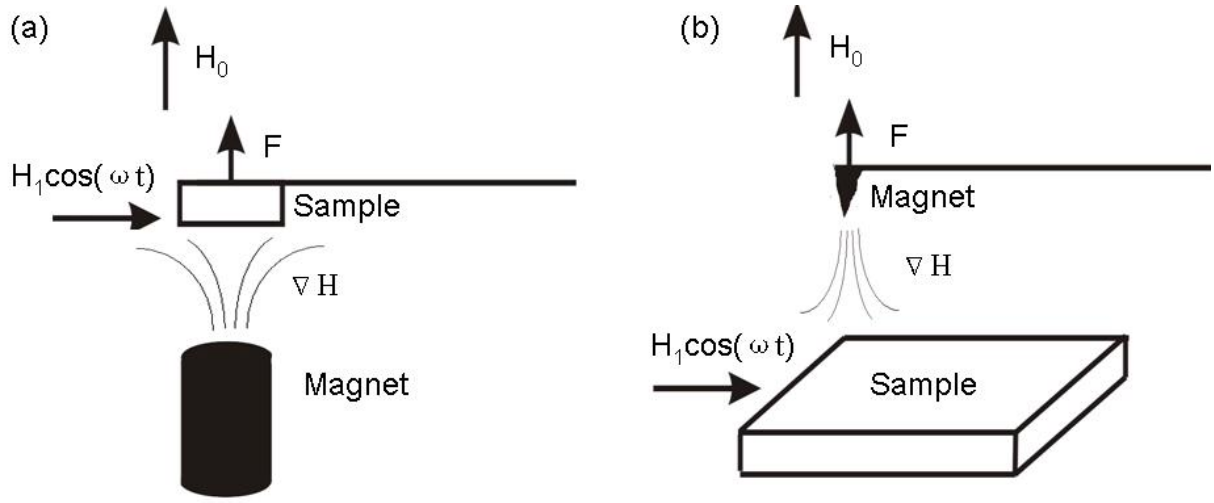

Fig. 4.2 Schematic diagram of MRFM. (a) "Sample on cantilever" set-up and (b) "magnet on cantilever" set-up, with $H_0=H_{ext}+ H_{mod}{}^0$.

The construction of the self-made f-MRFM is shown in Fig. 4.3. The main part of the f-MRFM is based on a commercial non-contact SPM (Topometrix SPM nanovision). It provides a laser-beam deflection system to detect the cantilever vibration and also modules for data processing and analysis.

Four magnetic fields are involved in the f-MRFM system:

(1) An external sweeping field H_{ext}, provided by a solenoid.

(2) A low frequency modulation field $H_{mod}{}^0$, provided by a modulation coil, along the H_{ext} field. The modulation frequency is ω_{ext}.

(3) A magnetic gradient field ∇H provided by a permanent magnet, with a gradient

along the vibration direction of the cantilever.

The local field at the sample is then the sum of fields (1)-(3).

(4) A high frequency ac field H_1 of central frequency ω and modulation frequency ω_{ac} provided by a stripline resonator, and perpendicular to the local field, and perpendicular to the vibration direction of the cantilever, as shown in Fig. 4.3.

ω_{ext} is chosen as the difference between the ac modulation frequency ω_{ac} and the cantilever resonant frequency ω_0.

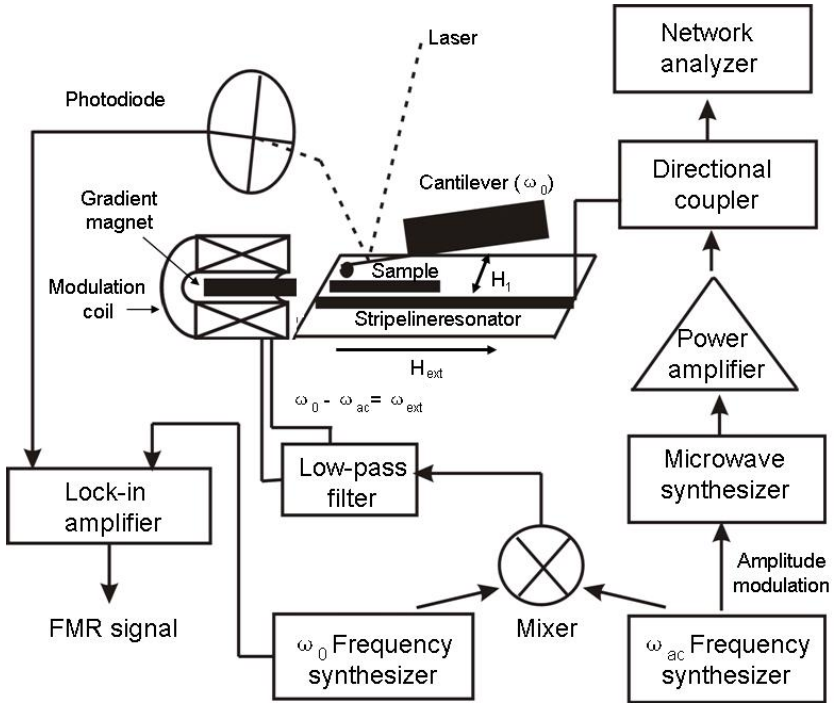

Fig. 4.3 Construction of the f-MRFM (not to the scale).

Construction of the magnetic field system

(1) The high frequency ac field

For magnetic resonance measurements, the resonant field should be sufficiently larger than the linewidth. As magnetite has a very broad linewidth of about 100 mT [Von66],

a large resonant field and, consequently, a high frequency ac field in the GHz range are necessary to generate ferromagnetic resonance in magnetite. LC circuits based on a small coil are unable to provide such high frequency fields. Therefore, a stripline resonator is employed.

A stripline resonator consists of a microstrip conductor, a ground metal plane and a dielectric substrate in between, as shown in Fig. 4.4 (a). The high frequency electric and magnetic fields are mostly confined in a narrow region between the microstrip and the ground as illustrated in Fig. 4.4 (b).

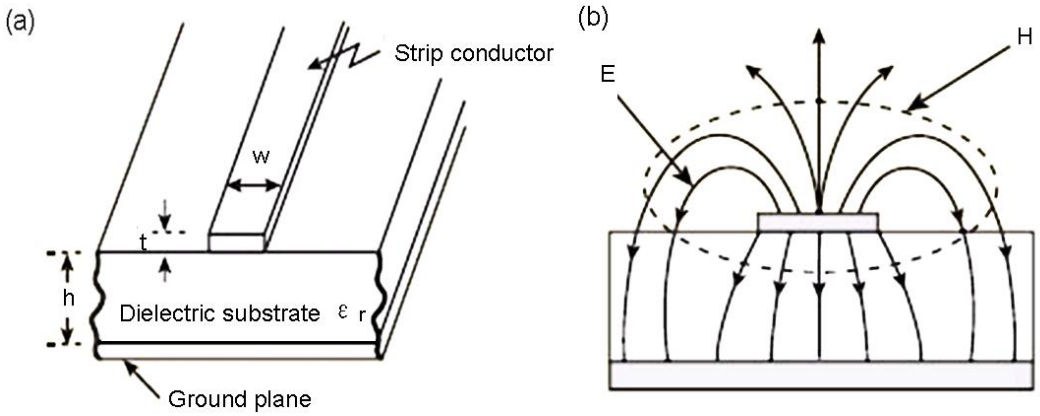

Fig. 4.4 Schematic drawing of (a) a microstripline resonator and (b) its electric and magnetic field distribution.

The resonant frequency f of a stripline resonator is determined by the length l, the width w and the thickness t of the microstrip, the dielectric constant ε_r and the thickness h of the dielectric substrate.

If the respective conditions are satisfied ($\varepsilon_r < 16$, $0.05 < w/h < 20$, $t < h/2$, and $t < w/2$), the properties of the stripline resonators can be determined by the following equations [Jab92]:

$$h_{eff} = h - 2t\,, \tag{4.1}$$

$$w_{eff} = w\{1 + \frac{1}{\pi}[\ln(\frac{2h}{t}) + 1]\}\,, \tag{4.2}$$

$$\varepsilon_{eff} = \frac{\varepsilon_r + 1}{2} + \frac{\varepsilon_r - 1}{2\sqrt{1 + 12\frac{h_{eff}}{w_{eff}}}}, (\frac{h_{eff}}{w_{eff}} \le 1)$$
$$= \frac{\varepsilon_r + 1}{2} + \frac{\varepsilon_r - 1}{2}[\frac{1}{\sqrt{1 + 12\frac{h_{eff}}{w_{eff}}}} + \frac{2}{5}(1 - \frac{w_{eff}}{h_{eff}})^2], (\frac{h_{eff}}{w_{eff}} > 1) \quad (4.3)$$

$$f = \frac{1}{2\sqrt{\mu_0 \varepsilon_0 \varepsilon_{eff}}\, w_{eff}}, \quad (4.4)$$

$$\lambda = \frac{c}{f\sqrt{\varepsilon_{eff}}}. \quad (4.5)$$

Hereby, μ_0 is the vacuum permeability, ε_0 is the vacuum permittivity, λ is the wavelength at resonance, and c is the speed of light.

When the length of the microstrip is $l = \lambda/2$, a half-wavelength stripline resonator is obtained.

The resonator should have an impedance of 50 Ohm in order to match other instruments or transmission lines operated in experiments. The impedance Z of the stripline resonator can be determined by [Jab92]

$$\frac{Z}{Z_0} = \frac{120\pi}{\sqrt{\varepsilon_{eff}}[\frac{w_{eff}}{h_{eff}} + 1.393 - \frac{2}{3}\ln(\frac{w_{eff}}{h_{eff}} + 1.444)]} \ (= 1), \quad (4.6)$$

where Z_0 denotes 50 Ohm.

A plate made of hydrocarbon ceramic material (TMM10 from Mauritz GmbH, Germany) has been employed, which has a thickness of 0.635 mm and a dielectric constant of 9.2. Both surfaces of the plate are coated with a 35 μm thick copper layer.

According to Eqs. (4.1)-(4.6), a half-wavelength stripline resonator operated at 4 GHz is designed. The width and length of the resonator are determined to be 0.64 mm and

14.94 mm, respectively. Then, the layout of the design with the calculated parameters was drawn by the software "Celwin3.2", and the final stripline resonator was fabricated by laser lithography (in Prof. Seidel's group, Saarland University).

The resonant frequency of the fabricated stripline resonator was experimentally determined. High frequency waves with constant power were generated by a sweeping oscillator (HP 8350B) and fed into the stripline resonator. The power of the wave reflected from the stripline resonator was determined by a network analyzer (HP 8756A). According to the powers of the original and reflected waves, the absorbed power by the stripline resonator was calculated. The absorbed power was then plotted as a function of the wave frequency. As shown in Fig. 4.5, the maximum absorption occurs at 4.125 GHz, which gives the resonant frequency of the stripline resonator and as expected by the design. The strength of the high frequency magentic field is calculated to be 0.8 mT for an incident power of 1 W by using a solver of two-dimensional microstrip circuit (Sonnet Lite, http://www.sonnetusa.com).

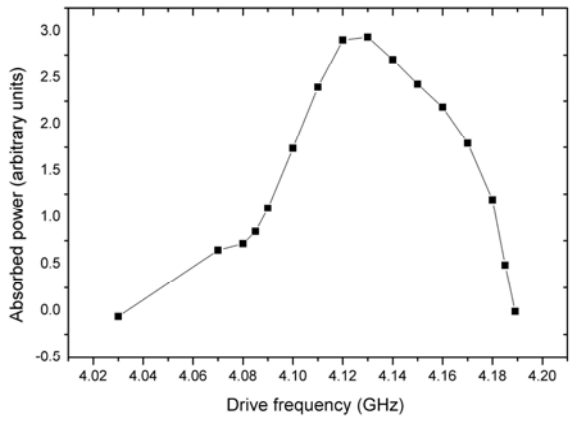

Fig. 4.5 The absorbed power of the fabricated stripline resonator versus frequency.

(2) The magnetic gradient field

The magnetic gradient field is created by a small permanent magnet. In f-MRFM experiments, a NdFeB magnet (N45) is employed. It has a remanence magnetization of 1.37 T and a coercivity of 1.1 T according to the product data sheet

(www.forcefieldmagnets.com). The magnet is cylindrical with both a diameter and a height of 2 mm.

Figure 4.6 shows the dependence of the magnetic field on the distance from the magnet in the axis direction. The distance between the magnet and the magnetic probe is controlled by a micrometer screw. The field gradient at a distance of 1 mm is about 100 T/m.

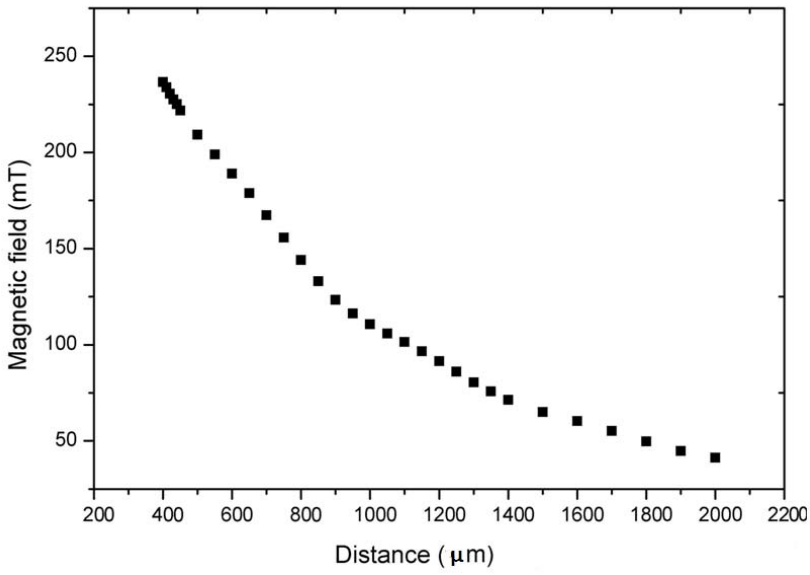

Fig. 4.6 Distance dependence of the magnetic field from the permanent magnet.

(3) The low frequency modulation field

The low frequency modulation field is produced by a small coil. The coil is made of a copper wire with a diameter of 0.1 mm. The inner diameter of the coil is made large enough to enclose the permanent magnet for the gradient field. The resistance of the coil is 39 Ohm. The current fed into the coil is generated using a frequency synthesizer.

The frequency of the modulation field is in the kHz range, which is comparable to the resonant frequency of the cantilever. During the experiments, the strength of the

modulation magnetic field was controlled by adjusting the amplitude of the feeding current. When the current amplitude was set to 100 mA, the magnetic field strength was measured to be 0.8 mT at a distance of 3 mm from the coil in the axis direction.

(4) The external sweeping field

The external sweeping field is produced by a solenoid. The field strength is enhanced by a pair of iron cores. The solenoid has a resistance of 2.2 Ohm. The sweeping function is realized by the combination of a function generator (HP 33120A) and a self-made voltage to current converter. The voltage to current converter can output a maximum current of 8 A for the employed solenoid. The maximum field in the middle of two iron cores was measured to be 370 mT.

According to the diagram in Fig. 4.3, the four magnetic fields are integrated in the SPM system. The constructed f-MRFM is shown in Fig. 4.7. The external magnetic field is perpendicular to the vibration direction of the cantilever, and the high frequency ac field is oriented at right angles both to the external field and to the vibration direction of the cantilever.

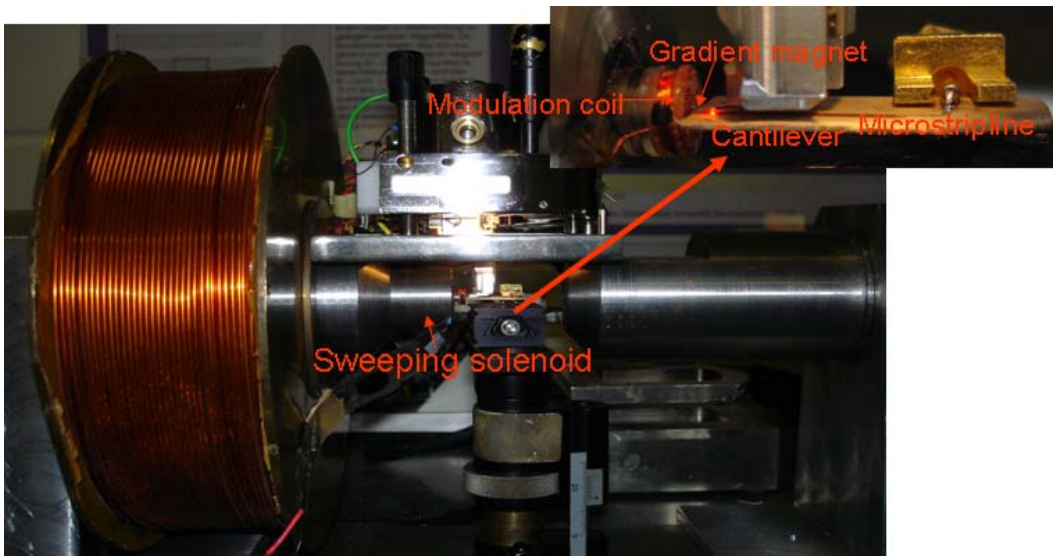

Fig. 4.7 The f-MRFM set-up. The core parts (microstripline, cantilever, gradient magnet and modulation coil) are shown in details in the inset.

4.2.2 Test of the f-MRFM

Sample preparation and experiment

The YIG film was grown by isothermal liquid phase epitaxy (about 700 ^{o}C) on a (100) gadolinium gallium garnet substrate. The thickness of the YIG film is about 1 μm. For details on the sample preparation please refer to Ref. [Hel02].

A small piece of YIG film was mounted onto a tipless cantilever (MicroMash CSC12) by three steps: (1) deposition of a small droplet of two-component epoxide glue onto the cantilever by a fiber; (2) pick up of a small piece of YIG film by another fiber; (3) movement of the YIG film close to the droplet on the cantilever and deposition. After 5 minutes, the YIG film will be tightly glued on the cantilever. All the steps were done by a micromanipulator under a CCD camera.

From the SEM image in Fig 4.8, the shape of the YIG film is roughly rectangular with a width of 35 μm and a length of 115 μm.

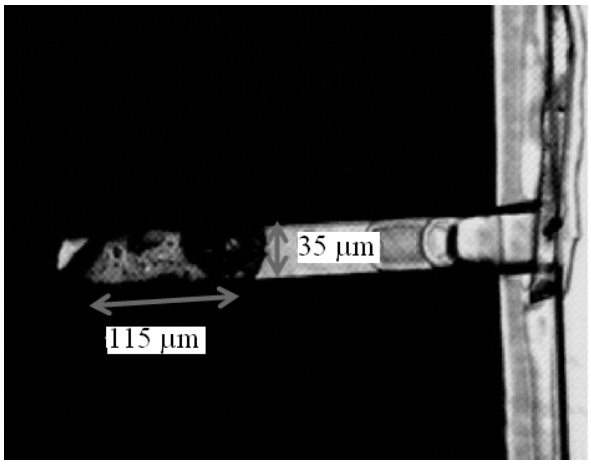

Fig. 4.8 Cantilever with a small piece of YIG film.

The employed cantilever had a resonant frequency of 10.37 kHz. After the YIG film was mounted, the resonant frequency of the cantilever was shifted to 4.61 kHz as shown in Fig. 4.9. From the frequency spectrum, the quality factor Q of the cantilever was determined to be 36.6.

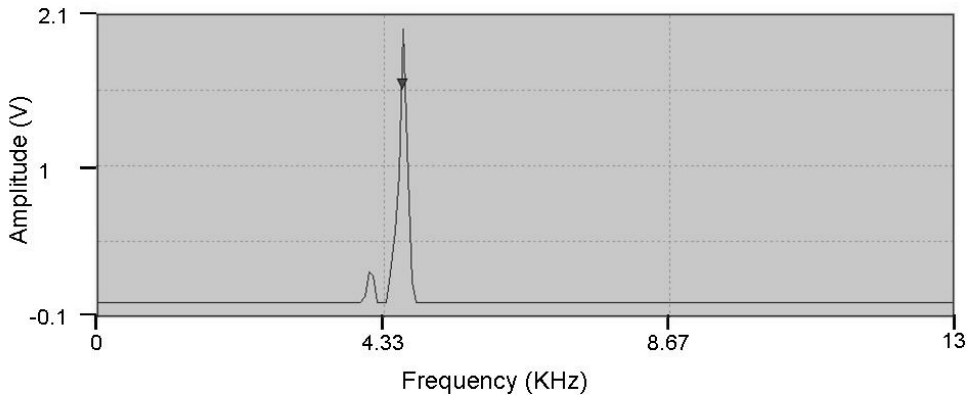

Fig. 4.9 Frequency spectrum of the cantilever with a small piece of YIG film.

The anharmonic modulation technique was employed to generate time-varying force on the cantilever at its resonant frequency [Bru95]: the high frequency ac field H_1 (4.125 GHz) was 100% amplitude modulated at a frequency of 6.61 kHz, and the frequency of the modulation field H_{mod}^0 was set to 2 kHz. The difference of two modulation frequencies is equal to the resonant frequency of the cantilever (4.61 KHz). The high frequency ac wave was amplified to 1 W (the maximum output of the employed amplifier) in order to maximize H_1. The current for H_{mod}^0 was set to 100 mA.

The cantilever was positioned about 1 mm away from the permanent magnet. In order to have a field gradient along the vibration direction, the cantilever was placed off the axis of the magnet.

Before the experiment, the actual magnetic field at the sample location was measured as a function of the sweeping voltage. The field sweeping rate was set to 1.4 mT/s.

Results and discussion

Four f-MRFM spectra of the YIF film are shown in Fig. 4.10. Figure 4.10 (a) is obtained under the above-described condition. Two resonant absorption peaks have been detected. The peaks are located at 70.1 and 70.9 mT, respectively.

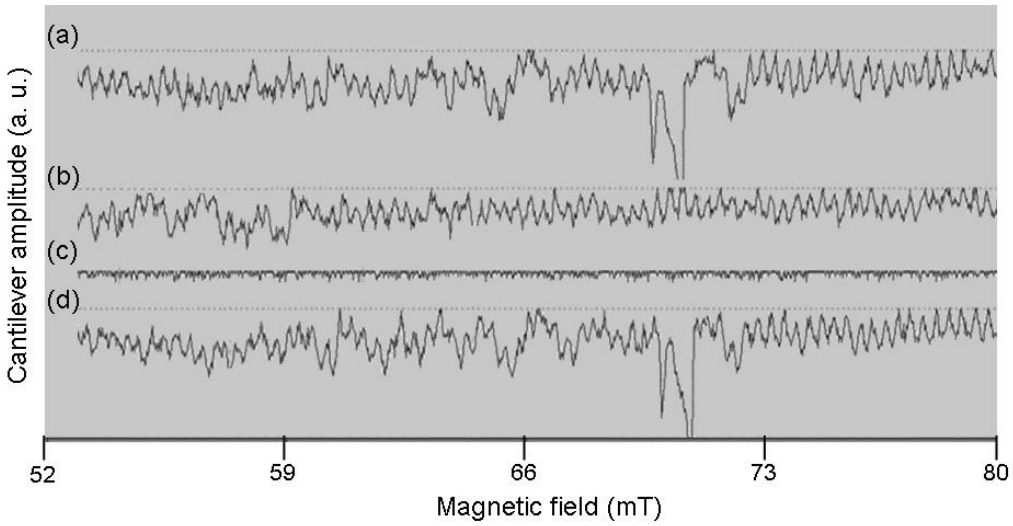

Fig. 4.10 f-MRFM spectra, i.e. cantilever amplitude versus external magnetic field H_{ext}, of a YIG film in various experimental conditions. (a) Both microwave and the modulation field are turned on, (b) microwave is off and the modulation field is on, (c) microwave is on and the modulation field is off, and (d) both microwave and the modulation field are on again.

When ferromagnetic resonance occurs in a rectangular film, the local magnetic field H satisfies [Mid00]

$$H = \frac{1}{\mu_0}\frac{\omega}{\gamma} - \frac{1}{2}M_s + \frac{1}{4}M_s d[(\frac{\pi}{w})^2 + (\frac{\pi}{l})^2]^{0.5}, \tag{4.7}$$

where ω is the angular frequency of the H_1 field, γ is the gyromagnetic ratio, M_s is the saturation magnetization, d is the film thickness, w is the film width, and l is the film length. In this experiment, one has ω = 4.125 GHz, γ = 28 MHz/mT for YIG [Mid00], M_s = 180 mT for bulk YIG [Cha02], d = 1 μm, w = 35 μm and l = 115 μm. According to Eq. (4.7), the resonant field for the YIG film is calculated to be 61.5 mT. It is in agreement with the experimental result shown in Fig. 4.10. The deviation between the theory and the experimental result may be due to the fact that the local field is the sum of the external field and the gradient field, the latter of which being known only within a few mT. The shape of the YIG film is not exactly rectangular. This might also play a role here.

Concerning the lineshape, theory predicts one principal resonance peak for the applied

modulation scheme [Mid00]. The reason for the appearance of double peaks could lie in local field inhomogeneities. Under this condition, the resonance can be exited at different external fields.

In order to distinguish spurious signals from the resonant ones, two comparative measurements were made by turning off either the high frequency ac field or the low frequency modulation field. In these cases, the resonant condition will not be met and therefore only spurious signals will be detected. As shown in Fig. 4.10 (b) and (c), the resonant signals disappear and only noise is observed in both cases. When the both fields were turned on again, the resonant peaks appeared again as shown in Fig. 4.10 (d). All the results confirm that the resonant signals are true.

In order to test the stability and reproducibility of the constructed f-MRFM, the YIG film was brought into and out of resonance by manually adjusting the strength of the external magnetic field. The adjustment range was within 0.5 mT. As shown in Fig. 4.11, the resonant status of the YIG film is switchable by slightly changing the external magnetic field. This confirms that the f-MRFM is stable and reliable. Furthermore, the result also indicates that the YIG film has a very small FMR linewidth (at least smaller than 0.5 mT). This is in agreement with the fact that the FMR linewidth of YIG is normally smaller than 0.1 mT [Zha98].

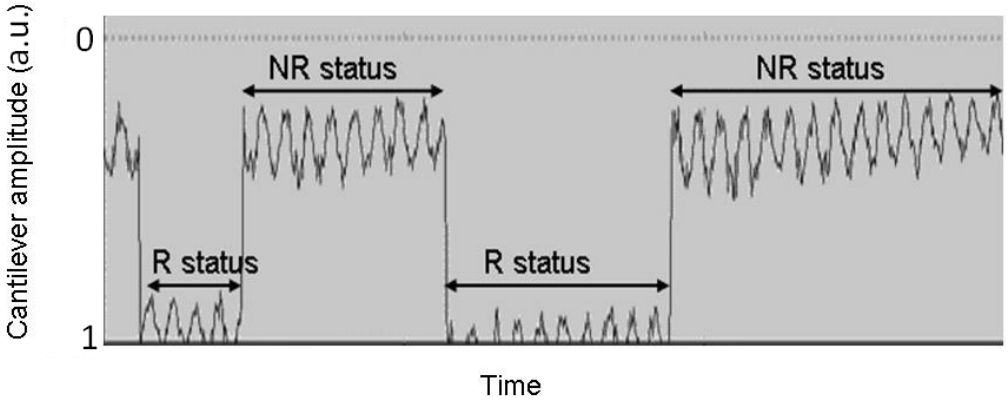

Fig. 4.11 Switch of the resonant status of the YIG film by external magnetic fields. (R status: resonant status; NR status: non-resonant status.)

4.3 Methods to prepare bacteria-on-cantilever samples

Subjected to the limited resolution of the CCD camera, it is a great challenge to manipulate the bacteria (smaller than 5 μm) with a fiber. The method, by which the YIG film was mounted onto the cantilever, is not applicable for magnetostatic bacteria. Furthermore, the attractive force between bacteria and substrates (normally glass or silicon) seems to be very large, which makes the picking-up process quite difficult. In order to resolve these problems, two methods are developed.

4.3.1 Method with a focused ion beam (FIB) system

In a dual beam FIB system, there are an electron beam and a Ga^+ ion beam. The electron beam is applied to do non-destructive imaging for the sample preparation. The Ga^+ ion beam with a low ion beam current (0.3 nA) is used to deposit Pt onto desired locations where the beam is focused. The deposited Pt can connect two separated parts. While, the Ga^+ ion beam with a high ion beam current (5 nA) will etch the surface material away and cut the selected region apart.

Bacteria have been successfully transferred onto a cantilever by the FIB system (Strata DB 235, FEI) in Prof. Mücklich´s group with the help of Dr. Soldera. As illustrated in Fig. 4. 12, the detailed process is as following

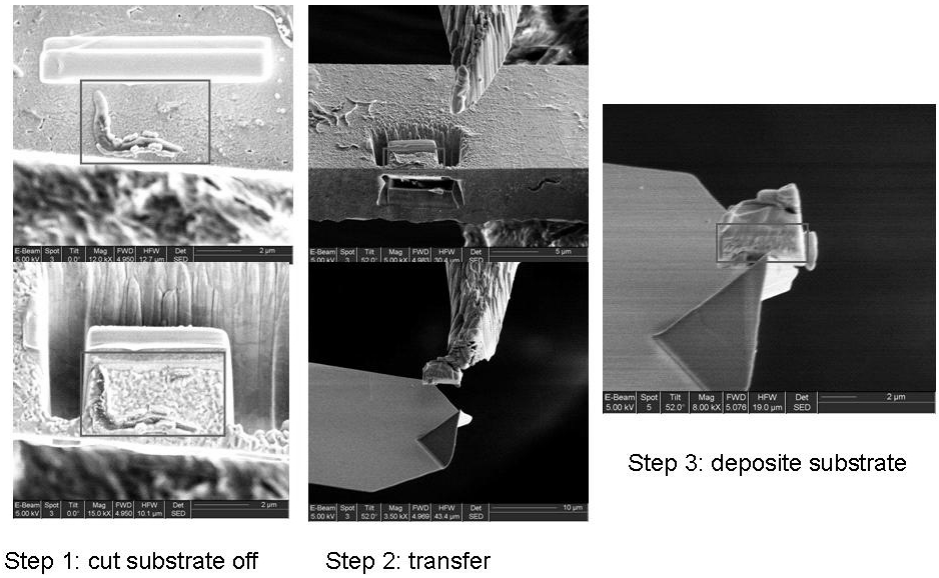

Fig. 4.12 Process of mounting one single bacterium onto a cantilever by a FIB system. The highlighted part in the rectangle is one single bacterium.

Step 1: cut an area containing a desired number of bacteria away from the substrate with a high ion beam current. The cutting process is carried out in two directions, perpendicular to the substrate surface and at a small angle with respect to the surface. Just before being cut off, the desired part is connected to a manipulating tip by the Pt deposition process with a low ion beam current. At the end, the wedge-shaped substrate is cut away from the main substrate.

Step 2: transfer the substrate to the vicinity of a cantilever by the manipulating tip.

Step 3: connect the substrate to the desired position on the cantilever by the Pt deposition process and separate the substrate from the manipulating tip by the cutting process.

The advantage of this method is that the number of the bacteria and the location of the bacteria on the cantilever can be precisely controlled. In practice, however, the method turns out to be very time-consuming. In order to reduce the preparation time, Pt was deposited between the bacteria and the manipulating tip to make a direct connection. But the attempt always failed due to relatively strong interaction between the bacteria and the substrate. This method also introduces unwanted materials to the sample.

4.3.2 Method with a microdroplet

Another method similar to the so called “dip-coating” technique [] was also developed. First, the front end of a cantilever is dipped into a microdroplet of a bacteria suspension, which is attached to the open end of a micropipette. Then bacteria are attached to the cantilever by the capillary force during the drying of the microdroplet. A CCD camera and a micromanipulator are employed for the “dip-coating” process. Finally, the number of the bacteria on the cantilever is checked by SEM.

The number of the bacteria attached by the cantilever can be roughly controlled by adjusting the bacteria concentration of the suspension. With a concentration of 2.5×10^5 bacteria/ml, it is possible to deposit one bacterium or several bacteria onto the cantilever as shown in Fig. 4.13.

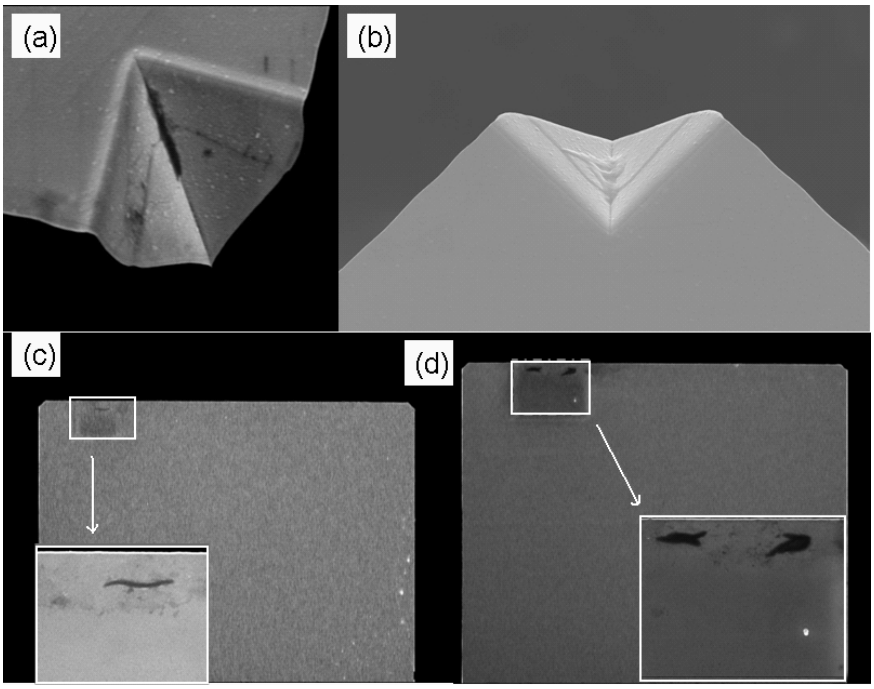

Fig. 4.13 Bacteria deposited on cantilevers. (a) One single bacterium on a cantilever with a tip, (b) several bacteria on a cantilever with a tip, (c) one single bacterium on a tipless cantilever, and (d) several bacteria on a tipless cantilever.

The key points of this method are as following:

(1) For a precise control, the microdroplet of the bacterial suspension should be as

small as tens of micrometers. The microdroplet in this size can be produced by a 5 µl pipette. (2) In order to easily attach bacteria onto the cantilever, it is better to dip the front end of the cantilever from the rim of the microdroplet into the suspension.

For samples with a relatively large quantity of bacteria, the number of the bacteria can be estimated by the total magnetic moment. A cantilever magnetometer measurement [Nga06] was performed for this purpose by Dr. Gysin at Basel University. Figure 4.14 (a) shows the hysteresis loop of one sample, which shows a maximum magnetic moment of about 4×10^{-12} Am^2. Assuming that the magnetic moment of one bacterium is about 8×10^{-16} Am^2 (see section 4.4), the number of bacteria is calculated to be 5000. The result is in agreement with the rough estimation according to the SEM image of the same sample shown in Fig. 4.14 (b).

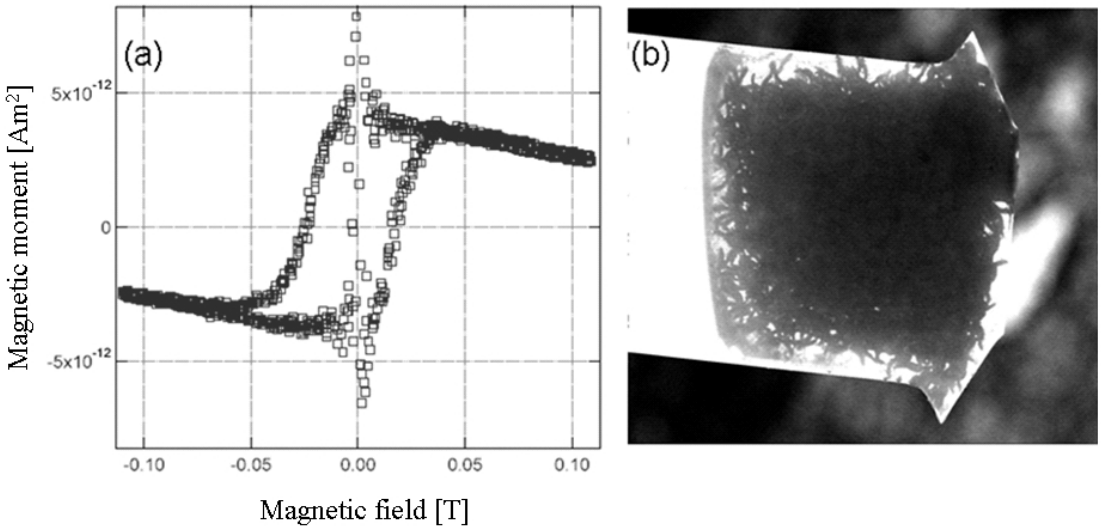

Fig. 4.14 (a) Magnetic hysteresis curve obtained by a cantilever-magnetometer at room temperature and (b) the corresponding SEM image of the measured sample.

Bacteria can be quickly deposited on the cantilever with this method. The number of the deposited bacteria is controllable in a large range from several to thousands. The location of the deposited bacteria can be roughly controlled by the dip depth. According the experience, the process is highly reproducible.

4.4 Discussion on detecting biogenic magnetic particles by ferromagnetic resonance force microscopy

A sample containing thousands of bacteria was analyzed by the f-MRFM. The following parameters were applied in the experiment: T = 300 K (temperature), k = 0.03 N/m (cantilever spring constant), Q = 31 (quality factor), $\omega_0 = 2\pi \times 5.37$ kHz (resonant frequency of the cantilever with bacteria), ∇H = 100 T/m (field gradient), and Δv = 1 Hz (detection bandwidth). With these parameters, according to Eq. 2.37, the minimum detectable magnetic moment would be 1.4×10^{-15} Am^2.

Magnetite nanoparticles from magnetotactic bacteria have an average diameter of 40 nm, and the saturation magnetization of magnetite is 480 kA/m. Assuming that a bacterium contains 50 magnetite nanoparticles, the magnetic moment of one bacterium is estimated to be about 8×10^{-16} Am^2. The magnetic moment of thousands of bacteria is on a level of 10^{-12} Am^2. Though the total magnetic moment of the sample is much less than the sensitivity limit of the conventional FMR spectrometer (10^{-7} Am^2 [Mor03]), it is already large enough to be detected according to the above-estimated sensitivity (1.4×10^{-15} Am^2) of the f-MRFM for our set-up.

However, no ferromagnetic resonant signal was detected in the experiment. The failure may be due to the following reasons.

Two reasons are related to the sample, which could not be changed.

(1) Magnetite is one of the materials with largest FMR linewidths (> 100 mT) [Von66], which broadens the resonant field and thus weakens the FMR signal at individual field strengths.

(2) The FMR resonance only occurs at selected regions where the FMR condition is met. Due to the finite sample extension, magnetic moments of thousands bacteria are not likely to be exited by the high frequency ac field synchronously.

The other four reasons are related to the working conditions of the f-MRFM:

(3) The noise of the present f-MRFM is noticeably larger than the thermal noise. A periodic noise signal is obvious in the f-MRFM spectra of the YIG film (Fig. 4. 10). The noise source is not very clear. Optical interference effects seem not to be the cause as the periodic noise signal varies its strength dramatically upon the presence of the low frequency modulation field. One possible source is from the exposed part of the electronic circuit.

(4) The sensitivity of the present f-MRFM is not optimized due to the relatively small field gradient, the relatively stiff cantilever and low Q factor.

(5) The external magnetic field might not be high enough to reach the main resonant field of the magnetite nanoparticles in bacteria, which are normally between 300 ~ 400 mT according to our conventional FMR measurements (see chapter 5) and to the literatures [Wei04, Kop06a, Kop06b].

(6) There was a large discrepancy between size modulation of the external field H_{mod}^{0} (0.8 mT) and the FMR resonance linewidth of magnetite (100 mT). This leads to a poor performance of the double modulation scheme employed in the experiment (as reported by Dr. I. Knittel).

In order to overcome the above problems, the present f-MRFM can be optimized as following: (1) superconducting magnets would be very helpful to be included in the f-MRFM, which can produce both a local magnetic field with a strength up to 5 T and a large gradient field; (2) soft cantilevers of special design and fabrication ($k < 0.001$ N/m is possible) can be employed to increase the sensitivity of f-MRFM [Ras06]; (3) better shielding and temperature control should be considered to reduce the noise; (4) increase the field modulation amplitude to the order of the FRM linewidth.

From Eq. 2.37, the sensitivity of f-MRFM will be dramatically improved with a great increase of Q factor to a level of 10^4 in vacuum. In order to further decrease the noise,

low temperature environment could also be considered for f-MRFM measurements [Rug92].

With these improvements, detection of magnetite particles in tissues and related issues can be realistically expected. Although it has been proved to be a challenge for experimentalists now, we believe that the success of achieving this goal would justify the effort.

Chapter 5

Structures and properties of magnetite nanoparticle aggregates

In this chapter, the effects of dipolar interactions on the micro-structures and magnetic properties of magnetite nanoparticle aggregates are investigated. Three comparative experiments have been carried out: (1) formation of magnetite nanoparticle aggregates on solid surfaces in external magnetic environments; (2) magnetic properties of magnetite nanoparticles aggregates dispersed in various mediums; (3) ferromagnetic resonance (FMR) of magnetite nanoparticle aggregates. As a whole, these are experimental attempts to understand the interplay of "dipolar interaction, structure formation and physical properties", which is a key issue of many application fields as presented in Chapter 1.

5.1 Formation of magnetite nanoparticle aggregates on solid surfaces in external magnetic fields

Formation of magnetic particle aggregates is fundamentally interesting, as it can directly influence the physical properties of magnetic particle systems. In reality, calculating the properties of magnetic nanoparticle aggregates has been proven difficult due to the complexity of dipolar interactions and the lack of knowledge of the aggregate structures [Ceb83, Don99, She01]. One direct way to obtain information on structure formation is to evaporate the solvent of a magnetic fluid, and to observe the fixed aligned structures on the substrate by scanning electron microscopy (SEM) or transmission electron microscopy (TEM). Chains and two-dimensional ordered lattices of magnetic nanoparticles have been observed in this way [But03, Gam07]. Usually, during the evaporation of the solvent, severe distortions can be caused by the capillary forces [But03, Gam07]. Cryogenic TEM observations provided first direct proofs of dipolar chains of magnetic nanoparticles formed in the liquid phase in the

absence of external magnetic fields [But03]. There, the particle arrangement could be fixed in an undisturbing way during the freezing process. These methods require high vacuum and even low temperature, while providing only two-dimensional information. With convenient performance conditions and the capability of three-dimensional imaging, atomic force microscopy (AFM) has been applied to study particle aggregates of dried magnetic fluids in the absence of external fields [Jey01, Ape05, Gam07]. The dipolar interactions between magnetic particles are relatively weak in that case, and the actual alignment of particle aggregates in fluids may be considerably distorted for the reasons mentioned above.

In this AFM study, the effect of the dipolar interactions is enhanced by external magnetic fields in order to reduce the influence of the capillary forces. Furthermore, though the capillary force could not be avoided in this method, the effect of the dipolar interactions can still clearly be seen from the variety of self-assembled aggregates developed in different external magnetic fields.

5.1.1 Sample preparation and experiments

A commercial ferrofluid (EMG 805, Ferrotec) was used. The magnetic fluid contains 3.6% (in volume) of spherical magnetite nanoparticles. The diameter of the magnetite nanoparticles is about 10 nm. The magnetic fluid was diluted to a volume ratio of 1:1000. Droplets from the given solutions were dried on freshly cleaved mica surfaces in the absence of external magnetic fields or subjected to various external fields. Three types of magnetic fields were applied: a uniform static magnetic field parallel to the mica surface (in-plane), a uniform static magnetic field normal to the mica surface (vertical), and an in-plane rotating magnetic field. The exact size of individual particles was obtained by analyzing a sample at little aggregation, which was prepared from extremely diluted magnetic fluid.

Structures of the particles aggregates were observed by AFM in tapping mode. Commercial cantilevers with a tip radius of 10 nm were employed. The cantilevers

have a resonant frequency of 75 kHz and a spring constant of 3 N/m.

5.1.2 Results and discussion

Figure 5.1 shows an AFM image of individual magnetic nanoparticles and the corresponding cross-sectional profile. The height of the particles lies between 8 and 12 nm. The lateral length of the particles is slightly more than 20 nm. The deviation of the lateral size is caused by the AFM tip curvature, which will be discussed in chapter 6.1.

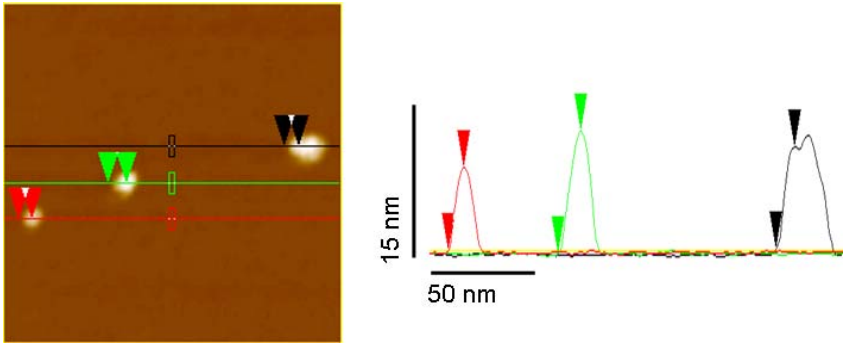

Fig. 5.1 AFM image and profiles of individual magnetic nanoparticles.

Figure 5.2 presents the structures of magnetite nanoparticle aggregates obtained in various external magnetic fields during the drying process.

In the absence of external magnetic fields, the aggregates are randomly distributed all over the substrate as shown in Fig. 5.2 (a). The aggregates appear in diverse structures, including single particles, short chains and clusters. The clusters are irregular with branched and curved structures. The size of these clusters ranges from hundreds of nanometers to a few microns. There is an upper limit of the cluster size, as clusters larger than 3 microns are rarely observed even in large area scans at various sample locations. The shape of clusters and the size limit are similar to those obtained by the numerical simulations based on cluster-cluster aggregation in two-dimensional

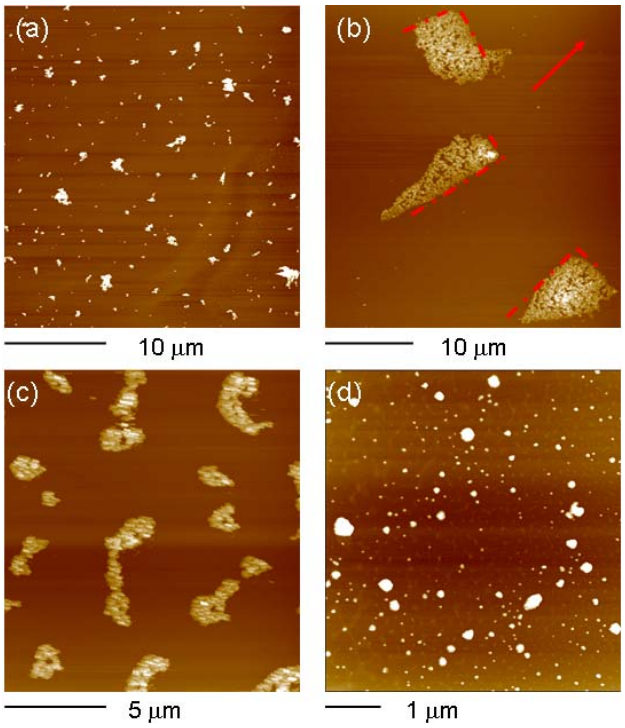

Fig. 5.2 AFM images of aggregates of magnetic nanoparticles formed in various external magnetic fields. (a) In the absence of external magnetic fields, (b) in a 20 mT in-plane static magnetic field, (c) in a 20 mT static magnetic field normal to the surface, and (d) in a 20 mT in-plane rotating magnetic field. The axis of the in-plane field in (b) is indicated by the arrow. Straight edges are highlighted by the dashed lines.

diffusion-limited models for a system of weak magnetic interacting particles [Hel88, Eri89, Sat96, Mor00]. The simulations show that clusters are built up in a confined plane, starting from small sizes, by forming aggregates via dipolar interactions. The strength of the dipolar interactions is characterized by the ratio of magnetic dipolar to thermal energy, $K_{d\text{-}d}$. The results show a significant effect of the dipolar interactions on the formation process of aggregates. The larger $K_{d\text{-}d}$ is, the lower is the fractal dimension D of the formed structures (a straight chain has a D approaching 1) and the higher is the ratio of particles aggregating in large clusters. In the experiment, the motion of magnetite nanoparticles is also essentially limited to the substrate plane as it is assumed in the calculations. According to Ref. [Hel88], $K_{d\text{-}d}$ is calculated to be 1.5 for magnetite particles of 10 nm in diameter at 300 K. With such a small $K_{d\text{-}d}$, the dipolar interactions have only a slight effect on the aggregate formation [Hel88].

When subjected to a 20 mT in-plane static magnetic field, magnetite nanoparticles build up large-sized particle islands, leaving a major part of the substrate bare, as shown in Fig. 5.2 (b). The size of the islands is about 10 μm, much larger than those aggregates generated in the absence of external magnetic fields. The islands in Fig. 5.2 (b) mostly consist of mono- or bilayers of magnetic particles. The dipolar interactions favor the alignment of magnetic particles along the external field. An external magnetic field parallel to the surface will facilitate the islands to spread on the surface, and meanwhile prohibit particles piling up on the surface. The island size can even be extended to several tens of microns by applying higher magnetic fields. One such pattern formed in an in-plane field of 40 mT is presented in Fig. 5.3. A noticeable feature of the particle islands are their largely straight edges, which are marked by the dashed lines in Figs. 5.2 (b) and 5.3. In the simulations, straight edges are found to be formed through chain-chain interactions in external magnetic fields [Hel88, Eri89, Sat96, Mor00]. In the liquid, chains of particles develop via dipolar interactions of particles and interactions of particle moments with the homogeneous external field. For 10 nm magnetite particles, the ratio of the energy of the dipole moment of a particle in a 20 mT homogeneous magnetic field to the thermal energy, $K_{\text{d-f}}$, is 7.3. For $K_{\text{d-f}} > 5$, the particle-field interaction dominates over the particle-particle interaction [Sat96]. As could be shown by simulations, chain structures along the field direction are formed, but also structures on a length scale of several micrometers aligned with the field by chain-chain interaction [Hel88, Eri89, Sat96, Mor00, Lal04].

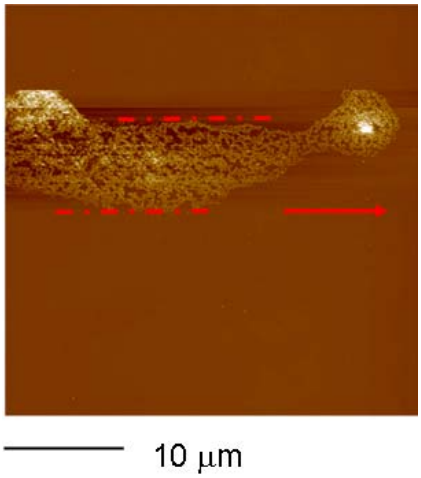

Fig. 5.3 AFM image of aggregates of magnetic nanoparticles formed in a 40 mT in-plane static magnetic field. The field axis is indicated by the arrow.

In the early stage of the drying process, capillary forces are negligible, while in the final stage, they are dominant [But03, Lal04, Gam07]. Capillary forces act to reduce the surface energy by diminishing surface areas, and in consequence the formed assemblies of particles are driven to aggregate. Let us assume particle islands consisting of a monolayer of spherical particles of size a = 10 nm, the islands being squares of size d and being a distance d apart from each other. A schematic drawing of the particle islands is presented in Fig. 5.4. The surface energy of one island edge is given by $E_0 = \sigma \cdot a \cdot d$, for a surface tension of σ. Complete side-by-side contact of two islands reduces the total surface energy of the liquid by approximately $E_S = 2\ E_0$. Other interfacial energies are neglected. The surface force can be approximated by $F_S = E_S/d = 2\sigma \cdot a$. However, the particles are pressed onto the surface by the surface normal force $F_{NS} = 4\partial E_0 / \partial a = 4\sigma \cdot d$. Assuming an empirical friction coefficient α results in a friction force $F_{FS} = \alpha F_{NS}$. For an island of size $d > a/2\alpha$ holds $F_{FS} > F_S$. It will remain unaffected by capillary forces. Therefore, structures already formed in the early stage of drying could persist until complete drying, provided they are sufficiently large. From this, the observed considerable influence of the external field on the ultimately dried pattern can be understood. However, the pattern might still be severely affected by effects related to the dewetting front [Hsu07].

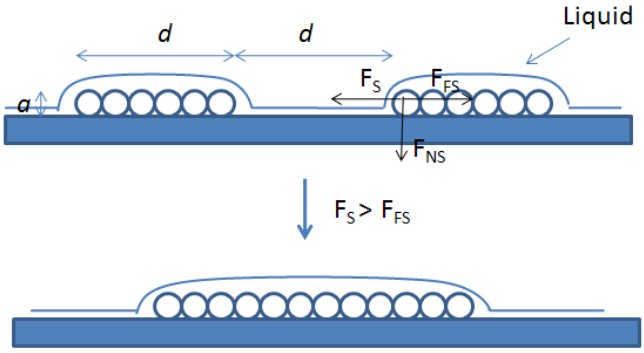

Fig. 5.4 Schematic drawing of particle islands before and after aggregation due to the surface tension of liquid. F_S, F_{NS} and F_{FS} denote the surface force, the surface normal force and the friction force, respectively.

From a high resolution AFM image shown in Fig. 5.5 (a), particles are aligned in chains with their axes along preferentially the external field axis. The result directly manifests the typical structure of interacting dipole chains in the presence of external magnetic fields. The straight chains are mostly found at the edges, while the major part of the particle islands include many branched structures, such as shown in Figs. 5.2 (b) and 5.3. The branching effect is due to the competition between the magnetic dipolar interactions, thermodynamic randomization and other energetically favorable branching processes [Sat96, Psh00, Han02].

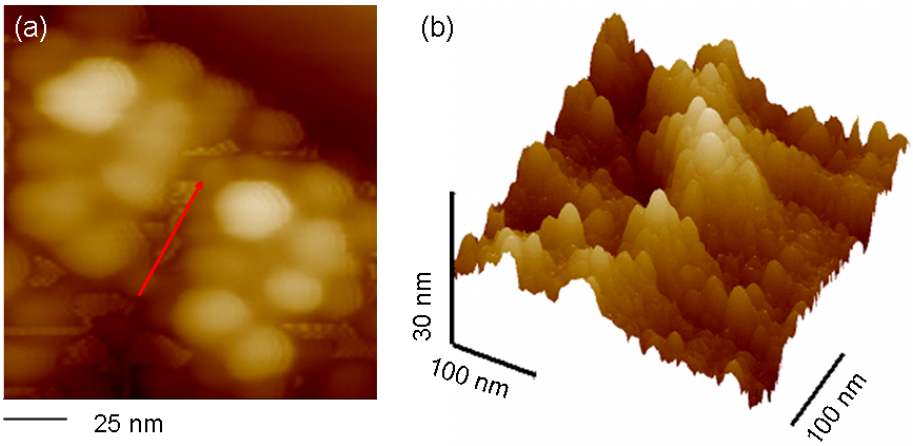

Fig. 5.5 High resolution AFM images of aggregates of magnetic nanoparticles. (a) In a 20 mT in-plane static magnetic field and (b) in a 20 mT static magnetic field normal to the surface. The in-plane field axis is indicated by the arrow.

When subjected to a 20 mT static vertical magnetic field, magnetite nanoparticles are also found in form of particle islands, as shown in Fig. 5.2 (c). Individual particles and short chains are rarely observed. The shape of the particle islands is irregular, and the size is about 5 μm. From a high resolution AFM image as shown in Fig. 5.5 (b), it can be concluded that the topography of the particle islands is quite rough with height variations. In the solution, the magnetic particles are aligned along the external magnetic field, i.e., normal to the surface in this case. After drying, these particles are piled up within the islands, resulting in the observed height variations and rough topography.

As show in Fig. 5.6, the average height of the particle islands for a perpendicular field is 19 nm (about the thickness of two monolayers) in a field of 20 mT and 27 nm (about the thickness of three monolayers) in a field of 40 mT. This result clearly shows the dependence of the shape of the particle islands on the strength of the external fields. From the available data, there is not a big difference in the size for islands formed in perpendicular fields of various strengths.

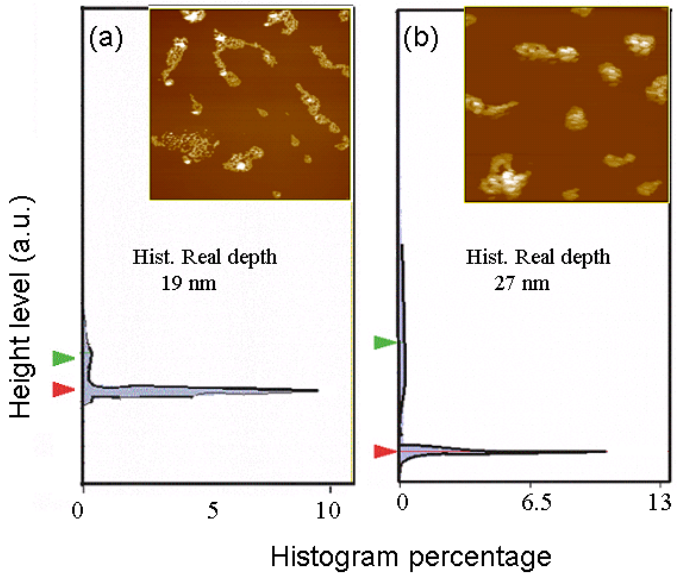

Fig. 5.6 Height distributions of magnetic nanoparticle aggregates. (a) 20 mT and (b) 40 mT static magnetic field normal to the substrate. The percentage values yield the relative surface area covered by particle aggregates of a certain height with respect to the total surface area displayed in the images, respectively. Lower arrows indicate the substrate level and upper ones the averaged level of the islands.

When subjected to a 20 mT in-plane rotating magnetic field (10 Hz), magnetic particles are arranged in form of spherical clusters, as can be seen in Fig. 5.2 (d). The size of the clusters is generally smaller than 500 nm and the majority of them are even smaller than 100 nm. Elongated structures, like chains and branches, tend to break due to the repulsive dipolar interaction, when the external field has an angle of more than 45^{o} with respect to the chain axis [Dav05]. Thus, isotropic spherical structures are favorable in a rotating magnetic field. For the same reason, small spherical clusters are less likely to grow by interconnections. As a result, the observed clusters are relatively small, even compared to those aggregates formed in the absence of external magnetic fields.

5.1.3 Conclusion

Magnetic nanoparticle aggregates were formed on solid surfaces in four kinds of external magnetic fields. The formation of the particle aggregates is strongly influenced by dipolar interactions. Elongated particle islands with largely straight edges are built up along the field axis in in-plane static magnetic fields. Irregular particle islands with a rough topography are developed in static vertical magnetic fields. Spherical clusters with relatively small sizes are formed in in-plane rotating magnetic fields. In the absence of external magnetic fields, diverse structures including single particles of a few tens of nanometers to irregular clusters of a few microns in size have been observed. The typical scale and the height of the particle islands depend on the strength of the applied magnetic fields. The experimental results clearly support previously published numerical simulations on ferrofluids in a two-dimensional diffusion-limited system.

5.2 Magnetic properties of magnetite nanoparticle aggregates in liquid and elastic matrices

Due to complex dipolar interactions between magnetic particles, there is a long-time standing discrepancy between theoretical predictions and experimental results for the magnetic properties of ferrofluids [Dor95, Ewi02, Tak02]. The properties of magnetic beads used in biological applications can be significantly influenced by the dipolar interactions between magnetic particles embedded in the beads [Pan03, Gij04]. In the models of superparamagnetic particle-based magnetoreception in organisms, the dipolar interactions are critical for the behavior of the magnetic particle ensembles [Sch99, Win01, Dav05]. Factors like the particle concentration, the particle size and the dispersion medium, play important roles in the dipolar interactions. In this section, the influence of these factors on the magnetization and susceptibility of systems of magnetic nanoparticles is investigated.

5.2.1 Sample preparation and experiment

Two hexane-based ferrofluids (from Sustech GmbH) were employed. They contain magnetite particles of 10 and 20 nm in diameter, respectively. The weight percentage of the magnetite particles is 5% for both ferrofluids.

The original ferrofluids were diluted to 1.25%, 0.51% and 0.2% (weight percentage of magnetite particles) by pure hexane solvent. The original ferrofluid and its dilutions were used as samples with magnetite particles dispersed in liquid. Paraffin wax (melting point: 50 ^{o}C) was used as elastic matrix for dispersing magnetite particles. The original ferrofluid was added into the melted wax in an ultrasonic bath at a bath temperature of 55 ^{o}C. After 30 min ultrasonication, the bath was slowly cooled down to room temperature. Finally, three samples were prepared with 2.75%, 0.27% and 0.02% (weight percentages) of magnetite particles in the matrix of paraffin wax.

The magnetization of the samples was measured by a vibrating sample magnetometer (VSM). The available homogenous magnetic field has a maximum strength of 1591 kA/m (~ 2 T). The sensitivity of the VSM is about 5 $\times 10^{-8}$ Am^2. The samples were sealed in a small Teflon cylinder (for magnetite particles in liquid) or fixed onto a plastic bar (for magnetite particles in the elastic matrix). The weight of each sample was measured by a sensitive balance. For VSM measurements, the samples were vibrating at 84 Hz with an amplitude of few millimeters. In order to determine initial susceptibilities of samples, the measurements were performed in a relatively low field range up to 20 kA/m. The contribution of diamagnetic materials, like sample holders, was subtracted from the measured data.

The magnetite particles from the ferrofluids and the alignment of magnetite particles on the surface of the paraffin wax were characterized by AFM.

5.2.2 Results and discussion

Figure 5.7 shows the mass magnetization of magnetite particles in liquid and the elastic matrix. Results are compared in term of mass magnetization because the volume of the samples is difficult to be precisely determined. The calculated initial mass susceptibilities are listed in the up-left corner of the figure.

The mass magnetization M_{m} of non-interacting particles as a function of an applied magnetic field H is expressed by [Tak02]

$$M_{\mathrm{m}}(H) = \eta M_s L(\frac{M_s v H}{k_B T}), \tag{5.1}$$

where η, M_{s}, v, k_{B}, and T are the magnetite weight fraction, the saturation magnetization, the particle volume, Boltzmann constant and temperature, respectively. L(x) denotes the Langevin function.

A normalized mass magnetization can be defined as the mass magnetization M_{m}

divided by the weight fraction. According to Eq. (5.1), the normalized mass magnetization curves of the original ferrofluid and its dilutions are expected to be identical. However, as shown in Fig. 5.7 (a), this is not the case. The larger weight fraction a sample has, the larger magnetization is observed at the same applied field. A similar tendency is also observed for the samples with the magnetic particles dispersed in the elastic matrix, as shown in Fig. 5.7 (b). The deviation between the theory and the experiment is indicative of non-negligible dipolar interactions between magnetic nanoparticles. The dipolar interactions tend to stabilize the particles' magnetization in a long-range order and thus against the thermal agitation [Yaf86, Dor95]. This gives rise to a higher magnetization than for a non-interacting system. The dipolar interaction energy of the particles is proportional to the inverse cube of the average interparticle distance [Blu01]. Therefore, ferrofluids with denser magnetic particles exhibit higher magnetization.

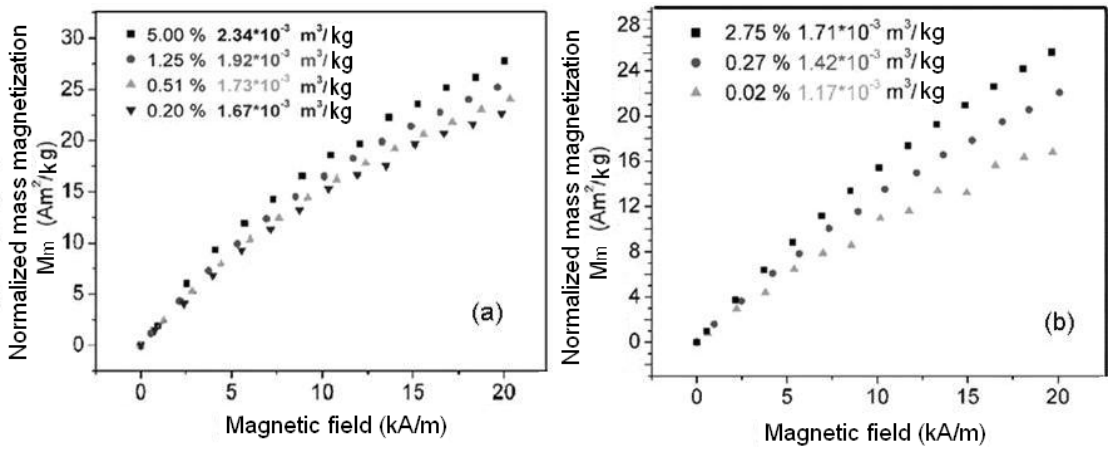

Fig. 5.7 Normalized mass magnetization of magnetic particles dispersed (a) in liquid and (b) in an elastic matrix. The initial mass susceptibilities calculated by Eq. (5.2) are listed in the up-left corner of the figure.

The effective size of the magnetic particles could be estimated from the equation [Ewi02]

$$\chi_m = M_s \frac{\mu_0 M_s v}{3K_B T}\frac{1}{\rho} = M_s \frac{\mu_0 M_s \pi d^3}{18 k_B T}\frac{1}{\rho}, \tag{5.2}$$

where χ_m is the initial mass susceptibility determined from the linear part at the

beginning of the magnetization curve, d is the diameter of the magnetic particles, and ρ is the material density.

Tab. 5.1 Effective diameters of magnetite particles in liquid with various weight fractions.

Magnetite weight fraction	5%	1.25%	0.51%	0.2%
Effective particle diameter (nm)	10	9.4	9	8.9

For magnetite, the bulk saturation magnetization M_s of 4.8×10^5 A/m and a density ρ of 5.17×10^3 kg/m^3 were taken into account [Smi59]. The calculations were performed

Tab. 5.2 Effective diameters of magnetite particles in the elastic matrix with various weight fractions.

Magnetite weight fraction	2.75%	0.27%	0.02%
Effective particle diameter (nm)	9	8.5	7.9

for room temperature, 293 K. The results are listed in Tab. 5.1 and 5.2, respectively. The effective particle size is about 10 nm and in a good agreement with the data from the sample producer. A higher particle concentration gives rise to a larger effective particle size.

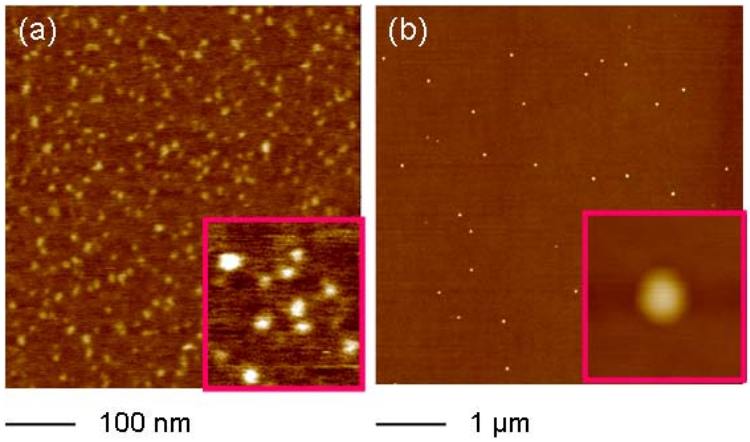

Fig. 5.8 AFM images of magnetite particles. (a) With an average particle diameter of 10 nm and (b) with an average particle diameter of 20 nm. Both insets: 100×100 nm^2.

From Fig. 5.8, the average diameters of magnetite particles in two liquid samples are estimated to be 10 nm and 20 nm, respectively. The magnetization data of these two samples are shown in Fig. 5.9. As the difference in the particle weight fraction is negligible for both samples, the magnetization data indicate that large particles acquire a higher initial susceptibility than small ones.

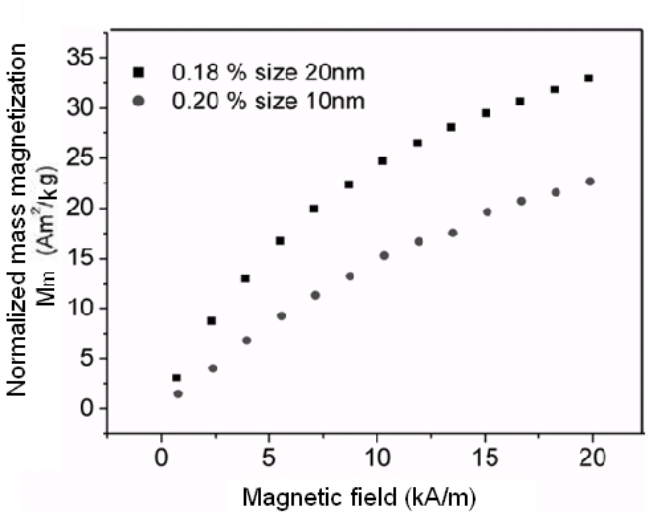

Fig. 5.9 Normalized mass magnetization of magnetite particles of different sizes.

Figure 5.10 presents magnetization curves of the particles dispersed in a liquid and an elastic matrix for comparison. In Fig. 5.10 (a), the sample with 1.25% particle weight percentage in liquid shows a larger magnetization than the sample with 2.75% particle weight percentage in the elastic matrix. This is similar for the sample with 0.2% particle weight percentage in liquid and the sample with 0.27% particle weight percentage in the elastic matrix. For a same weight fraction, the volume fraction of magnetic particles in liquid is smaller than the one in the elastic matrix (the material density of hexane solvent and paraffin wax is 600 kg/m^3 and 900 kg/m^3, respectively). Therefore, a higher magnetization is observed in liquid samples with a smaller volume fraction compared to particles in an elastic matrix. It is contradictive to the results for the magnetic particles dispersed in the same media. Furthermore, from the hysteresis curves shown in Fig. 5.10 (b), the magnetite particles in liquid approach saturation much faster than those in the elastic matrix. In the latter situation, the magnetite

particles are not saturated yet at a field of 800 kA/m. In various dispersion media, the particle mobility and arrangement can be dramatically different. In the elastic matrix, the particles are fixed. The magnetizing

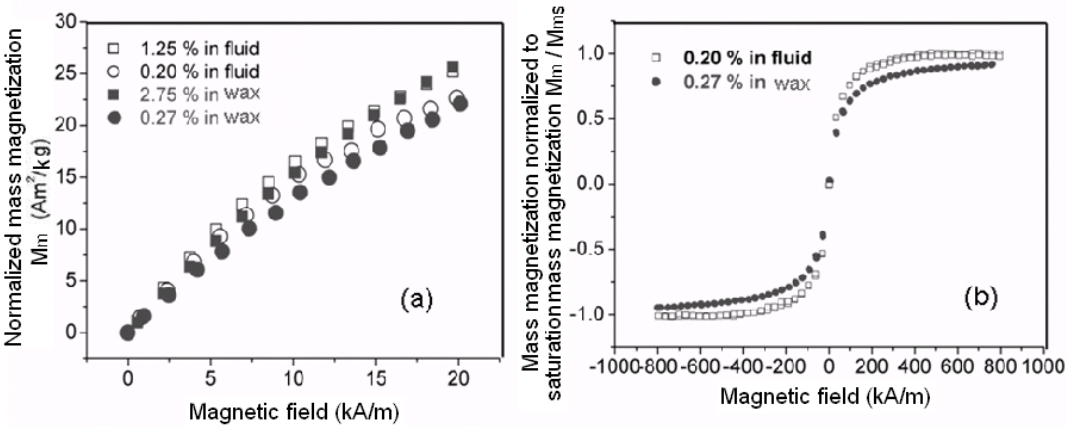

Fig. 5.10 Comparison of (a) magnetization and (b) hysteresis loops of magnetite particles in liquid and the elastic matrix.

process takes place only through the Néel rotation of magnetic moments. In liquid, the easy axis of a particle is free to be aligned along the external field in addition to the Néel rotation. Some kinds of particle arrangements, like closed circuits, zigzag chains and networks, were supposed to be formed in remanence in the simulations [Hel88, Jun95]. The existence of clusters and closed circles of magnetite particles in the elastic matrix were confirmed by the AFM measurement, as shown in Fig. 5.11. When the external field increases, the closed circles will gradually open and the networks will line up along the applied field in liquid to achieve energetically favorable states [Hel88, Jun95]. On contrast, the closed circles and networks in the elastic matrix will remain in the external magnetic field. It requires a higher magnetic field to saturate magnetite particles in these arrangements.

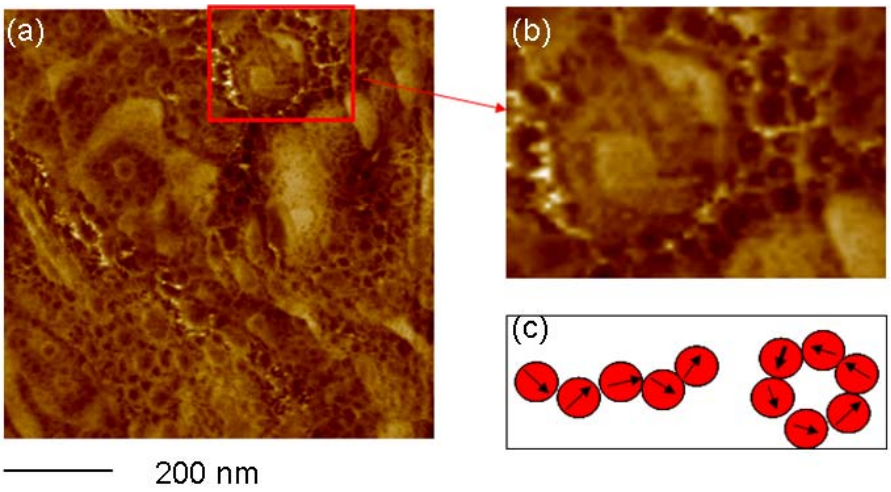

Fig. 5.11 AFM image of (a) magnetite particles dispersed in the elastic matrix, (b) the enlarged part, and (c) schematic drawing of particle arrangements predicted by theoretical simulation.

5.2.3 Conclusion

Parameters, like the particle concentration, the particle size and the dispersion medium, can significantly modify the properties of magnetic nanoparticle aggregate via dipolar interactions. Higher susceptibility is obtained for magnetic particles with a higher particle concentration in the same dispersion medium. The dipolar interactions play a role to stabilize the particle magnetization against thermal agitation, which has the same effect an enlargement of the effective size of the particle. The dispersion media can significantly influence the particle mobility and arrangement.

5.3 Assessment of the magnetostatic interactions of magnetite nanoparticles by ferromagnetic resonance

In situ non-destructive assessment of the magnetostatic interactions of magnetic nanoparticles is of particular interest, where the original arrangements of the particles are easy to be destroyed by extraction. Important information on the size and the shape distribution of magnetic nanoparticles and on the arrangement of particles is expected to be obtained from the assessment. Conventionally, rock magnetism

techniques [Cis81, Mos93], like anhysteretic remanent magnetization, isothermal remanent magnetization and the Moskowitz test, are applied for *In situ* non-destructive analysis of magnetostatic interactions. However, these rock magnetism techniques are relatively complicated and time-consuming (see the procedure in Section 6.3). The FMR (ferromagnetic resonance) technique was recently introduced as an alternative approach to assess the magnetostatic interactions of magnetite nanoparticles in organisms [Kop06b]. The FMR technique is very sensitive to variations of magnetic anisotropy fields and the experiment can be rapidly completed. Biogenic magnetite particles in both living magnetotactic bacteria and bacterial magnetofossils can be distinguished from other synthesized magnetite particles by their special features in the FMR spectra [Wei04, Kop06a]. These special features include low-field secondary absorption peaks, positive uniaxial anisotropy and a relatively small effective gyromagnetic ratio. These features are supposed to arise from unique intracellular chains of magnetite nanoparticles. FMR was mainly performed in aqueous solution. In this section, a systematic FMR study on *Magnetospirillum gryphiswaldense* MSR-1 bacteria (*M. gryphiswaldense*), magnetite nanoparticles extracted from *M. gryphiswaldense*, and on other synthetic magnetite nanoparticles will be presented. In contrast to previous work done in an aqueous environment, all samples under study were deposited onto well-defined surfaces. An external field was applied during the drying process of the solutions in order to produce a preferred orientation for particle assemblies.

5.3.1 Sample preparation and experiment

The wild type strain *M. gryphiswaldense* were grown microaerobically in a 100 ml culture volume at 28 °C under moderate shaking (100 rpm) in modified flask standard medium. The detailed process is described in Ref. [Lan06]. The *M. gryphiswaldense* sample contained 2.55 $\times 10^9$ cells/ml. 2% (g/ml) formaldehyde was added in order to crosslink the proteins in order to fix the bacterial shape.

For the production of biogenic magnetite particles, *M. gryphiswaldense* were cultivated in a modified Biostat A twin dual vessel laboratory fermenter (B. Braun Biotech International GmbH), which was previously described in Ref. [Hey03]. The bacteria were grown at 0.125 mbar of oxygen under stationary condition for 24 h. The procedure for purification was chosen according to the work by Grünberg et al. [Grü04]. The bacterial cells were disrupted by 3 passages through a French Press at 1260 bar. The cell debris was removed by centrifugation at 800 g (the earth's gravitational field) for 5 min. The cleared cell lysate was passed through a magnetic separation column (Miltenyi Biotech GmbH). The column-bound magnetite particles were washed by 50 ml of EP (10 mM Hepes, 1 mM EDTA pH7.4), HP (10 mM Hepes, 200 mM NaCl, 1 mM EDTA pH7.4) and water. Subsequently the magnetite particles were centrifuged at 2×10^5 g for 90 min. Finally, the magnetite particles were resuspended in 2 ml of EP.

Commercial synthetic magnetite nanoparticles and magnetite-containing polymeric composite particles were chosen for reference. MSG W11® is a ferrofluid product (Ferrotec GmbH), containing magnetite nanoparticles (2.8-3.5% in volume, 10 nm in diameter). M1-180/20® (Merck Chemie SAS) are polymeric microspheres (0.96 μm in diameter) with embedded magnetite nanoparticles (23.7% in weight, 20 nm in diameter). Nanomag®-D–spio (Micromod Partikeltechnologie GmbH) consist in a small number of spheric magnetite nanoparticles (35% in weight, 10 nm in diameter) embedded in a matrix of dextran (50 nm in diameter).

4 ml of each sample was picked up from the solution and deposited onto a freshly cleaved mica surface by a pipette. The sample was then dried in air in an external homogeneous magnetic field of about 45 mT, which was produced by a strong horseshoe magnet. This external field and the field direction will be referred to as the “alignment field” and the “alignment direction”, respectively. The particles form a layer of varying thickness.

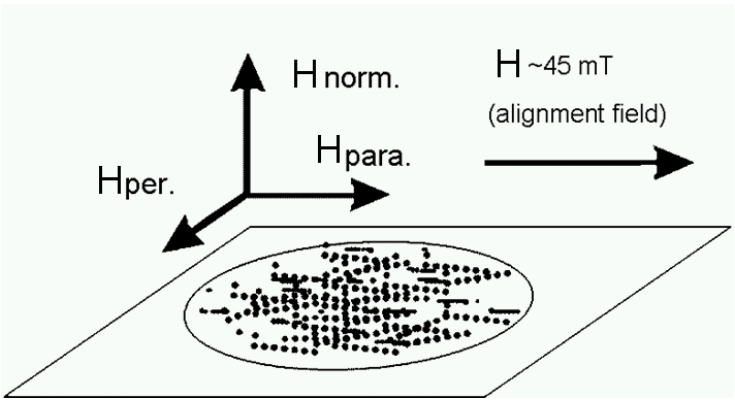

Fig. 5.12 Magnetic field orientations. $\mathbf{H}$ is the external homogeneous magnetic field applied during the drying process. $\mathbf{H}_{para.}$, $\mathbf{H}_{per.}$, and $\mathbf{H}_{norm.}$ are the magnetizing fields in FMR measurements.

Ferromagnetic resonance spectra were acquired using an X-band Bruker ESP 300E Spectrometer. The employed frequency was 9.85 GHz and the power was set to 64 μW. The modulation frequency and the field amplitude were 100 kHz and 1 mT, respectively. Perpendicular to the microwave magnetic field, a magnetizing field was swept from 0 to 800 mT to accomplish one measurement. Since all the samples contained sufficient ferromagnetic material, one sweep was sufficient to obtain a reasonably good FMR spectrum. For each sample, three orientations have been chosen relative to the alignment field: the magnetizing field applied parallel to the alignment direction ($\mathbf{H}_{para.}$), perpendicular to the alignment direction within the substrate ($\mathbf{H}_{per.}$), and normal to the substrate ($\mathbf{H}_{norm.}$), as illustrated in Fig. 5.12.

5.3.2 Results and discussion

All measured spectra are presented in Fig. 5.13 and the fit parameters are listed in Tab. 5.3. As a rough overview over the spectral characteristics, three phenomenological parameters are used: effective *g* factor, linewidth factor and asymmetry factor. The effective *g* factor is associated with maximum absorption through $g_{eff} = h\nu/\mu_B H_r$. Here, H_r is the experimental field value at maximum absorption. The linewidth factor ΔH is

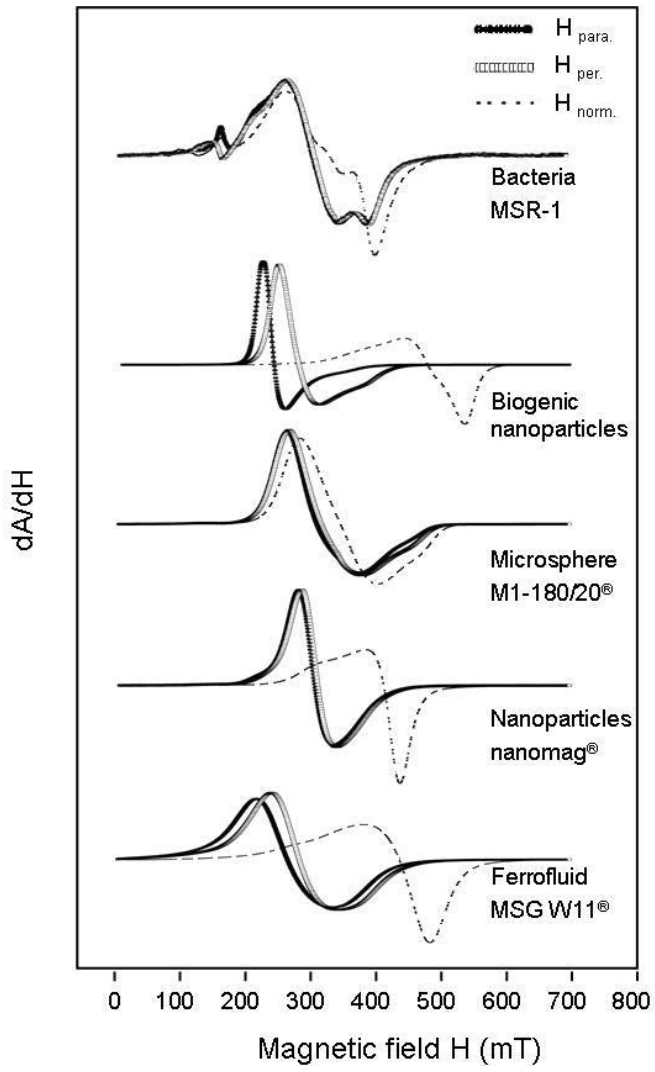

Fig. 5.13 FMR Spectra of the samples.

asymmetry factor F_A denotes the asymmetry ratio between the low-field and the high-field part of the absorption peak, $F_A = \Delta H_{high}/\Delta H_{low}$. H_r, ΔH and F_A are determined from the spectra, as indicated in the Fig. 5.14. Although all these parameters are derived from the absorption spectrum, FMR spectra are generally given by the first derivative of the absorption curve.

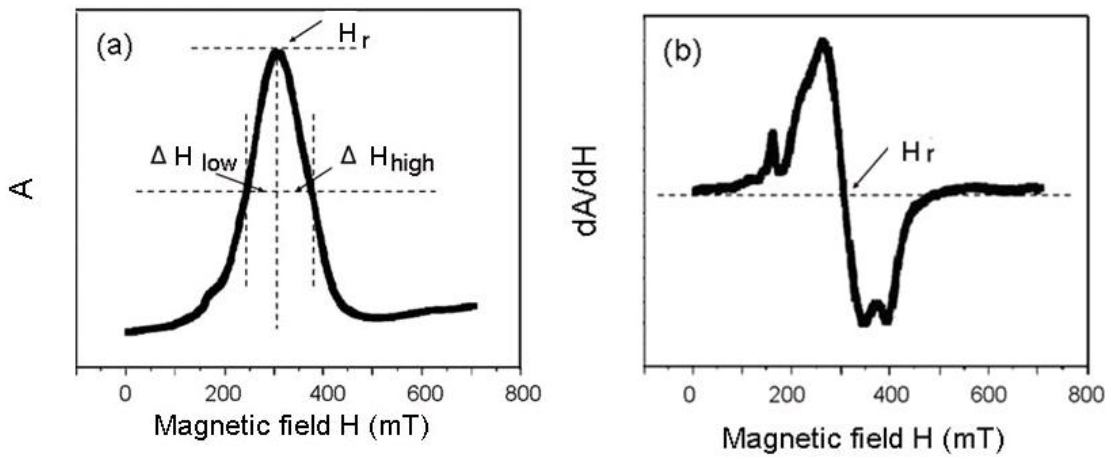

Fig. 5.14 (a) Absorption and (b) derivative spectra with characteristic field values.

Among all the results, MSR-1 bacteria have the most complicated FMR spectra involving multiple absorption peaks. When the magnetizing field is applied in plane, the slight difference in the spectra for two magnetizing field orientations ($\mathbf{H}_{para.}$ and $\mathbf{H}_{per.}$) is unexpected. The alignment field applied during the bacteria deposition process should to some extent align the bacteria along its orientation. A shift of absorption peaks would occur by changing the relative orientation of the sample with respect to the magnetizing field. Since this is not the case, the result indicates that magnetic alignment is weak during the bacteria deposition process. Four well-defined peaks are found at around 165, 265, 350 and 390 mT, respectively. Between the first two peaks, there is a broad shoulder. The main resonance field is about 307 mT, determined by the zero-crossing point in the spectrum. Accordingly, the deduced effective g factor is 2.26. This is larger than the value calculated for bulk magnetite (2.12) [Bic50]. With asymmetry factors of 1.15 and 1.05, the spectra do not show a clear low-field tendency (a tail asymmetrically extending in the low field direction) as observed in early studies [Wei04, Kop06a, Kop06b]. When the magnetizing field is applied normal to the plane, the shoulder at the low-field part disappears. Between two main absorption peaks, there are ripple-like structures instead of secondary peaks in the spectrum. The main resonance field is shifted to a higher value of 320 mT. The asymmetry factor is found to be 0.97. This indicates that stronger absorption occurs at

the high field part.

Tab. 5.3 Summary of FMR analysis

		$\mathbf{H}_{\text{para.}}$ (mT)	$\mathbf{H}_{\text{per.}}$ (mT)	$\mathbf{H}_{\text{norm.}}$ (mT)
Ferrofluid	g_{eff}	2.63	2.45	1.59
	ΔH	125.5	129	122.4
	F_{A}	1.35	1.28	0.64
Nanomag composite particles	g_{eff}	2.27	2.24	1.68
	ΔH	81.0	77.5	93.2
	F_{A}	1.45	1.4	0.52
Microsphere composite particles	g_{eff}	2.25	2.20	2.01
	ΔH	123.2	111.8	117.6
	F_{A}	1.63	1.24	0.92
Biogenic particles	g_{eff}	2.91	2.52	1.46
	ΔH	52.1	87.7	119.8
	F_{A}	1.91	1.85	0.83
M. gryphiswaldense Bacteria	g_{eff}	2.28	2.25	2.09
	ΔH	130.9	125.5	155.1
	F_{A}	1.15	1.05	0.97

Except MSR-1 bacteria, all samples show only one broad secondary peak. The spectra of the biogenic nanoparticles are the most asymmetric ones. The absorption curves show long tails extending to the high-field range for an in-plane magnetizing field, while the inverse tendency is observed for a normal magnetizing field. The dependency of asymmetry on the magnetizing field orientation is similar to that of the other samples of particles, except that of M1-180/20® microspheres. The main resonance field for biogenic nanoparticles is shifted by 38 mT towards higher fields, when $\mathbf{H}_{\text{para.}}$ is changed to $\mathbf{H}_{\text{per.}}$. The main resonance field increases significantly by 200 mT, when $\mathbf{H}_{\text{per.}}$ is changed to $\mathbf{H}_{\text{norm.}}$. The spectra of ferrofluid MSG W11® are the most symmetric ones. The absorption peaks are broad and the secondary peaks have almost been smeared out. The difference in the main resonance field is 19 mT

between the spectra measured for $\mathbf{H}_{para.}$ and $\mathbf{H}_{per.}$, and 155 mT between the spectra for $\mathbf{H}_{per.}$and $\mathbf{H}_{norm.}$. In case of Nanomag® particles, only a slight difference in the main resonance field is observed for spectra measured for $\mathbf{H}_{para.}$ and $\mathbf{H}_{per.}$. The difference in the main resonance field between the spectra for $\mathbf{H}_{per.}$and $\mathbf{H}_{norm.}$ is relatively small, about 101 mT. In contrast to the other samples, for M1-180/20® microspheres, the spectrum is independent of the magnetizing field orientation. The spectra show the smallest shift in the main resonance field in various magnetizing fields. As magnetite particles are embedded in a polymer matrix, there is no significant effect of the alignment field. When the magnetizing field is normal to the substrate, the shift of the main resonance field is larger than 100 mT for biogenic magnetite nanoparticles, ferrofluid MSG W11® and Nanomag® particles. This is caused by the demagnetizing field of the layer-like samples. For planar magnetic samples, the in-plane internal field among particles acts to assist the external field, while the out-of-plane internal field opposes the external field [Gri88]. The reversal of the spectrum asymmetry upon changing the orientation of the magnetizing field from in-plane to normal to the plane reflects the direction-dependent magnetostatic interaction among particles, as observed for continuous magnetic thin films [Gri88]. For M1-180/20® microspheres, the diameter of the polymer matrix is about 1 μm, and the embedded magnetite nanoparticles all experience a similar demagnetizing field without much influence from neighboring microspheres. These M1-180/20® microspheres behave like being completely separated from each other in the FMR experiments.

5.3.3 Model calculations

In order to interpret the observed FMR spectra, modelling was performed on the basis of theories by Griscom [Gri81] and Kopp [Kop06a]. The samples consist of an assembly of single-domain particles and these particles are small with respect to the microwave skin depth (about 5 μm for magnetite) [Gri74]. The particles are almost spherical. Thus the shape anisotropy does not play a role in modelling. As the magnetocrystalline anisotropy is not the dominant factor determining the internal field

of bacterial magnetite nanoparticles [Wei04], it is neglected as well. The net magnetization vector approaches the external field direction in the presence of a strong magnetizing field during the FMR measurements. As the particles are densely distributed on the substrate, the complete layer of particles is treated as a film [Gri88]. The demagnetizing field $\mathbf{H}_{\mathrm{de,film}}$ of the film is employed as a fit parameter. The net dipolar field of the surrounding particles felt by particle *i* is given by

$$\mathbf{H}_{\mathrm{di},i} = \sum_{j \neq i} (1/4\pi)[\mathbf{m}_j / r_{i,j}{}^3 - 3\mathbf{r}_{i,j}(\mathbf{m}_j \cdot \mathbf{r}_{i,j}) / r_{i,j}{}^5], \tag{5.3}$$

where $\mathbf{m}_j$ are the magnetic moments of all particles interacting with particle *i* and $\mathbf{r}_{i,j}$ are the distance vectors between the two interacting magnetic dipoles.

In the following, we consider the particular case that particles are aligned in chains. When FMR is obtained, the moments of magnetite particles are aligned along the magnetizing field. The angle θ defined by the magnetic moment $\mathbf{m}_j$ and the distance vector $\mathbf{r}_{i,j}$ is constant in this case. Then, the effective component of the dipolar field of the chain is given by

$$H_{\mathrm{di},i} = \sum_{j \neq i} (1/4\pi)(m_j / r_{i,j}{}^3)(1 - 3\cos^2\theta). \tag{5.4}$$

The resonance field, at which the maximum absorption occurs, is then given by

$$H_{\mathrm{r},i}(\theta) = H_{\mathrm{r},0} + H_{\mathrm{di},i} + H_{\mathrm{de,film}}. \tag{5.5}$$

The resonance field in the absence of anisotropy is determined by $H_{\mathrm{r},0} = h\nu/\mu_0\mu_{\mathrm{B}}g$, where *h* is Planck's constant, ν the microwave frequency, μ_{B} the Bohr magneton, and *g* the gyromagnetic ratio.

Alternatively, we consider a planar assembly of isolated particles. Particles are inhomogenously distributed on a surface. Following Refs. [Kop06a, Kop06b], each

particle is subject to an effective uniaxial shape anisotropy of random orientation, arising from its magnetic dipolar interaction with of a random environment. The resonance field, is then given by

$$H_{\mathrm{r},i}(\theta) = H_{\mathrm{r},0} - 0.5H_{\mathrm{an}}[(3\cos^2\theta - 1) + (K_2/K_1)(8\cos^2\theta\sin^2\theta - 2\sin^4\theta)] + H_{\mathrm{de,film}} \tag{5.6}$$

where we employed the uniaxial anisotropy energy, $E = K_1\sin^2\theta + K_2\sin^4\theta$, and followed the approach of Ref. [Gri81]. H_{an} is the uniaxial anisotropy field given by $2K_1/M_{\mathrm{s}}$.

To compute the absorption at the applied magnetizing field, a Gaussian broadening function of linewidth σ is applied. When the external field is applied in plane, the absorption A is obtained from

$$A(H) = \frac{\sqrt{2\pi}}{\sigma}\int_{\theta=0}^{\pi/2}\sum_{i=1}^{N} \exp(-(H - H_{\mathrm{r},i}(\theta))^2/2\sigma^2)\sin\theta d\theta, \tag{5.7}$$

with $H_{\mathrm{r},i}$ from Eq. (5.5) or (5.6). When the magnetizing field is applied normal to the plane, the angle is 90^{o}. Gaussian broadening represents a number of physical effects, including those associated with the heterogeneity of size, shape, crystal orientation, arrangement, and composition.

According to the model, the fit parameters are the particle diameter, the center-to-center distance, the chain length, the Gaussian broadening linewidth, the uniaxial anisotropy, the ratio of the first-order anisotropy constant to the second-order one, the demagnetizing field and the *g*-factor. The particle diameter and the center-to-center distance between particles could be obtained from TEM observations.

The parameters are determined from best fits of position and intensity of each experimental absorption peak. In some cases, two sets of fit parameters are employed, as the spectrum of real samples is always a combination of classes of population, e.g. isolated particles and particles in chains or particles in aggregates.

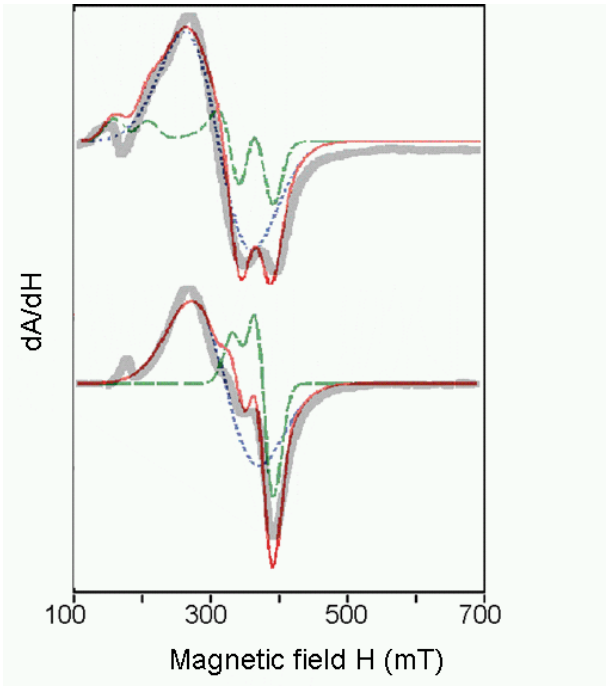

Fig. 5.15 Modelled FMR spectra of *M. Gryphiswaldense* MSR-1 bacteria. Magnetizing field in-plane (upper) and normal to the plane (lower). Dashed green line: component for particles in chains, dotted blue line: component for isolated particles, red solid line: superposition of both components, gray solid line: experimental spectrum.

The modelled spectra for bacteria samples are shown in Fig. 5.15 and the fit parameters are listed in the upper part of Tab. 5.4. The value of the magnetic moment **m** of the particles is given by

$$|\mathbf{m}| = (\pi/6) d^3 M_s , \qquad (5.8)$$

where d is the particle diameter and M_s is the saturation magnetization of bulk magnetite.

From the TEM image of biogenic nanoparticles shown in Fig. 5.16, the average diameter of the particles is 30 nm and the average center-to-center distance between nearest neighbors is 32 nm. Taking M_s = 480 kA/m [Smi59], $|\mathbf{m}|$ is then calculated to be 6.8×10^{-18} Am^2 which was applied in the calculations. In addition to one set of parameters representing interacting particles aligned in chains, another set

representing isolated particles turned out to be necessary for a reasonably good fit.

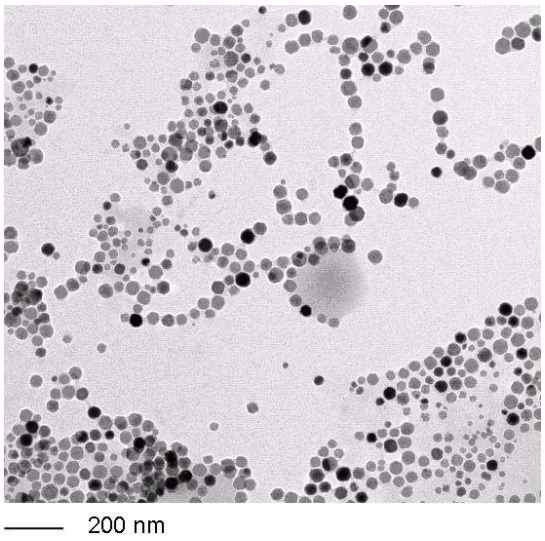

Fig. 5.16 TEM image of biogenic nanoparticles from *M. Gryphiswaldense* MSR-1 bacteria.

The presence of isolated particles is likely to be due to vacancies in the chains, distortions and disaggregation during the cell treatment [Kop06a, Kop06b, Lan06]. In case of in-plane magnetizing fields, the best fit is obtained when the average chain length is equal to 5 particles. This is shorter than the length obtained from TEM observations, where often bacteria with chains of about 20 particles are found. The reduced chain length in the simulation could be the result of curved or broken chains, which lead to a shorter average length. Additionally, the deduced center-to-center distance might be smaller than the real one, which overemphasizes the dipolar interactions and leads to a similar result as obtained for longer chains with a larger center-to-center distance between particles. In case of the magnetizing field normal to the substrate, the best fit is obtained with a chain length of 7 particles. The modelled spectra are illustrated in the lower part of Fig. 5.15. The average angle between magnetizing field and chain axis is set to 71.1^{o} instead of 90^{o} in order to better model the ripple-like structures superimposed to the main absorption peak. Deviation from 90^{o} might be due to the fact that the chains in the bacteria body are not necessarily parallel to the substrate.

Tab. 5.4 Parameters for FMR modelling

	Particle diameter (nm)	Particle number	Center-to-center distance between particles (nm)	σ (mT)	H_{an} (mT)	K_2/K_1	$H_{de,film}$ (mT)
Bacteria	30	5	32	15	-	-	40
($\mathbf{H}_{para.}$ and $\mathbf{H}_{per.}$)	30	1	-	50	-	-	15
Bacteria	30	7	32	15	-	-	10
($\mathbf{H}_{norm.}$)	30	1	-	50	-	-	0
Biogenic particles ($\mathbf{H}_{para.}$)	-	-	-	18	-82	-0.1	65
Biogenic particles ($\mathbf{H}_{per.}$)	-	-	-	30	-82	0	30
Biogenic particles	-	-	-	25	88	-0.17	-120
($\mathbf{H}_{norm.}$)				25	0	0	-190

When the magnetizing field is normal to the substrate, the secondary peak at the field of 160 mT could not be modelled. This peak is corresponding to a g factor of 4.3, which might be caused by free Fe^{3+} ions [Waj00, Jai01]. Fe^{3+}, which exists in the culture medium of bacteria, might absorb to the surface of the cells. In the spectra of extracted magnetite nanoparticles, there is no absorption peak at the corresponding position.

Modelled spectra of biogenic magnetite nanoparticles are shown in Fig. 5.17 and the corresponding parameters are listed in the lower part of Tab. 5.4. Biogenic and synthetic magnetite nanoparticles are arranged in a disordered network with a preferred axis along the alignment direction. Therefore, modelling is based on an uniaxial anisotropy, represented by H_{an} in Eq. (5.6). When the magnetizing field is applied in plane, both resonances are asymmetric, with a high-field tendency, as shown in the upper and middle of Fig. 5.16. In the model, an anisotropy field of -82 mT is employed. Such a negative anisotropy is suitable to the magnetostatic interactions within a planar particle aggregate [Gri88, Kop06a]. The anisotropy enhances the magnetizing field, shifting the resonance to a lower field.

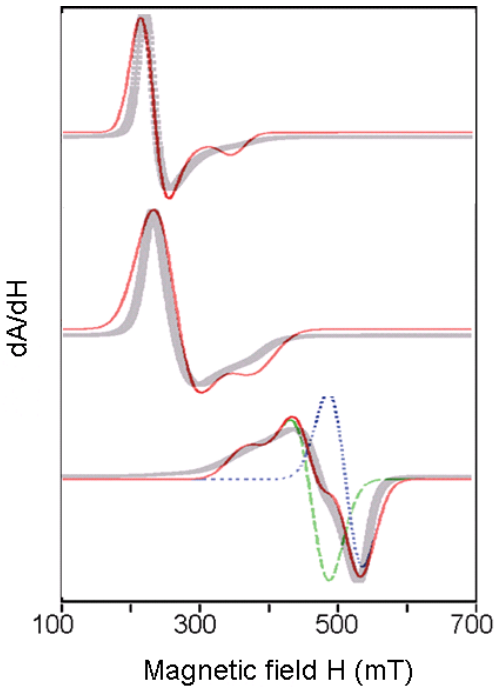

Fig. 5.17 Modelled FMR spectra of biogenic nanoparticles for $\mathbf{H}_{para.}$ (upper), $\mathbf{H}_{per.}$ (middle), and $\mathbf{H}_{norm.}$ (lower). Dashed green line: component for particles in chains, dotted blue line: component for isolated particles, red solid line: superposition of both components, gray solid line: experimental spectrum.

This interpretation is confirmed by changing the magnetizing field's orientation: when it is applied normal to the substrate, the spectrum exhibits a low-field tendency as shown in the lower part of Fig. 5.17. This indicates that the anisotropy changes sign. The spectrum is well fit by a combination of particles with a positive uniaxial anisotropy field of 88 mT and additional isolated particles without any anisotropy. In a magnetizing field normal to the substrate, the dipolar fields between particles are oriented opposite to the magnetizing field [Gri88]. The role of magentostatic interaction in this situation is like that of a positive anisotropy, i.e., increasing the resonance field and causing a low-field tendency.

5.3.4 Conclusion

We have deposited intact *M. Gryphiswaldense* bacterial cells, as well as biogenic and synthetic magnetite particles onto smooth surfaces for FMR investigations. During deposition and during the drying process, samples were subjected to external

alignment by magnetic fields, and were partly aligned. FMR measurements were performed with the magnetizing field along various directions. The arrangement of magnetite particles determines the magnetostatic interactions. The latter then influence the FMR spectra. Modelling of the spectra of bacterial cells was performed including magnetic dipolar interactions. The results prove that the most distinguished feature of bacterial FMR spectra arises from the chain arrangement of the particles. Other samples of individual magnetite particles could better be modelled in terms of a random uniaxial anisotropy. In all cases modelling well reproduces the experimental FMR spectra for the different magnetizing field orientations. The FMR spectra of biogenic magnetite particles show a narrower linewidth, and are more dependent on the orientation of the magnetizing field than those of synthetic magnetite particles. This can ultimately be attributed to the strict biological control of particle growth, resulting in narrow size and shape distributions and high material purity.

Chapter 6
Study of biogenic magnetite nanoparticles

In this chapter, biogenic magnetite nanoparticles from bacteria and fishes are systematically studied by AFM and MFM. Single magnetite particles were extracted from *Magnetospirillum gryphiswaldense* MSR-1 bacteria (*M. gryphiswaldense*). The size of the magnetite particles was determined in an accurate way by employing AFM tip deconvolution procedures. The magnetic structure and behavior were observed by MFM in remanence and in externally applied magnetic fields. Clusters of magnetite particles were obtained from adult salmons. In addition to AFM and MFM investigations, the magnetic behavior of the clusters was studied by modelling. The model is based on the assumption of purely dipolar interactions between the particles. The plausibility of clusters as functional elements in magnetoreception is discussed. MFM was also applied as a tool to locally explore magnetic particles/clusters in tissue slices from Tilapias fish in combination with global analysis done by conventional magnetic tests.

6.1 Single magnetite nanoparticles from bacteria

Among magnetic nanoparticles, biogenic magnetite nanoparticles attract particular interest due to their unique magnetic characteristics and due to their biocompatibility [Ban05, Zha06]. Magnetite nanoparticles are ideal for cell isolation and purification, biomolecular labelling and immobilization, drug targeting, hyperthermia therapy and as contrast agents for magnetic resonance imaging [Mat87, Yoz03]. Attempts to produce magnetite nanoparticles by growing magnetotactic bacteria have been made ever since intracellular chains of magnetite crystals were first found by Blakemore [Bla75, Hey03]. However, the technological application of biogenic magnetite nanoparticles is still hampered by their limited availability. Recently, large-scale production of magnetite nanoparticles was realized utilizing *M. gryphiswaldense*, which are more oxygen tolerant than other magnetotactic bacteria. They thus can be grown in simple liquid media [Lan06, Sun08]. This motivates the analysis of individual magnetite nanoparticles from *M. gryphiswaldense*.

AFM and MFM have indeed yet been successfully employed to characterize magnetite nanoparticles from *M. gryphiswaldense* [Alb05, Ebe05]. When the radii of the particles under study are comparable to the curvature of AFM tips, the obtained AFM results are likely to

deviate from reality and thus from those observations by means of scanning electron microscopy (SEM) or transmission electron microscopy (TEM) [Ras02, Ped03]. A proper tip convolution procedure is needed then. Previous MFM measurements were mainly performed in remanence [Alb05, Ebe05]. In this section, a systematic AFM and variable-field MFM study on magnetite nanoparticles from *M. gryphiswaldense* is presented. The size distribution of the magnetite nanoparticles has been analyzed and precisely determined. For the first time the individual magnetic behavior of single magnetite nanoparticles has been directly analyzed as a function of the environmental configuration by experimental as well as theoretical means.

6.1.1 Sample preparation and experiments

M. gryphiswaldense were cultured as described in chapter 5.3.1 or in ref. [Lan06]. Magnetite nanoparticles were extracted from the bacteria. For details, please refer to also chapter 5.3.1.

A droplet of highly diluted aqueous suspension of magnetite nanoparticles was deposited onto a freshly cleaved mica surface and subsequently dried in air. During the drying process, the sample was placed between the poles of a strong horseshoe magnet, which produces a homogenous in-plane magnetic field of 45 mT. After drying, some samples were covered with a gold layer by means of sputtering or a polymethylmethacrylat (PMMA) layer by means of spin-coating in order to test the detection capability of MFM for embedded magnetic materials. The samples were analyzed by AFM and MFM. The lift height in MFM measurements was set to 20 nm. External in-plane magnetic fields were generated by a pair of solenoids.

6.1.2 Results and discussion

6.1.2.1 Topography

Figure 6.1 shows an overview of the sample. The majority of magnetite nanoparticles are aligned in chains. Most chains exhibit a width of one or two particles. The axes of the chains are nearly parallel to each other and aligned along the applied magnetic field during drying. The chains are much longer than 1 μm (which is typically the length of magnetite-particle chains in intact bacteria). Thus, it can be concluded that the chains are artificially formed by the dipolar interaction. Besides chains, many individual magnetite nanoparticles are scattered on the substrate.

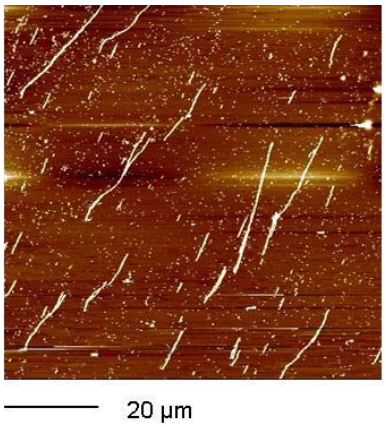

Fig. 6.1 AFM image of biogenic magnetite nanoparticles.

Figure 6.2 (a) is an AFM image of magnetite nanoparticles obtained by a non-magnetic tip. The particles appear rather similar in shape and size. This reflects a strict control of the biomineralization process [Hey03].

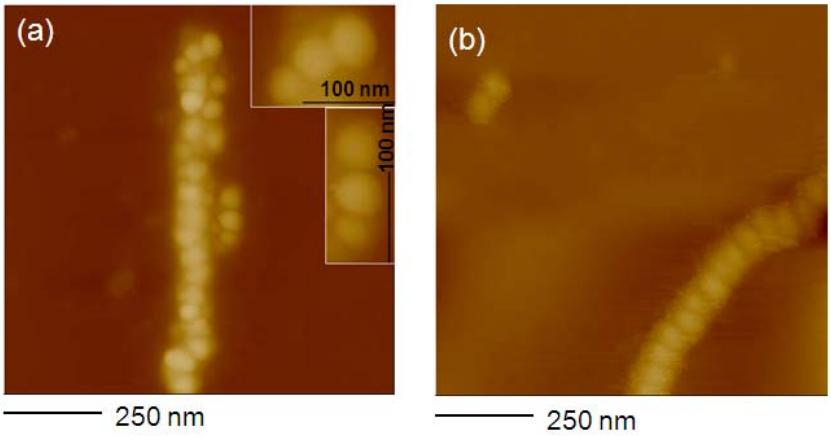

Fig. 6.2 AFM images of biogenic magnetite particles. (a) AFM image in a 2-dimensional view obtained by an AFM tip and (b) AFM image in a 2-dimensional view obtained by a MFM tip.

Though AFM has the advantage to provide three-dimensional information as compared to SEM and TEM, the lateral resolution could be greatly influenced by the curvature radius of the employed probes [Ras02, Ped03]. In Fig. 6.2 (c), the AFM image obtained by a MFM tip (an AFM tip with a magnetic coating in this case) shows a reduced image quality and an increased particle size. This is due to the fact that the additional magnetic coating always increases the curvature radius of the original AFM tip. As illustrated in Fig. 6.3, an AFM tip becomes blunt after depositing a magnetic coating.

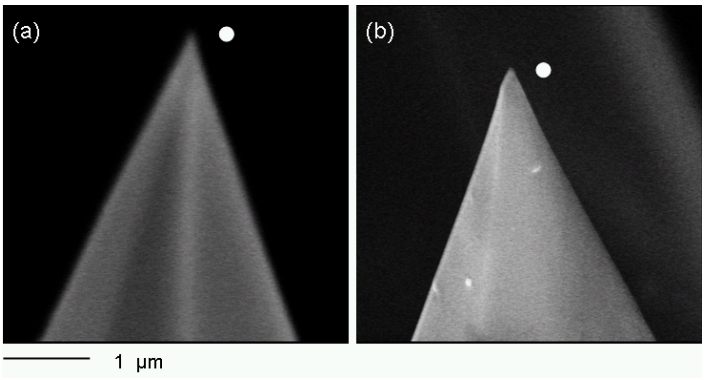

Fig. 6.3 SEM images of (a) an AFM tip and (b) a MFM tip (the same AFM tip with a 30 nm CoCr coating). White circles of 80 nm radius are inserted for reference.

In order to precisely analyze the particle size, both height and lateral diameter distributions of particles are plotted in Fig. 6.4 (a) and (b). All the data are collected from the topographic AFM images obtained by a MFM tip. As the particles are spherical, the height and the lateral diameter of the particles should be equal. In reality, the average height of 100 particles is about 30.5 nm. This is less than half of the average lateral diameter of about 65.8 nm. The deviation between the height and lateral diameters is even larger for the smaller magnetite nanoparticles [Ras02, Ped03].

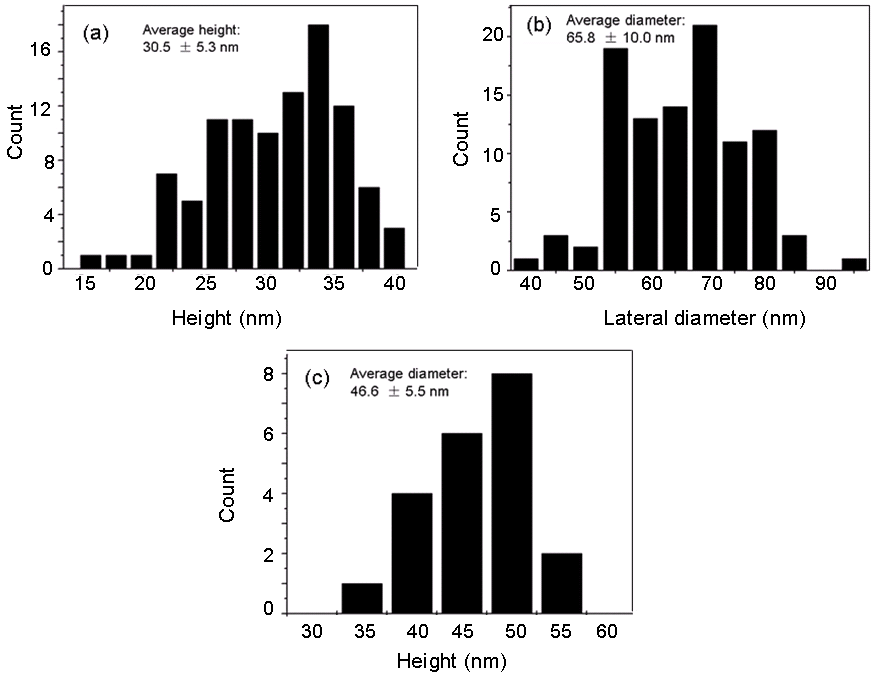

Fig. 6.4 Height and lateral diameter distribution of biogenic magnetite particles. (a) and (b) are distributions of height and lateral diameter according to topographic AFM images obtained by a MFM tip, respectively. (c) The lateral diameter distribution according to topographic AFM images obtained by an AFM tip.

When the curvature radius of the tip is smaller than the particle as sketched in Fig. 6.5 (a), the measured lateral size can be roughly determined from [Ras02, Ped03]

$$R_m = R / \tan(\frac{\pi}{4} - \frac{\theta}{2}), \tag{6.1}$$

with R_m denoting the measured particle radius, R the real particle radius and θ the half cone angle of the tip. As seen from Eq. (6.1), a larger half cone angle leads to a larger measured particle radius.

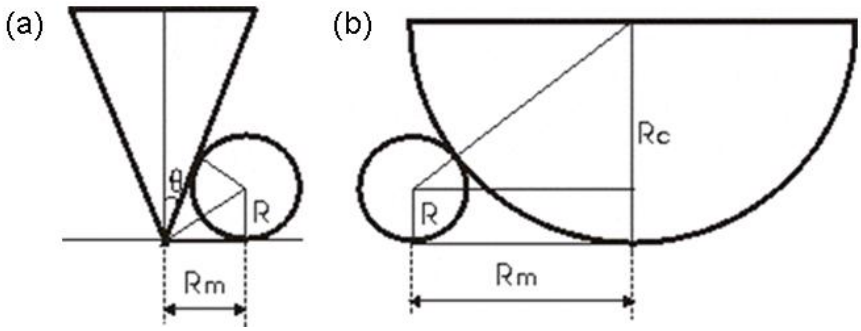

Fig. 6.5 Tip convolution in the case of (a) a relatively large particle radius and (b) a relatively small particle as compared to the curvature radius of the tip.

When the curvature radius of the tip is comparable to or larger than the particle size like in Fig. 6.5 (b), the curvature radius of the tip will influence the measured radius of the particle in the way defined by [Ras02, Ped03]

$$R_m = 2\sqrt{R_c \cdot R}, \tag{6.2}$$

with R_c denoting the curvature radius of the tip.

For the measurements performed with an AFM tip, the distribution of the measured diameters of 21 particles is shown in Fig. 6.4 (c). The average particle diameter is 46.6 nm. The result is consistent with the prediction of Eq. (6.2), which yields a smaller size for particles measured with an AFM tip as compared to a MFM tip. According to the supplier's information, the applied AFM tip has a typical curvature radius less than 10 nm, and the standard cone angle is 30^o. Since the tip curvature radius is smaller than the particles under study, the particle diameter is calculated according to Eq. (6.1), which yields 35.8 nm. This value is close to the average height of the particles. The calculated particle diameter is also in agreement with the analysis by means of SEM. The SEM image is shown in Fig. 6.6. It reveals an average particle diameter between 30 and 40 nm.

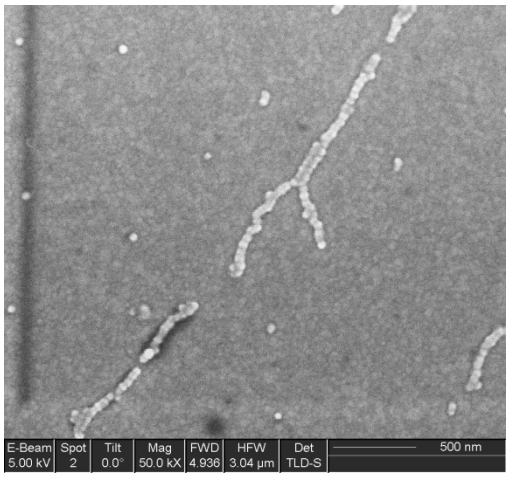

Fig. 6.6 SEM image of biogenic magnetite particles

6.1.2.2 Magnetism

Zero applied field

Figure 6.7 shows AFM and MFM images of magnetite particles in remanence. In the MFM image, magnetic signals stemming from isolated magnetite particles and chains of particles are obvious. All the isolated particles have a dark magnetic contrast, which represents attractive interactions between the magnetic tip and the particles. The resulting attractive force on the cantilever indicates easy alignment of the particle magnetization by the stray field of the magnetic tip. A sketch of the remanent state is shown in Fig. 6.9 (a). The magnetic state of the particles can be estimated by the ratio of magnetic to thermal energy $K_1V/12k_BT$. Here K_1 is the magnetocrystalline anisotropy constant and V the volume of the particles. Taking 1.35×10^4 J/m^3 for $|K_1|$ (bulk magnetite [Dun97]) and an average particle diameter of 35 nm, the energy ratio is 5.4 at room temperature (T = 300 K). This value is slightly above the superparamagnetic range. The particles contain a single stable magnetic domain [But75]. However, the magnetic barrier of the single particles is relatively small and the magnetization of these particles is easily to be aligned by external fields.

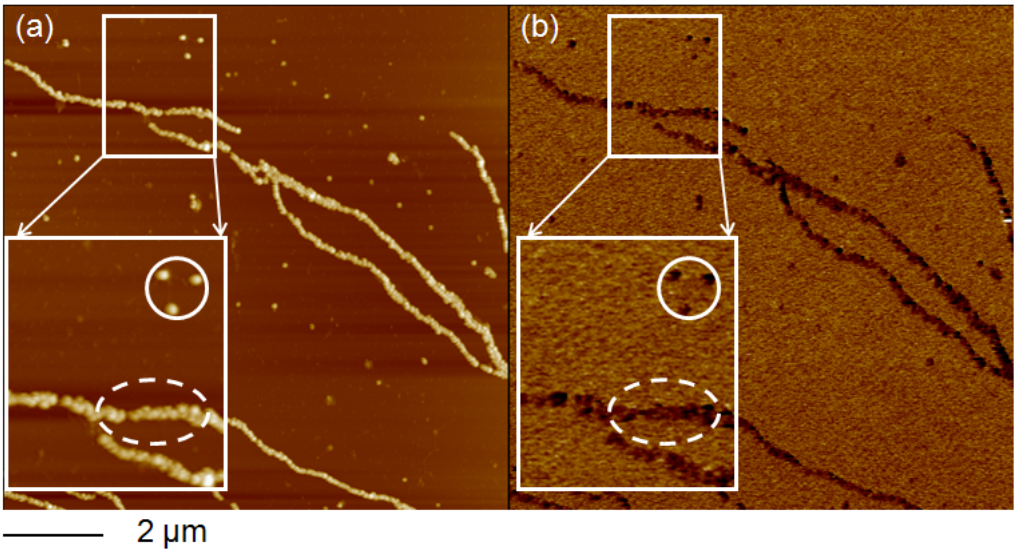

Fig. 6.7 (a) AFM and (b) MFM images of single magnetite nanoparticles and chains of particles in remanence. The isolated particles are marked by solid circles and the particles in chains with reduced magnetic contrast are marked by dashed ellipsoids.

The magnetic contrast of chains of magnetite particles differs slightly from that of isolated particles. Apart from a strong magnetic contrast, also a reduced magnetic contrast is observed.

From the AFM image of Fig. 6.7, the particles in a chain are closely aligned. The dipole-dipole energy $E_{\text{d-d}}$ between two neighboring particles in contact is given by [Sat96]

$$E_{\text{d-d}} = \mu_0[(4\pi/3)R^3M_s]^2/32\pi R^3. \qquad (6.3)$$

With the magnetic permeability of free space of $\mu_0 = 4\pi\times10^{-7}$ H/m, a diameter of the magnetite particles of R = 35 nm and the saturation magnetization of magnetite of M_s = 480 kA/m [Smi59], $E_{\text{d-d}}$ is then calculated to be 2.17×10^{-18} J. From Fig. 6.3 (b), the curvature radius of the MFM tip, R_c, is about 35 nm. For simplicity, a point dipole-dipole interaction between the apex of the tip, considered as a sphere, and the particle is taken into account. The tip-dipole energy $E_{\text{t-d}}$ is given by [Sat96]

$$E_{\text{t-d}} = \mu_0[(4\pi/3)R^3M_s][(4\pi/3)R_c^{\,3}M_t]/32\pi(R+R_c+d)^3, \qquad (6.4)$$

where saturation magnetization of M_t = 720 kA/m [11] for the $Co_{85}Cr_{15}$ alloy thin film tip, and a lift height of d = 20 nm have been assumed. $E_{\text{t-d}}$ is then calculated to be 1.53×10^{-18} J. The magnetic dipolar interaction between neighboring particles is thus strong enough to partly pin the magnetization along the chain axis when the MFM measurement is performed with a lift height of 20 nm. Thus, the attractive interaction between the tip and the particles is reduced

giving rise to a reduced contrast. However, during the topographic scanning, the lift height is zero. In this case, $E_{t\text{-}d}$ is increased according to Eq. (6.4) to 3.25×10^{-18} J, which exceeds $E_{d\text{-}d}$. The particle magnetization will then partly along the tip stray field. As a consequence, the pinning effect of the neighboring magnetite nanoparticles is reduced. However, there is no indication in the MFM images for a remanent distortion of the sample magnetization due to topographic imaging with the ferromagnetic probe.

The magnetic data in remanence are different from previous MFM observations [Alb05, Ebe05]. The latter have shown magnetic images in terms of rings around white centers. In the respective experiments, magnetite nanoparticles were subjected to a vertical external field prior to the measurements and supposed to have a stable magnetization oriented perpendicular to the substrate surface during imaging.

Applied magnetic fields

A magnetic field of 60 mT is applied in the sample plane. This is strong enough to fully align the magnetization of magnetite nanoparticles in the field direction [Her05]. MFM images are shown in Fig. 6.8. Magnetic dipoles of isolated particles and particles in chains are appearing as combined dark and bright regions, respectively. The magnetic contrast is reversed when the external field is reversed.

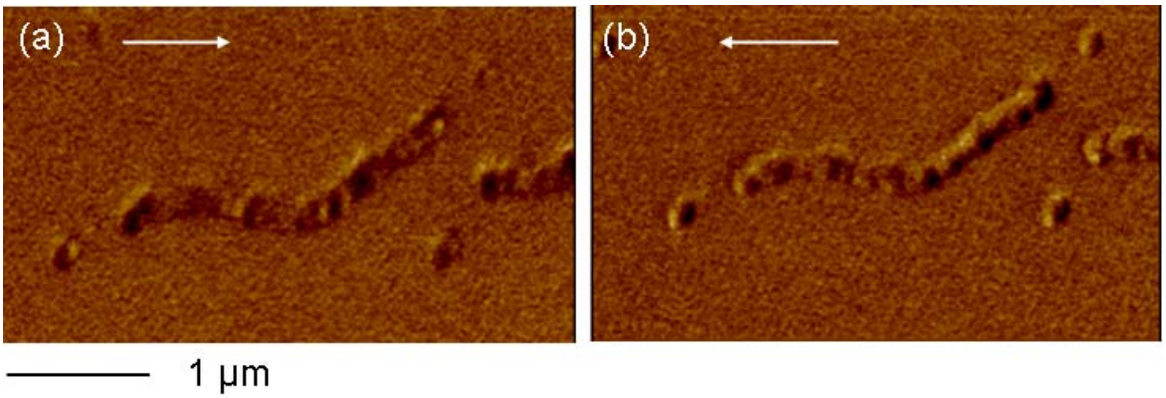

Fig. 6.8 MFM images of biogenic magnetite particles in a 60 mT in-plane field. Magnetic field direction: (a) from left to right (b) from right to left. The field direction is indicated by arrows.

The models sketched in Fig. 6.9 (b) and (c) illustrate the interactions between a MFM tip and magnetic particles in an external magnetic field. The positive and negative magnetic poles produce stray fields of opposite directions at both poles. The result is that the tip is attracted at one pole and repelled it at the other one.

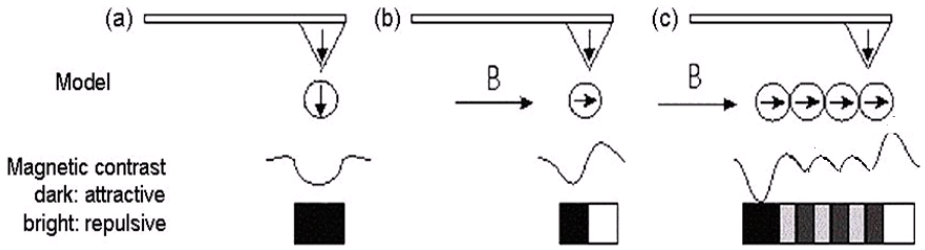

Fig. 6.9 Schematics of the interaction between a MFM tip and magnetic particles. (a) remanent state, (b) and (c) in external magnetic fields for isolated magnetic particles and a chain of particles, respectively.

The magnetization reversal process of a two-particle chain is shown in Fig. 6.10. From the AFM image in the upper-left part of Fig. 6.10, the angle between the field axis and the chain axis is roughly 45°. In absence of external magnetic fields, the MFM image shows a weak magnetic dipole structure along the chain axis. The magnetic structure of the chain remains unchanged up to a magnetic field of 13 mT. Upon increasing the magnetic field up to 26 mT, the magnetic dipole axis rotates from the chain axis toward the axis of the external magnetic field. Upon further increasing the external magnetic field, the magnetic contrast is further enhanced. If the external magnetic field is beyond 60 mT, the magnetic contrast stays almost unchanged, which indicates a saturated state of the chain.

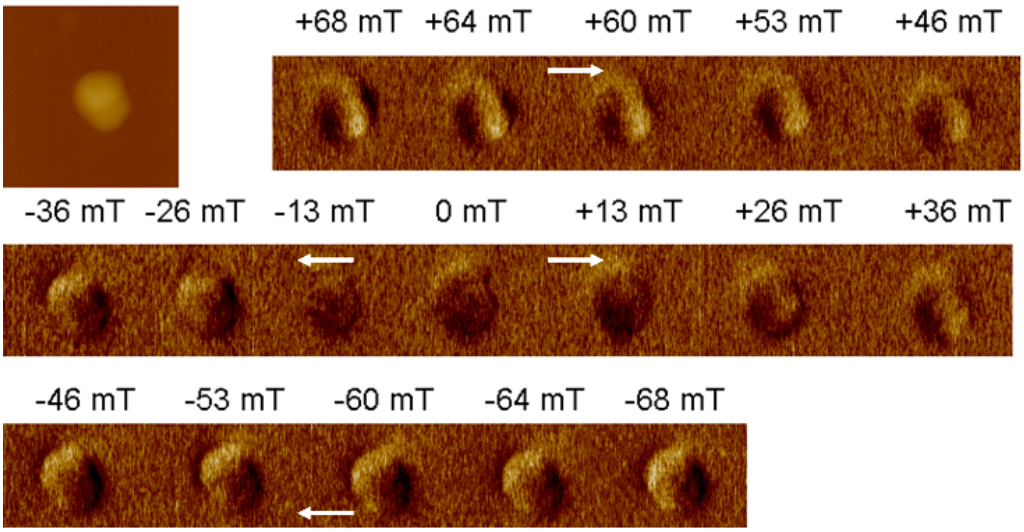

Fig. 6.10 AFM (upper-left corner) and MFM images of a chain of two biogenic magnetite particles in external in-plane magnetic fields. The field direction is indicated by arrows.

The change in the magnetic contrast as a function of the applied magnetic field is analyzed by subtracting consecutive MFM images obtained at various field strengths [Wit99]. In this study, a commercial software (Software for DI multimode nanoscope) is used to quantify the magnetic contrast of MFM images by avoiding direct MFM image subtraction. The depth

analysis function enables phase signals of a specified area to be accumulated in a histogram. With this capability, the magnetic contrast is quantified by the difference in the averaged phase shift for the dark and bright regions in each MFM image, i.e., the difference between the depth levels of 25% and 75%. The results are plotted in Fig 6.11. We find that the change in the magnetic contrast is not a linear function of the field. The maximum change occurs at a field of about 26 mT. A coarse estimation shows that the field at which the maximum change occurs is comparable to that particular field (31 mT for magnetite nanoparticles of 35 nm diameter), which is exerted on one magnetite nanoparticles by its neighbor.

Magnetic hysteresis loops of bacteria have been measured by a cantilever magnetometer [Mar98] under high vacuum condition ($p < 10^{-6}$ mbar) at room temperature. As shown in Fig. 4.14 in section 4.3, the coercivity and the saturation magnetic field are determined to be about 25 mT and 50 mT, respectively. These values are in agreement with the magnetization reversal process of a two-particle chain as discussed above. This result indicates that magnetic dipolar interaction experienced by each particle is largely independent of the chain length. The latter is proven by the fact that the chain length of bacteria is much longer than that of a two-particle chain.

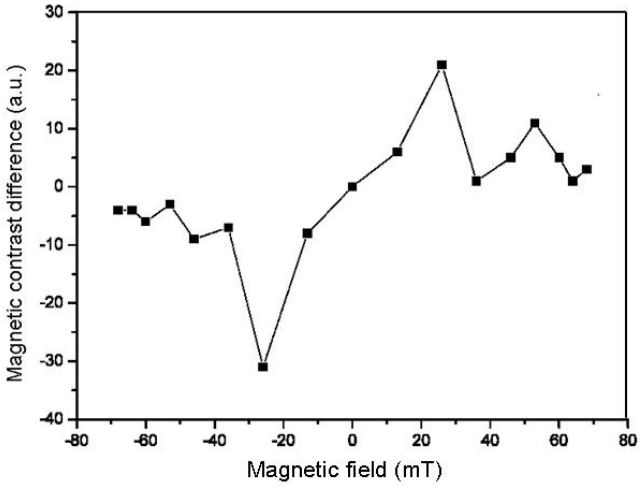

Fig. 6.11 Magnetic contrast of magnetite nanoparticles versus the external magnetic field.

MFM detection of embedded magnetite nanoparticles

As shown in Fig. 6.12, the magnetic contrast of biogenic magnetite nanoparticles underneath a 20 nm gold layer is still observable in an external magnetic field of 68 mT. The magnetic

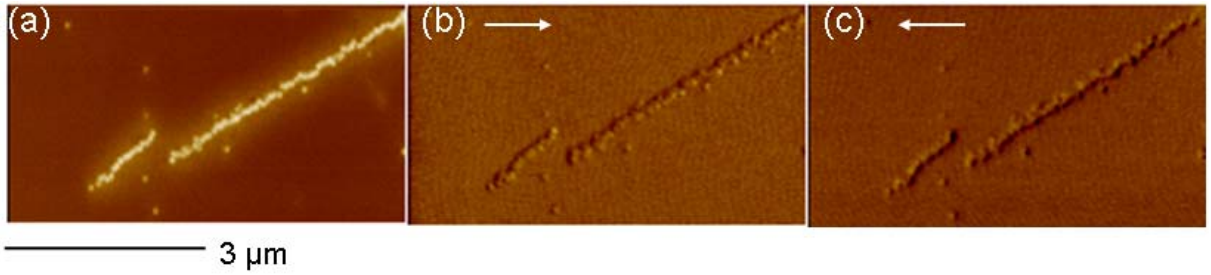

Fig. 6.12 (a) AFM image, (b) and (c) MFM images of biogenic magnetite particles under a 20 nm-thick gold layer in an in-plane magnetic field of + 68 mT and -68 mT, respectively. The field direction is indicated by arrows.

nature of the signals is confirmed by the reversal of magnetic contrast upon reversing the magnetic field direction. When an additional 30 nm gold layer was sputtered onto the same sample, the chain could be still recognized by its height contrast as shown in Fig. 6.13 (a). In contrast, the MFM images in Fig. 6.13 (b) and (c) represent the surface topography without clear magnetic signals. Therefore, the magnetite nanoparticles 50 nm below the gold layer surface are not detectable by MFM.

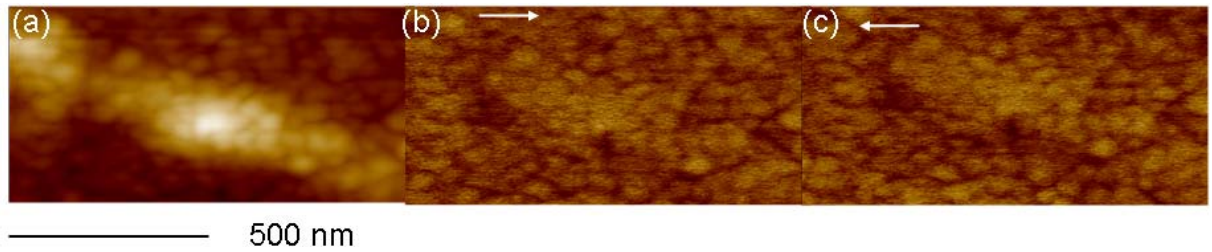

Fig. 6.13 (a) AFM image, (b) and (c) MFM images of biogenic magnetite particles under a 50 nm-thick gold layer in an in-plane magnetic field of + 68 mT and -68 mT, respectively. The field direction is indicated by arrows.

A PMMA layer of 50 nm provides a relatively smooth surface. As shown in Fig. 6.14 (a), the topography of magnetic nanoparticles is smeared by the PMMA layer, but the locations of the nanoparticles are still visible. The existence of magnetite nanoparticles can be confirmed by MFM in this case. The magnetic contrast can also be confirmed by reversing the external magnetic field.

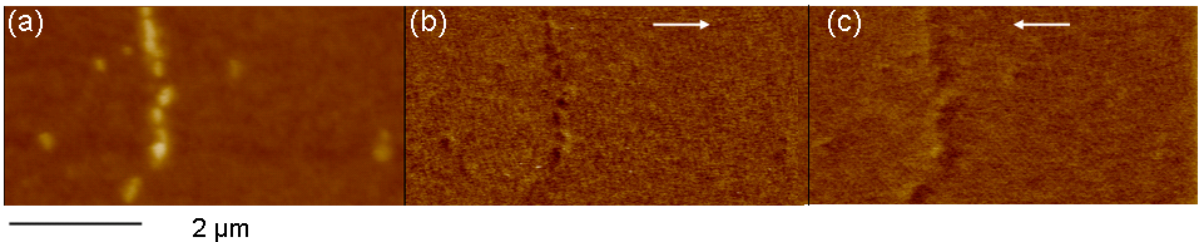

Fig. 6.14 (a) AFM image, (b) and (c) MFM images of biogenic magnetite particles under a 50 nm-thick PMMA layer in an in-plane magnetic field of + 68 mT and -68 mT, respectively. The field direction is indicated by arrows.

Thus, the surface topography has a significant influence on the detection capability of MFM for embedded magnetic materials. The detection capability is greatly reduced for magnetic particles underneath a rough surface.

6.1.3 Conclusion

According to the AFM results, magnetite nanoparticles produced from *M. gryphiswaldense* have a narrow size and shape distribution. Though AFM has the advantage to provide three-dimensional information, the lateral resolution is greatly influenced by the curvature of the AFM tips. Based on tip deconvolution models, the average particle size can be reliably determined. The results are in agreement with the SEM observation. According to MFM measurements, magnetite nanoparticles have a single and pinned magnetic domain. In remanence, individual particles are easily polarized by the MFM tip, while particles aligned in chains are less influenced by the MFM tip. This is due to dipolar interactions among particles. In external magnetic fields, the dipolar magnetization of magnetite nanoparticles is clearly observable by MFM. The dipole moment is switched when the external magnetic field is reversed. The magnetization reversal process of a two-particle chain has been recorded by MFM in a field range of ±68 mT. The change in the magnetic contrast of magnetite nanoparticles upon changing the external magnetic field was estimated in a quantitative way. The maximum change occurs at 26 mT. This field magnitude is comparable to the dipolar field exerted on individual magnetite nanoparticles by their chain neighbors. The chain is saturated at 60 mT, which is in agreement with the result obtained by a cantilever magnetometer. The capability of MFM to explore magnetite particles underneath a surface is demonstrated by the comparative experiments. The capability is quite dependent on the sample topography.

6.2 Magnetite clusters from the sensory system of salmon

Magnetite nanoparticles are present in a variety of biological species and fulfil physiological functions which are only in part understood after long years' study [Kir01]. In particular, they possibly play a role in the magnetoreception of many animals [Man88, Kir01, Die00, Mor04]. The size and the arrangement of magnetite nanoparticles are crucial to their function. Particles discovered in vertebrates are usually superparamagnetic or ferromagnetic with sizes ranging from several nm to a little less than 100 nm [Kir85], and they are typically single domain. The orientation of the magnetic moments of superparamagnetic particles tends to be randomized by thermal activation, while in case of ferromagnetic particles the magnetic moments remain stable. In several magnetoreceptor models, clusters of superparamagnetic particles are assumed to be arranged in the elastic matrix or in vesicles [Shc99, Win01, Man88]. In the elastic matrix magnetic forces lead to deformation, while in the vesicle magnetic torque results in mechanical torque [Kir81, Win01]. In addition, some part of the magnetic material might act as a flux concentrator [Fle07a, Fle07b]. The actual intracellular arrangement of the magnetite particles in tissue is, however, difficult to determine. In recent work, magnetite in form of particle clusters had been extracted from the sensory system of Atlantic salmon [Pet09]. The clusters are possible functional elements within the fish's sensory cells. The mechanisms of magnetoreception proposed so far are either based on isolated ferromagnetic particles, on particles in chains [Kir81, Kir01] or on clusters of superparamagnetic particles [Shc99, Win01]. In this section, the plausibility of clusters of ferromagnetic particles being the basis of magnetoreception and the applicability of existing magnetoreception models are discussed.

6.2.1 Sample preparation and experiment

Magnetite particles were extracted from the sensory system of Atlantic salmon. Tissue was dissolved in a lysis buffer containing 5 ml of 400 mM Tris HCl (hydroxymethyl aminomethane hydrochloride, pH 8.5), 0.5 ml of 0.5 M EDTA (ethylene diamine tetraacetic acid), 1 ml of 10% SDS (sodium dodecyl sulfate), 2 ml of 5 M NaCl, 0.25 ml of 20 mg/ml proteinase K and 41.25 ml of H_2O per 50 ml solution. The dissolving process continued over night at 60 °C in an oven. The solution was then centrifuged at 1.7×10^4 rpm. The pellets were resuspended in 10 M NaOH and left over night at 60 °C. Afterwards, the solution was centrifuged at 1.2×10^4 rpm. The pellets were resuspended in H_2O and magnetite particles were magnetically collected.

The magnetite particles were deposited on a mica surface. A conductive coating of 5 nm gold was sputtered onto the whole sample to avoid possible electrostatic charging. AFM and MFM measurements were performed in air. Sample and scanner were placed inside a vertical coil to produce well-defined external fields.

6.2.2 Results and discussion

Size of particles and clusters

AFM images of the extracted magnetite material on various sample locations are shown in Figs. 6.15 (a) and (b). The extracted magnetite material appears in form of clusters of uniform size and shape over the entire sample. The clusters are spherical with diameters of 200-300 nm. Figure 6.15 (c) is the profile of a cluster, which is marked by a white bar in Fig. 6.15 (b). From higher resolution images of Fig. 6.15 (d) and (e), single magnetite particles can be identified to compose the clusters. The diameter of the individual particles is approximately 30-60 nm. In another experiment, an average particle diameter of 30-35 nm had been determined [Pet09, Man09]. Such particles are known to be ferromagnetic at room temperature [Wor98]. The particles within a cluster are arranged in a compact way and the number of particles is estimated to be roughly 100-200.

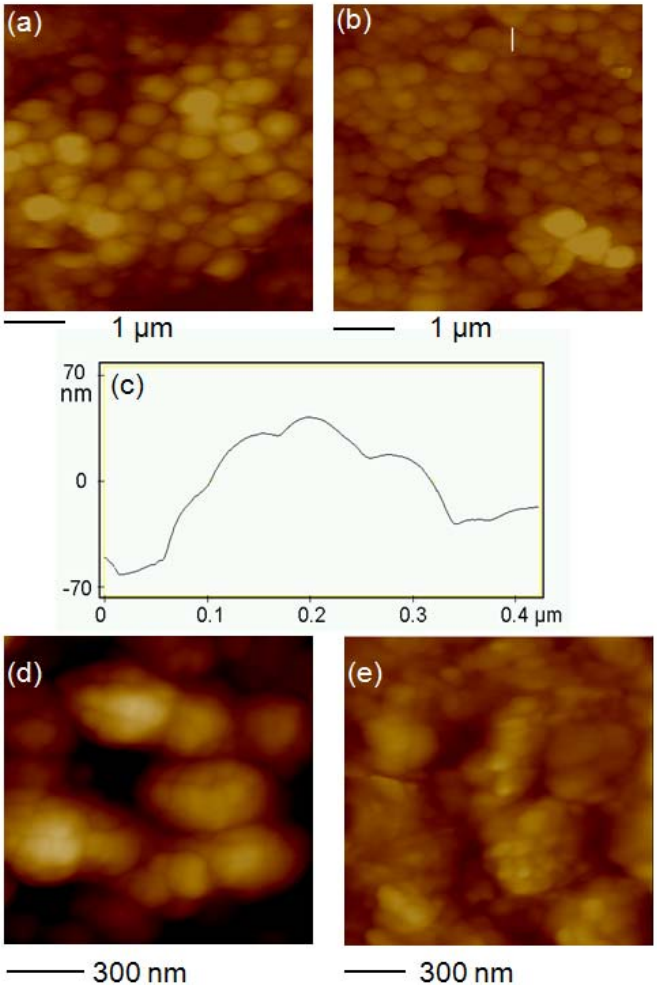

Fig. 6.15 AFM images of magnetite clusters from salmon. (a), (b), (d) and (e) are images on various sample locations. (c) is the profile of a cluster marked in (b) by a white line.

Magnetic properties

Figure 6.16 shows the MFM image that belongs to the AFM image in Fig. 6.15 (b). The MFM measurement was performed in remanence. In the MFM image, a dark contrast is clearly observed all over the measured region, indicating an attractive interaction between the magnetic tip and the magnetite clusters.

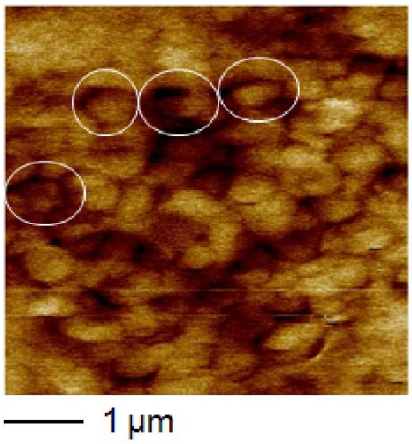

Fig. 6.16 MFM image of the magnetite clusters. Phase signals of the MFM cantilever were measured at constant oscillation amplitude in the lift mode. The circles demonstrate the enhanced magnetic contrast at clusters edges.

Upon a closer inspection of Fig. 6.16, the magnetic contrast at the edges of the clusters tends to be enhanced. Examples of this "edge effect" are highlighted by circles. A similar phenomenon had been observed before in colloidal iron clusters and was explained by a flux-closed state of the magnetic particle clusters [Ped03].

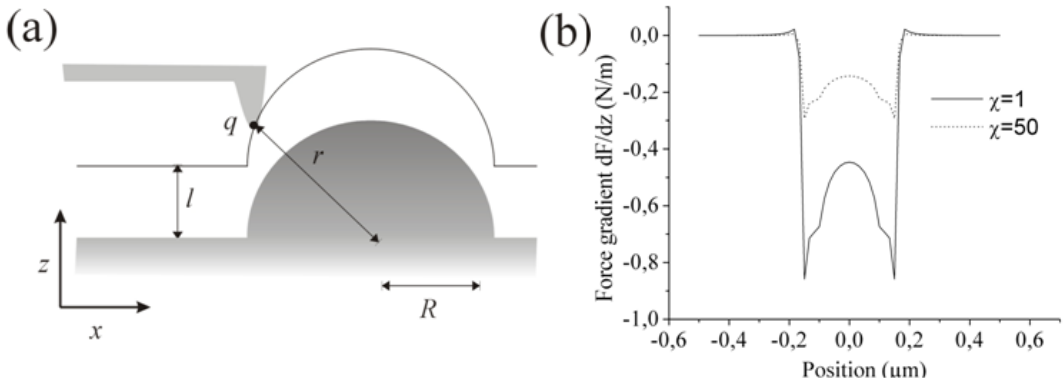

Fig. 6.17 (a) Schematics of the trajectory of the MFM probe. (b) simulated force gradient along the trajectory for a cluster of 400 nm diameter and for two different values of the susceptibility.

A model of the tip-cluster interaction is sketched in Fig. 6.17 (a). A cluster is regarded as a sphere of magnetic susceptibility χ and radius R. The MFM tip is modelled in the monopole approximation [Loh99, Gar01] using a magnetic tip charge of q. The topography of a cluster within an ensemble is given by

$$z_0(x) = \sqrt{R^2 - x^2}\,, \tag{6.3}$$

for $-R \leq x \leq R$, where x is measured from the center of the cluster. The MFM tip positions are $z(x) = z_0(x) + l$, with l being the lift height. For a given lateral position x, the distance to the cluster center is given by

$$r(x) = \sqrt{x^2 + z(x)^2} \,. \tag{6.4}$$

The magnetic field acting on the cluster due to the presence of q at a distance of r is calculated according to Ref. [Nor95]. The resulting magnetic field is given by **H** = H **n**, with **n** being the unit vector pointing from tip to cluster center. For the limiting case of infinite χ one obtains

$$H = -\frac{q_i}{4\pi\left(r - r_q\right)^2} + \frac{q_i}{4\pi r^2}, \tag{6.5}$$

with $q_i = qR/r$, and $r_q = R^2/r$. For a finite susceptibility one obtains

$$H = -\frac{q_i}{4\pi\left(r - r_q\right)^2} + \int_0^{r_q} \frac{\sigma(r')}{\left(r - r'\right)^2} dr', \tag{6.6}$$

with $\sigma(r') = (q/R)[\gamma(1-\gamma)/2](r_q r'/R^2)^{-(1+\gamma)/2}$, $\gamma = 2\chi/(2+\chi)$ and r_q as defined above. The effective force on the tip is then given by

$$F(x) = qH_z(r(x)), \tag{6.7}$$

where H_z denotes the z-component of the field. The modelled MFM signal is shown in Fig. 6.17 (b). The magnetic contrast is clearly enhanced at the edge as observed in the experiments (Fig. 6.16). This supports the assumption that the magnetite particle cluster essentially behaves as a sphere of constant permeability.

A sequence of AFM and MFM images obtained in external magnetic fields is presented in Figs. 6.18 (a)-(h). The external field strengths are 0.5 mT, 3.5 mT, 7 mT and 15 mT respectively. The external magnetic field was applied normal to the sample surface. As the tip moment was found to be very stable upon imaging a test sample in external magnetic fields, the variation in the magnetic contrast is attributed to the change in the magnetic structure of the clusters. The magnetic contrast is enhanced rapidly upon increasing the external magnetic field. It shows a completely dark appearance already at small field strengths for those relatively isolated and large clusters, which are highlighted in both the AFM and MFM images. The result suggests that large clusters are more susceptible to the external magnetic field at their edges than small clusters surrounded by others.

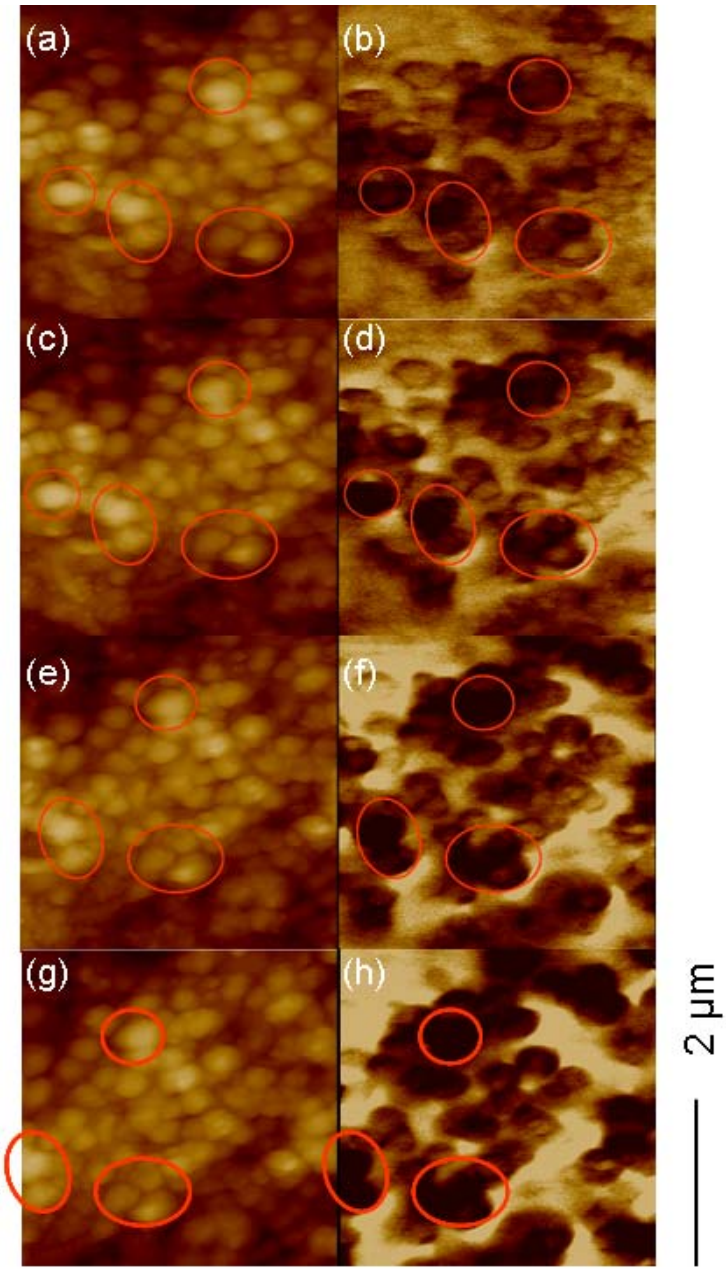

Fig. 6.18 Sequence of AFM and MFM images in various magnetic fields normal to the sample surface. (a), (c), (e) and (g) are AFM images, and (b), (d), (f) and (h) are the corresponding MFM images obtained at field values of 0.5 mT, 3.5 mT, 7mT and 15 mT, respectively. The circles highlight the locations where the magnetic contrast rapidly changes in response to the external magnetic field.

When the applied external magnetic field is above 35 mT, magnetic contrast becomes completely dark for all the clusters as shown in Fig. 6.19. This indicates that magnetic clusters are approaching a saturation state below this field. The shift in the AFM images in Fig. 6.19 is due to the thermal drift.

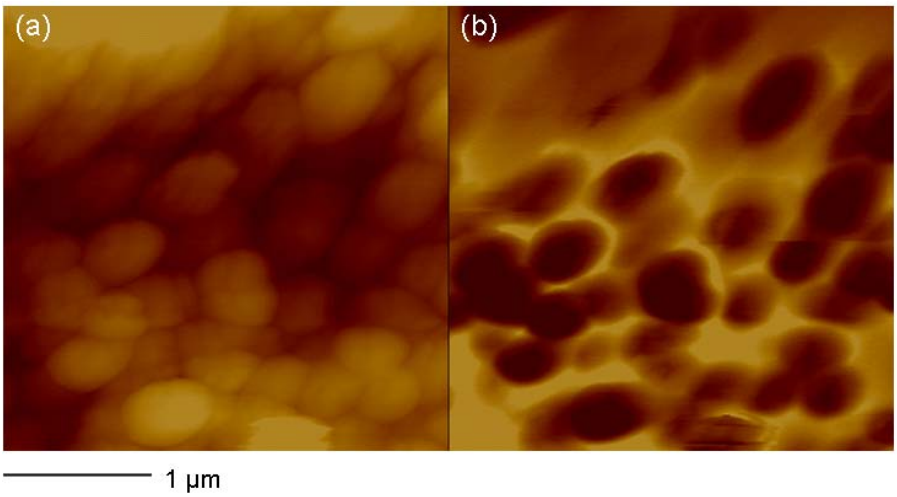

Fig. 6.19 (a) AFM and (b) MFM images of magnetic cluster in a 35 mT external magnetic field.

In order to gain insight into the magnetic behavior of the magnetite particle clusters in external magnetic fields, modelling was performed by means of a Monte Carlo approach by M. Gruner from the University of Duisburg. The individual nanoparticles within a cluster were treated as freely rotating magnetic dipole moments. Since the anisotropy field of magnetite being an order of magnitude smaller than the dipole field of neighboring particles, the anisotropy of individual particles was neglected. The long-range dipolar interaction between the individual dipole moments was fully taken into account. The total magnetic moment of a cluster was set to $10^6 \mu_B$, corresponding to 123 individual magnetite particles of 34 nm diameter. The individual particles were arranged in a close packed (fcc) fashion with a center-to-center distance of 80 nm. The resulting clusters are of ellipsoidal shape, and the x, y and z axes have a length of 340 nm, 450 nm and 570 nm, respectively. Initially, low energy magnetization structures were obtained within a simulated annealing approach by exponentially cooling down the system from 3000 K to 100 K within 1.5×10^6 Monte Carlo sweeps (MCS), touching each magnetic moment. Starting from these configurations, the simulations with an external magnetic field were performed at 300 K with a number of 1.5×10^5 MCS for each value of the external magnetic field (the first 5×10^4 MCS were discarded to allow the system to reach thermal equilibrium).

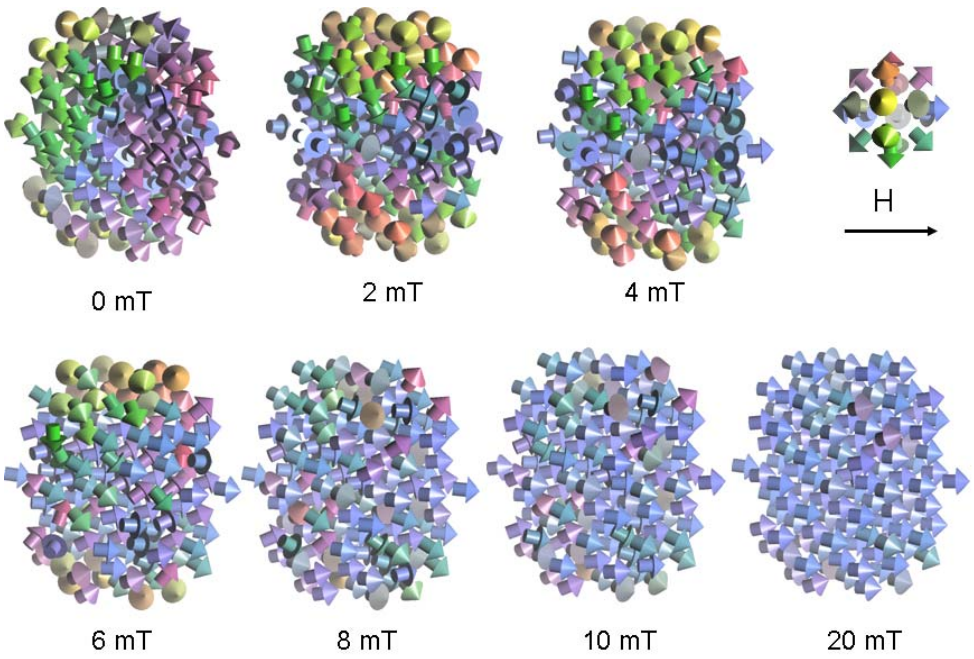

Fig. 6.20 Simulation of the magnetic structure of a magnetite cluster in a variable magnetic field. The colors refer to the direction of the magnetic dipolar moments as shown in the upper right corner of the figure.

Magnetic structures of the clusters are shown in Fig. 6.20. As is well known, the magnetic structure in remanence is a vortex state with a total net magnetization close to zero [Hub98]. In a magnetic field, this vortex state transforms into a nearly saturated state at 10 mT by coherent rotation. The coherent rotation leads to the nearly linear, hysteresis-free magnetization curve of Fig. 6.21. The resulting magnetization curve deviates from the corresponding Langevin function, indicating strong magnetic interaction between particles. The magnetization curve is rather similar to that of densely packed superparamagnetic particles under physiological conditions [Waj04]. Therefore, according to both the MFM and modelling results, clusters can be regarded as permeable entities. Sensory models treating the observed clusters of superparamagnetic particles as permeable spheres [Shc99, Win01] should thus also be applicable to salmon.

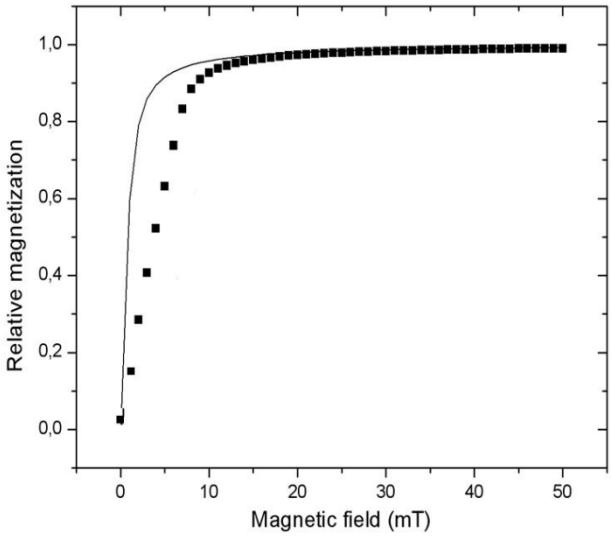

Fig. 6.21 Magnetization curve of a magnetite cluster from modelling. The cluster has a total magnetic moment of 10^6 μ_B, composed of 123 fcc close-packed particles of 34 nm diameter. The black line indicates the Langevin function for the employed particles at 300 K.

6.2.3 Conclusion

According to the AFM and MFM results, magnetite particles extracted from sensory cells of salmon are ferromagnetic and arranged in densely packed clusters. These clusters are uniform in size and shape. The MFM contrast is enhanced at the cluster edges, and saturates within a field range of 10 to 35mT. According to the results of modelling, the remanent state of the clusters is a vortex with negligible net magnetization. In a magnetic field, this vortex state transforms into the near-saturated state by coherent rotation. At a lower field, the clusters can be regarded as spheres of constant permeability. The sensory mechanisms based on the assumption of an ensemble of superparamagnetic particles are thus valid for the investigated salmon samples.

6.3 Detection of magnetic material in fish tissues

Magnetoreceptors in animals are often supposed to be constituted by magnetite particles [Kir81, Shc99, Kir01, Win01]. However, it proves difficult to understand the mechanism of magnetoreception, as the actual arrangement of magnetic particles in biological issues is still poorly known. Thus, technical approaches to locally detect magnetic particles in tissues are crucial to ultimately disclose the mechanism.

In this section, Mozambique tilapia fishes (migratory) and Zebra fishes (non-migratory) are studied. Both fishes have demonstrated magnetosensing in behavioral experiments after

training [Shc05]. Rock magnetic tests and MFM measurements are carried out to globally and locally explore magnetic particles in fish tissues, respectively. Measurements were performed in the department of earth and environmental sciences, Munich University, with the help of Mr. A. Davila.

6.3.1 Detection of magnetic particles in fish *in situ* by rock magnetic tests

6.3.1.1 Sample preparation and experiment

Heads of Tilapias and Zebra fish were separated from the rest part of the fish by a glass knife. Possible magnetic contaminations on the sample surface were removed before experiments by washing the sample in a diluted solution of HCl. Afterwards, 2 heads of Tilapias fishes, 2 bodies of Tilapias fishes, 11 heads of Zebra fishes and 11 bodies of Zebra fishes. The capability were measured separately.

The isothermal remanent magnetization (IRM) acquisition and the alternating magnetic field (AF) demagnetization were measured by a SQUID magnetometer (2G Enterprises). The IRM is the remanent magnetization of one sample after a short exposure to a static magnetic field. To obtain an IRM acquisition curve, a pulsed magnetic field was stepwisely increased to the maximum value of 1 T for all the samples. After the sample has reached the saturation IRM, an alternating magnetic field was applied to demagnetize the sample at a step width of 5 mT till the maximum alternating field of 100 mT. The magnetic moment of the samples was plotted as a function of the strength of the alternating magnetic field to obtain AF demagnetization curves. Seven hours later, the fish samples were measured again following the same procedures.

As the magnetization of the samples was small, other possible magnetic contributions to the results were carefully handled. Quartz wool, which was used to fix the samples, was only placed in the sample holder after each magnetizing process. The magnetization of the quartz wool is then kept constant during the measurements. The magnetic contribution of the sample holder was recorded separately for each measurement and then subtracted.

6.3.1.2 Results

Tilapias fishes

Figure 6.22 (a) shows the IRM acquisition curves of two Tilapias heads and the empty holder. The magnetic signal of the Tilapias sample is about two times larger than that of the sample holder. Both the fish heads and the sample holder are saturated at a field of less than 200 mT. The saturation IRM of the Tilapias sample and the sample holder are 0.08 mA/m and 0.043 mA/m, respectively. The IRM acquisition curve of the Tilapias sample has two distinct features as compared to that of the sample holder: (1) a slight decrease of magnetization at the beginning of the magnetizing process and (2) a steep increase of magnetization afterwards.

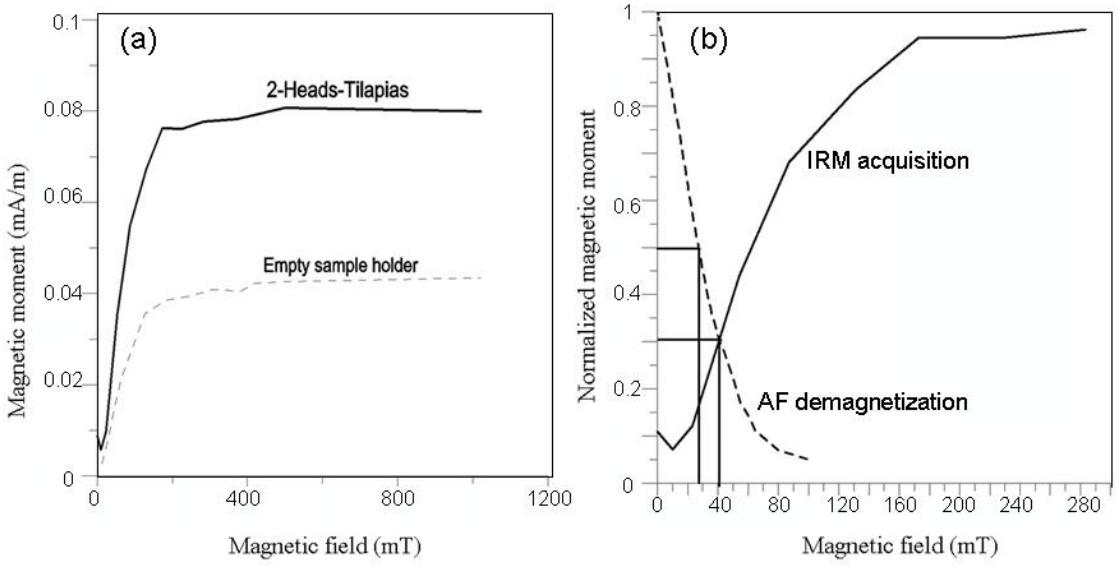

Fig. 6.22 IRM acquisition curves of (a) Tilapias sample and the empty sample holder, and (b) the IRM acquisition and the AF demagnetization curves of the Tilapias sample.

Figure 6.22 (b) shows the curves of the IRM acquisition and AF demagnetization of the Tilapias sample (normalized to the saturation IRM). Important parameters, like the median destructive field, the intersection of IRM acquisition and AF demagnetization (*R*-value), and the median coercivity, are determined from Fig. 6.22 (b) and listed in Tab. 6.1. The median destructive field is the alternating magnetic field at which the remanent magnetization is reduced to half of the saturation IRM. The median coercivity is the field defined by the intersection of the IRM acquisition and AF demagnetization curves. *R* value is the ratio of the remanent magnetization to the saturation IRM at the intersection of the IRM acquisition and AF demagnetization curves.

Tab. 6.1 Analysis of the IRM acquisition and AF demagnetization curves of fish samples.

	median destructive field (mT)	*R*-value	median coercivity (mT)
2 heads of Tilapias fish	26	0.3	40
2 bodies of Tilapias fish	25	0.2	40
11 heads of Zebra fish	20	0.18	36
11 bodies of Zebra fish	25	0.25	40

The results of the repeated experiments 7 hours later show no apparent difference from the first ones.

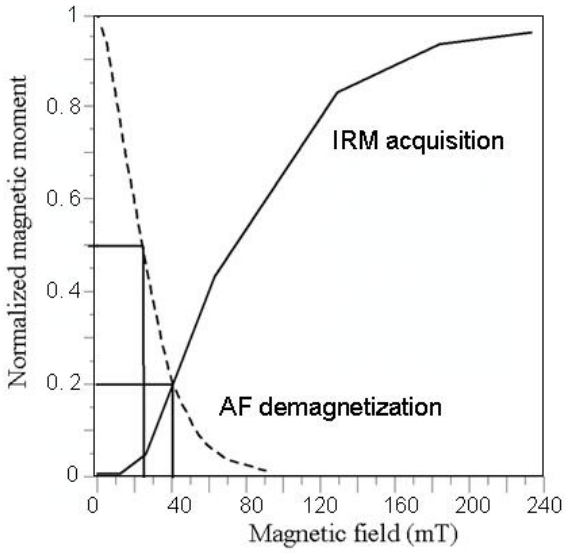

Fig. 6.23 IRM acquisition and AF demagnetization curves of the sample from Tilapias bodies.

Figure 6.23 shows the IRM acquisition and AF demagnetization curves of a sample from the Tilapias bodies (normalized to the saturation IRM). The determined parameters are listed in Tab. 6.1.

Zebra fishes

Figure 6.24 (a) shows the IRM acquisition curves of the Zebra head sample and the empty holder. The signal of the sample is three times larger than that of the sample holder. The saturation IRM of the sample and of the empty holder are 0.037 mA/m and 0.013 mA/m, respectively. The IRM acquisition curve of the head sample has a steeper increase of magnetization than that of the empty holder. A noticeably high saturation field over 400 mT is observed. Figure 6.24 (b) shows the curves of IRM acquisition and AF demagnetization of the same sample (normalized to the saturation IRM). The determined parameters are listed in Tab. 6.1.

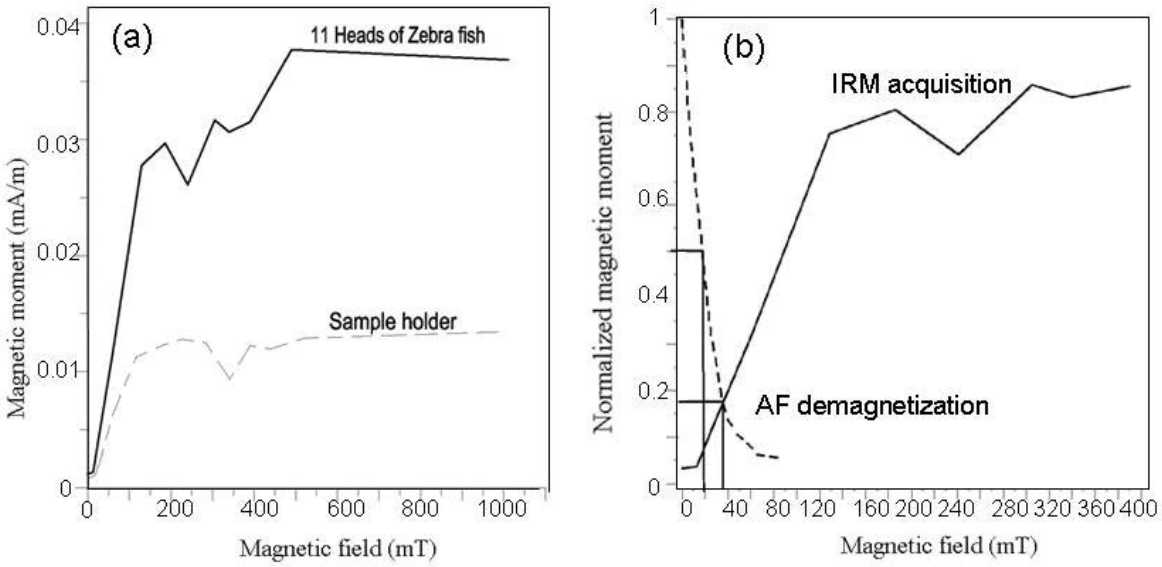

Fig. 6.24 IRM acquisition curves of (a) a sample of heads from Zebra fishes and the empty sample holder; and (b) IRM acquisition and AF demagnetization curves of the head sample.

No apparent difference in the curves of IRM acquisition and the AF demagnetization is observed for the sample measured 7 hours later.

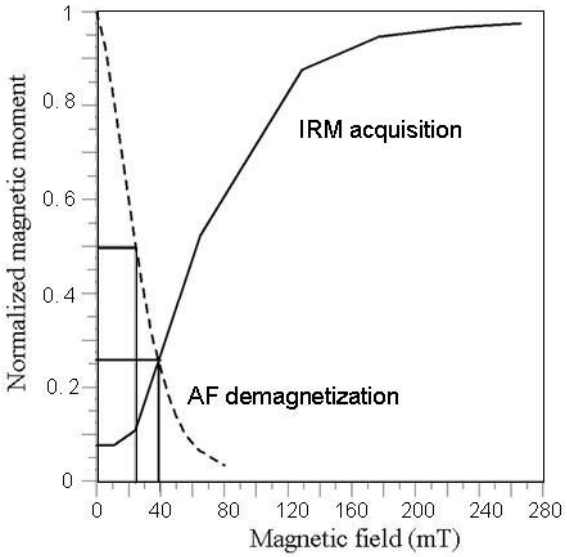

Fig. 6.25 IRM acquisition and AF demagnetization curves of a sample from 11 bodies of Zebra fishes.

Figure 6.25 shows the IRM acquisition and AF demagnetization curves of the sample from 11 bodies of Zebra fishes (normalized to the saturation IRM of 0.6311 mA/m). The determined parameters are listed in Tab. 6.1.

6.3.1.3 Discussion

Remanent magnetization is obviously found in all samples. The results suggest the presence of magnetic material in both Tilapias and Zebra fishes. Magnetization decreases at the beginning of the IRM curve of two Tilapias heads also implies the existence of the magnetic material. This phenomenon is often due to the breakage of originally aligned magnetic moments by relatively weak pulse fields [Mos93].

The *R*-values of samples of Tilapias and Zebra fishes are significantly less than 0.5, which suggests the presence of interacting magnetic particles. For a system of non-interacting particles, the *R*-value should be 0.5 [Cis81, Mos93]. Magnetic moments that are aligned by a given pulse field level should also be moved by an alternating field of the same strength. Interactions between the particles support AF demagnetization and inhibit IRM acquisition, displacing the intersection point of these two curves to a position below half of the saturation IRM [Cis81].

The *R*-value and the median coercivity of Tilapias heads are similar to those of heads of migratory yellowfin tuna [Wal84] and chinook salmon (Oncorhynchus Ghawytscha) [Kir85b]. It implies that the potential magnetoreceptor of Tilapias fishes is also located in the head region and consisits of similar magnetic materials.

The field to obtain the saturation IRM for the Tilapias heads is less than 200 mT. The result rules out the presence of hematite and metallic iron alloys. Hematite and metallic iron alloys will continue to acquire remanent magnetization in fields above 1000 mT [Kir83]. Most probably, magnetite is the magnetic material in the Tilapias heads, as it reaches the saturation IRM at magnetic fields of only few hundred mT. In case of the Zebra fish heads, a magnetic field higher than 400 mT is required to obtain the saturation IRM, though a large fraction of the saturation IRM has been acquired at a field of about 200 mT. The result is in agreement with the noticeably lower *R*-value and median destructive field of the zebra head sample than those of the Tilapias heads. Besides magnetite, other magnetic materials could co-exist in Zebra fish heads.

The tissues from pigeons' heads show a change in the magnetic property after several hours (i.e., no remanent magnetization was measured in fresh tissues, whereas remanent magnetization is acquired after the tissues dried out) [Pre80, Han00]. Very fine superparamagnetic particles discovered in pigeons' heads are supposed to gain stable

magnetization by aggregation due to shrinkage of cell membrane and cytoplasm. In the present case, the magnetic property of all the fish samples shows no observable change with time. The result suggests that the magnetic particles in fish must be large enough to carry a stable magnetization. Not much remanent magnetization would be gained for this kind of magnetic particles by aggregation. This is in agreement with those magnetite particles discovered in other fish species [Wal84, Kir85b, Man88].

The fish bodies yield a saturation IRM several tens of times higher than that of the fish heads. In order to find out the strong source of the magnetic moment, guts of Tilapias fishes were isolated and measured. The saturation IRM of guts is close to that of the bodies. The results indicate that the magnetic signals from fish bodies may mainly come from the food. It could not be absolutely excluded that the signals from the head region is also related to food intake. However, magnetic material per volume in the fish heads is in fact relatively higher than that in the fish bodies. If a magnetoreceptor consisting of magnetite particles does exist in fish, it will more likely be located in the head region.

6.3.2 Detection of magnetic particles in fish tissues by MFM

6.3.2.1 Sample preparation and experiment

The olfactory lamellas have been postulated to contain magnetoreceptors in many vertebrates [Wal97, Han00]. Tissues of Tilapias fishes in a similar area (from mouth directing to eyes up to the area behind the nostrils) were prepared for MFM measurements. The tested area is sketched in Fig. 6.26. As MFM can only detect the stray field in the vicinity of the sample surface, tissues are sectioned into thin slices with a thickness of 2 μm. The lift height in the MFM measurements was set at 50 nm.

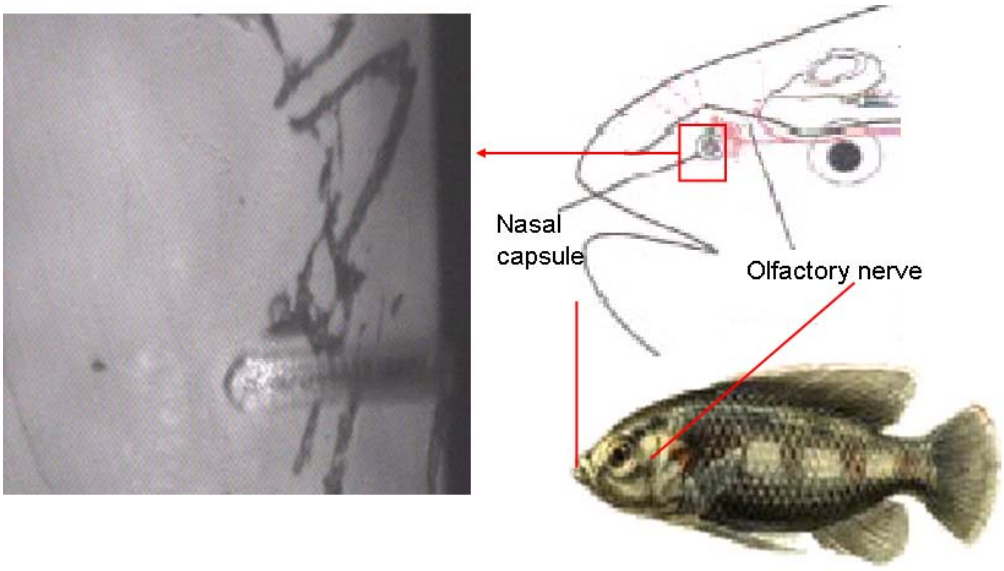

Fig. 6.26 Sketch of the measured part of the Tilapias fishes.

6.3.2.2 Results and discussion

Figure 6.27 shows AFM and MFM images of one slice tissue. Magnetic signals are observed at three locations, which are highlighted by a rectangle in the images. The tissue surface is relative rough (about 100 nm), giving rise to a crosstalk of topographical signals in the MFM image. However, the topography of the highlighted area in the AFM image is significantly different from the magnetic structure in the MFM image. Magnetic contrast is also convincingly strong as compared to the background. Therefore, the suspicion that the MFM signals are artificial due to the rough topography can be excluded.

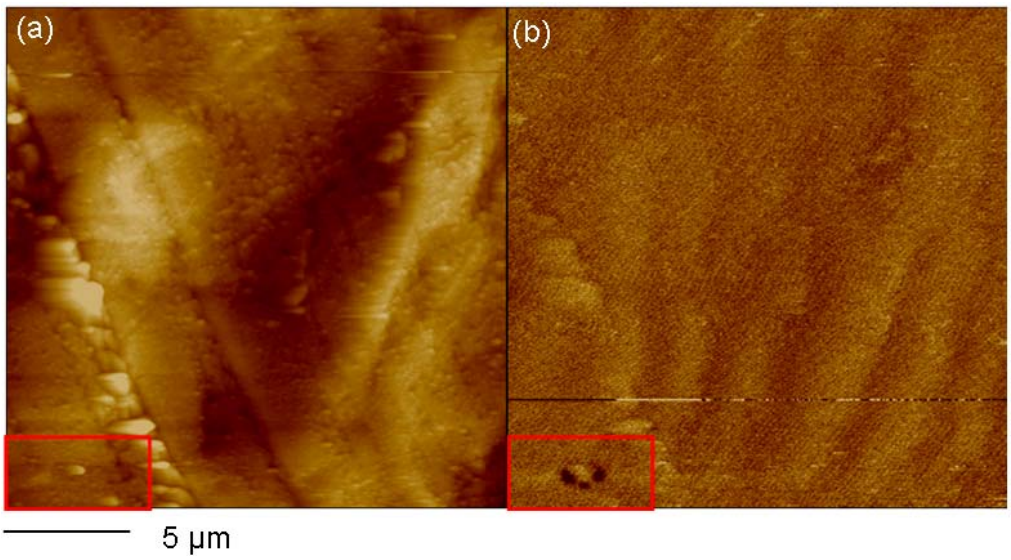

Fig. 6.27 AFM (a) and MFM (b) images of a tissue slice from the Tilapias fish.

The dark contrast in the MFM image indicates the existence of magnetic material, which is magnetized by the MFM tip. This is often the case for magnetite particles measured in absence of magnetic fields as shown the previous sections.

In Fig. 6.28, the area displaying magnetic signals is presented at a higher resolution. From the AFM image, this area looks relatively smooth and homogeneous. This implies that the magnetic material likely lies inside the tissue rather than on the surface.

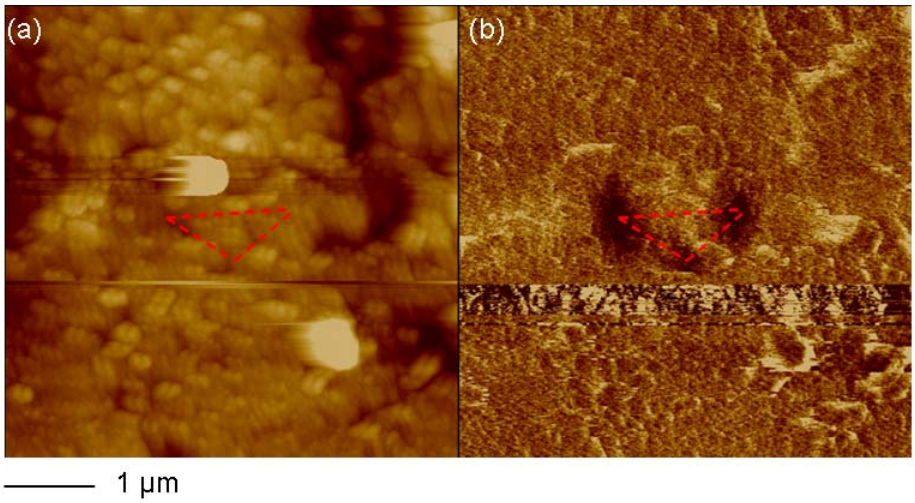

Fig. 6.28 (a) AFM and (b) MFM images of one tissue slice from the Tilapias fish.

The apparent magnetic structure is elongated, about 1 µm in length and 0.3 µm in width. This indicates that magnetic particles are arranged in an elongated structure. In fact, magnetite nanoparticles arranged in elongated structures are proposed in some models of magnetoreceptors [Kir81, Kir01].

AFM and MFM measurements have been performed for a series of tissue slices. However, other tissue slices do not show any clear magnetic contrast, including slices neighboring to the discussed one. As the discovered magnetic particles are only several tens of nanometers in size, a slice of 2 µm thickness is still too thick to obtain the precise arrangement of the particles by MFM.

It is quite a challenge to explore a fine arrangement of magnetic particles on a nanometer level in a tissue, which has millimeter dimension. In order to greatly reduce the huge time for AFM and MFM imaging, iron staining methods as described in Ref. [Tan69, Han00] should first be applied to exclude slices without iron content.

6.3.3 Conclusion

Magnetic material has been detected in Tilapias fishes and Zebra fishes. IRM acquisition and AF demagnetization have been performed to globally detect and characterize the magnetic material in these fishes. The results indicate that the detected magnetic material could result from groups of interacting magnetic particles. According to the saturation field of IRM, pure magnetite is the most possible magnetic material in Tilapias fishes, while other metallic iron alloys should be present for Zebra fishes. MFM was performed on tissue slices from the olfactory lamellas of Tilapias fishes. Embedded magnetic materials have been found and are possibly arranged in an elongated structure. However, in order to detect local arrangements of magnetic material in biological tissues, enormous time can be foreseen to be required because of the large number of slices and the slow imaging process by MFM.

Chapter 7

Magnetic structures of magnetite thin films

In this chapter, the magnetic structure of magnetite thin films is studied by MFM. The magnetic behavior of magnetite thin films is very different from that of the bulk material, e.g. in terms of an unexpected high saturation field and large coercive force [Mar96]. The reason is still not very clear. The magnetic properties of the magnetite thin films are found to be changed significantly by a short-time annealing in air [Zho04]. The mechanism is still uncertain. With the convenience to perform in-field measurements, MFM is employed as a powerful tool to better understand these unusual phenomena which occur for magnetite thin films.

7.1 Introduction

Fe_3O_4 (magnetite) is an attractive candidate material for magnetic tunnel junctions and spin-valve devices, because of its full spin polarization, high Curie temperature and high magnetization [Zie00, Suz01, Eer02b]. However, unexpectedly low efficiency of Fe_3O_4 multilayer spin valves was found [Zaa00] and the observed magnetic properties of Fe_3O_4 films are puzzling [Mar96, Mar97]. Conversion electron Mössbauer spectroscopy (CEMS) [Mar96, Mar97] and nuclear resonance data [Kal03] reveal a notable fraction of magnetic moments pointing out of the film plane, while an in-plane orientation would be expected from the interplay of crystalline, magnetoelastic and shape anisotropies [Mar96]. The films are still unsaturated at 7 T, whereas the magnetization is expected from the anisotropy to be saturated at much lower field values [Mar96]. These unexpected properties appear to be independent of the employed deposition methods and have been related to anti-phase boundaries (APB) existing in epitaxial films [Mar97]. In Fig. 7.1, an example of APB in magnetite is shown schematically. For Fe_3O_4 (001) grown on MgO (001), the lattice constant of

the film is twice that of the substrate. This results in stacking faults in the cation sublattice forming the APB. In particular, across most types of APB, a strong anti-ferromagnetic coupling is expected [Eer02a, Eer02b, Eer03].

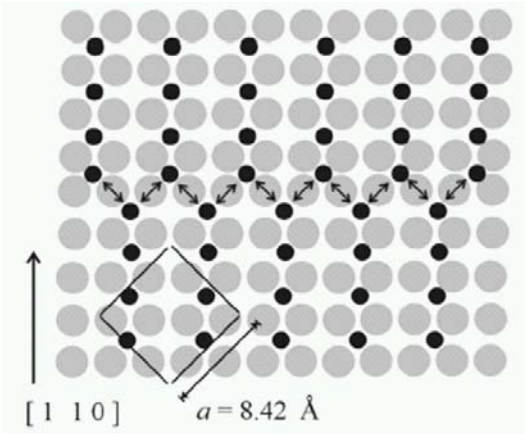

Fig. 7.1 Schematics showing a Fe_3O_4 (100) layer. Oxygen ions are displayed in grey and *B*-site iron ions ($Fe^{3+}_A [Fe^{3+} Fe^{2+}]_B O^{2-}_4$) in black. Across the anti-phase boundaries, there are additional 90°—Fe-O-Fe bonds (arrows).

From the application point of view, it would be most convenient if the magnetic properties of magnetite thin films resemble those of the bulk material. Increasing the "anti-phase domain size", i.e., the average distance between APB, is a key challenge for this purpose. Recently, it was shown that the additional annealing in air subsequent to an ultrahigh-vacuum annealing has a strong influence on the magnetic properties of samples. Such a treatment results in an increase of the magnetization at 1 T by 14% and in a decrease of coercive fields by 40% with respect to as-grown samples [Zho04]. In the light of another finding that the "domain wall resistance" across APB is huge, it could also be possible to use the APB itself as a spin valve [Eer02b].

It is thus important to study magnetic structures at APB and their correlation to the magnetic properties of magnetite thin films. MFM has been previously employed to investigate the domain structures of magnetite thin films, which are supposed to be defined by the APB [Bob01, Zie02, Pan02, Bol05]. Most of the results show magnetic

domain structures with a characteristic length scale of 100-300 nm, which is considerably larger than the average length of APB as mapped by TEM [Cel03, Eer03]. Furthermore, the irregularly shaped magnetic structures so far prevented a deeper understanding of the micromagnetism of magnetite films. In this work, a comparative MFM study on magnetite thin films under various preparation conditions is carried out to check the influence of the APB on the magnetic structures.

7.2 Epitaxial magnetite thin film preparation and characterization

Epitaxial magnetite thin films were grown on MgO single-crystal substrates by oxygen-plasma-assisted molecular beam epitaxy. The MgO substrates were cut along the <100> direction within ± 0.1°. The base pressure in the growth chamber was lower than 6.7×10^{-8} Pa. Each MgO substrate was annealed at 600 °C for 30 min in a plasma oxygen environment prior to deposition. The magnetite layer was deposited by means of e-gun evaporation from Fe pellets with a purity of 99.995% in a plasma oxygen environment of 6.7×10^{-8} Pa with a substrate temperature of 250 °C. Growth mode and crystalline quality of the films were monitored in situ by reflection high-energy electron diffraction (RHEED). The film thickness was controlled by quartz-crystal thickness monitors calibrated using x-ray reflectivity. The thicknesses of prepared films are 20 nm, 100 nm 400 nm, and 700 nm.

A BEDE D1 diffractometer was employed to carry out the high resolution x-ray diffraction (HRXRD) measurements. The diffractometer was equipped with a channel cut Si crystal monochromator. It was further equipped with a TTK 450 Anton Paar chamber. This facility allowed the samples to be annealed in situ without removing them from the HRXRD setup. Samples were annealed in air at 250 °C for 4 minutes. The position of the diffraction peaks and a reciprocal space map (RSM) were employed to evaluate the strain status of the epitaxial films during the treatment. Raman spectroscopy (RS) measurements were carried out before and after the

treatment to clarify the treatment-induced iron oxide phase of the magnetite surface. The four-probe method was employed in the resistance measurements. Hysteresis loop and magnetic moment measurements were carried out using a MicroMag 3900 alternating gradient force magnetometer at room temperature. To avoid the error introduced by the distribution of film thickness and volume among different film specimens, a single specimen was employed for magnetic measurements before and after the treatment. Each sample was in the form of a slice of Fe_3O_4, 0.5-0.7 mm thick and having lateral dimensions of 3-6 mm.

As annealing in air is always questioned because of uncontrolled film oxidation, we first analyze the change in the stoichiometry of the films induced by the treatment.

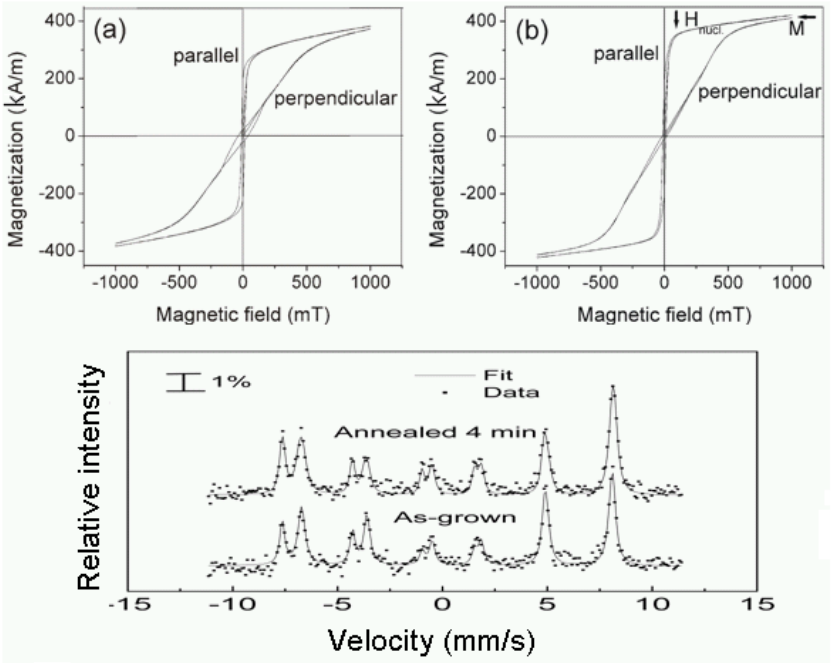

Fig. 7.2 Magnetization curves of (a) as-grown and (b) annealed Fe_3O_4 films for in-plane (parallel) and out-of-plane (perpendicular) magnetic fields. In-plane nucleation field and approximate saturation magnetization are indicated by arrows. (c) CEMS spectra of as-grown and annealed Fe_3O_4 films.

The change in the stoichiometry of the treated films was evaluated by a resistivity jump at a certain temperature [Zho04]. Verwey transition that is suppressed even by

small deviations from stoichiometry [She85] can still be observed in films subjected to a 4 min annealing. The result suggests that their stoichiometry remained close to that of ideal Fe_3O_4. The somewhat lower observed Verwey transition temperature of films (90~115 K) compared to values for single crystals (120 K) is in agreement with previous reports on magnetite films [Oga98]. From the magnetization curves as shown in Fig. 7.2 (a) and (b), γ-Fe_2O_3 inclusions formed from Fe_3O_4 via oxidation can be excluded, as γ-Fe_2O_3 has a smaller saturation magnetization of 392 A/m compared to 470 A/m for Fe_3O_4. This is in agreement with the RS measurements of original and treated films, which suggests that there are no traces of other iron oxide phases apart from magnetite [Zho04].

The deviation from stoichiometry is also checked by means of conversion electron Mössbauer spectroscopy (CEMS) after the MFM imaging [Wei06]. Fits to the spectra shown in Fig. 7.2 (c) indicate a 58 % reduction in the relation between mixed valence iron to trivalent iron, $\beta = Fe^{2.5+}/Fe^{3+}$, by a 4min annealing in air. From the relation: $\delta = (2-\beta)/(6+5\beta)$, a composition of $Fe_{(3-\delta)}O_4$ with $\delta = 0.03 \pm 0.01$ is obtained for the annealed film. As-grown samples show a perfect stoichiometry. The high stoichiometric resolution was obtained by measuring over several weeks.

The RHEED results suggest that the magnetite films were grown epitaxially as confirmed by the observed oscillations of pattern intensity. The out-of-plane and in-plane lattice parameters of the original film as calculated from the HRXRD results were 8.3604 and 8.4268 Å, respectively. The in-plane lattice parameter of the film is twice that of the MgO substrate implying that the film is fully strained on the MgO substrate without misfit dislocations.

The details of MFM measurements are presented in Chapter 2.3.

7.3 Magnetic structures of magnetite thin films

Figures 7.3 (a) and (b) show MFM images of as-grown Fe_3O_4 thin films of 100 nm and 400 nm thickness, respectively. Similar irregular domain structures have been observed before [Bob01, Zie02, Pan02, Bol05]. MFM images of the same Fe_3O_4 films after annealing for 4 minutes in air at 250 °C are shown in Figs. 7.3 (c) and (d). Upon annealing, a long-range ordered stripe-like magnetic domain structure has developed. The stripe domains exhibit some disorders at a smaller scale than the domain size. The insets in Figs. 7.3 (c) and (d) show the detailed structures of the stripe domains. Along with stripe domains, there are still some individual dots as marked in Figs. 7.3 (c) and (d).

Stripe domains in an essentially in-plane magnetized film have been observed before in permalloy [Sai64], cobalt [Heh96], and iron [Fos98] films. In such films, there is a perpendicular anisotropy that is smaller than the shape anisotropy. The magnetization in the respective weak stripe domains is tilted at alternating directions with respect to the film surface [Sai64]. In an external perpendicular field, weak stripe domains are transformed into bubble domains, as observed in Ref. [Heh96]. The same process is evident from Fig. 7.4, where the perpendicular field is stepwisely applied from +175 mT to -175 mT. A minimum film thickness of t_{min} is required for weak stripe domains to occur. We did not observe any stripe domains for a thickness of 20 nm. For $t > t_{min}$, the domain size is expected to scale with the square root of the film thickness [Sai64]. Domain sizes and thicknesses of the two films in Fig. 7.3 roughly follow this law. According to the theory, domains nucleate and develop into the stripe pattern upon reducing a saturating in-plane field. The stripes are preferentially oriented along the field direction. Our result agrees well with the theoretical predictions. The nucleation field is related to the perpendicular magnetic anisotropy and the minimum film thickness t_{min}. This relation yields a perpendicular anisotropy [Sai64] of $K = \mu_0 M_s H_{nucl} / \{2[1-(t_{min}/t)^{2/3}]\} \approx 5.7 \times 10^4$ J/m^3.

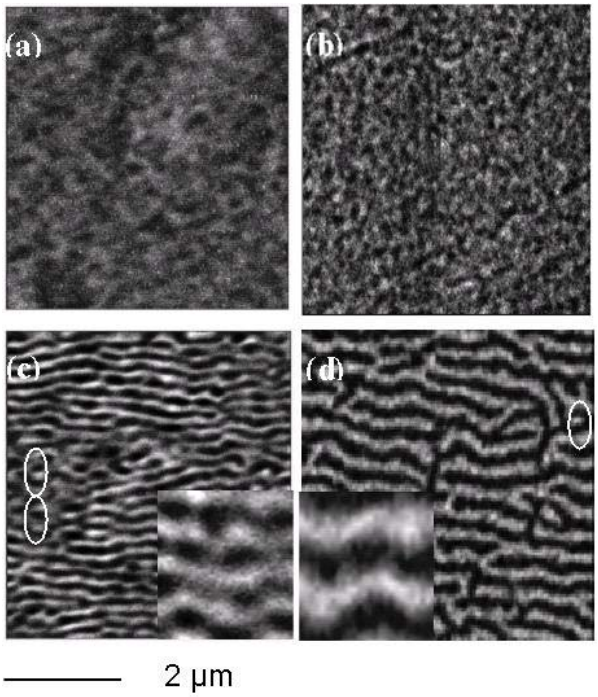

Fig. 7.3 MFM images of as-grown and annealed Fe_3O_4 films. (a) and (b) are images of as-grown Fe_3O_4 films of 100 nm and 400 nm thickness, respectively. (c) and (d) are the corresponding images of the films annealed for 4 minutes in air. The size of the insets is 1 µm x 1 µm. Individual dots in (c) and (d) are marked by circles.

The saturation magnetization M_s of the thin film and the nucleation field $\mu_0 H_{nucl}$ are taken from the in-plane magnetization curve (Fig. 7.2 (b)). The values are 420 kA/m and 100 mT, respectively. The film thickness t is 100 nm. The MFM images show that 20 nm < t_{min} < 100 nm. Assuming t_{min} = 50 nm for simplicity, one obtains a perpendicular anisotropy of about one half of the shape anisotropy, given by $\mu_0 M_s^2/2$ = 1.1×10^5 J/m^3. This perpendicular anisotropy is about five times larger than the crystalline anisotropy of bulk Fe_3O_4, i.e. 1.1×10^4 J/m^3 [Mar96]. The MFM data imply that an additional perpendicular anisotropy is induced by a few minutes of annealing in air. This is confirmed by CEMS data. A measure of in-plane orientation is given by the p parameter. For a film with homogenous magnetization, one obtains p = 2 $\sin^2\theta$ /(1+$\cos^2\theta$) with θ being the angle between the magnetization and the surface normal. The p value changes from 1.2 to 0.8 after annealing. p = 2 corresponds to an in-plane moment alignment, and p = 0 to a perpendicular alignment.

XRD data from Ref. [Zho04] show that the increase of strain is only a tenth of the strain value prior to annealing. Thus, the increase in strain cannot be responsible for a perpendicular anisotropy that is sufficient to generate stripe domains.

The APB with anti-ferromagnetic coupling are directly associated with a strong out-of-plane component of the magnetization [Kas06]. Chemical modification of APB during a short annealing is able to change the magnetic properties of Fe_3O_4 films substantially, even without a notable increase of the anti-phase domain size [Zho04]. The weak stripe domain pattern is the result of a competition between the perpendicular anisotropy and the domain wall energy [Hub98]. Chemical modification of APB during annealing in air can modify the domain wall energy [Eer03, Zho04]. The appearance of the stripe domains is quite likely caused by a change in the magnetic domain wall energy.

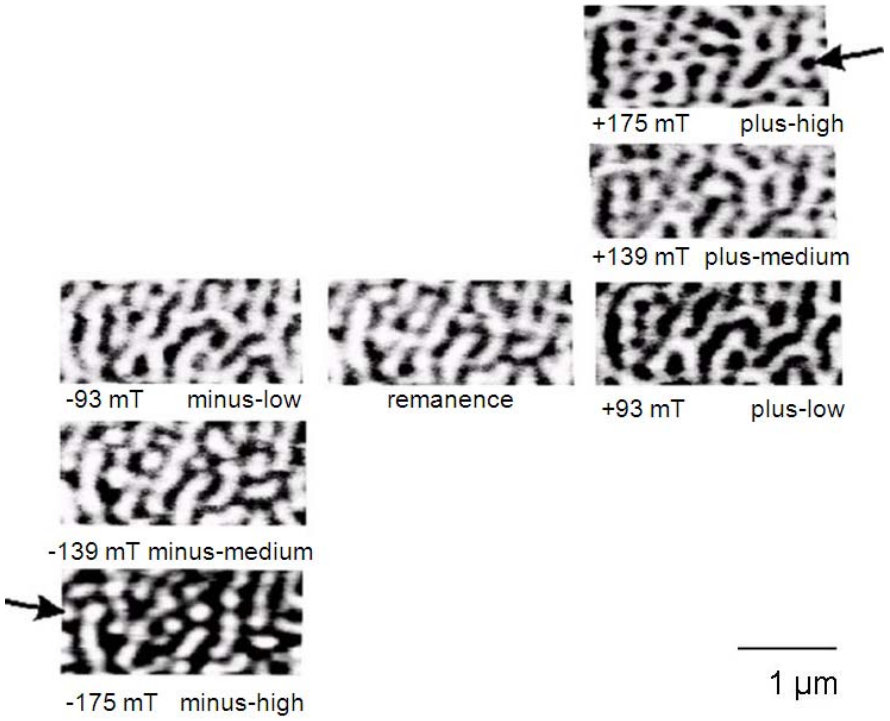

Fig. 7.4 MFM images of a representative film area during sweeping of the perpendicular field. For positive field values, images were inverted to account for the tip magnetization reversal. Arrows point to a typical dot. Because for every line, the average brightness is subtracted, the overall change in the magnetization is not reflected in the images.

In order to understand the behavior of APB, the development of magnetic structures

with the perpendicular external field is carefully analyzed. As shown in Fig. 7.4, in an external field perpendicular to the film, the stripe-domain structure partly decomposes into “dots” (bubble domains) with polarizations oppositely to the external field, and also oppositely to the magnetization of the environment (arrows in Fig. 7.4). Between subsequent field steps, most of the magnetic pattern remains unchanged and therefore can be used for precise alignment of the images. In Fig. 7.5 (a) images for field values from minus medium to plus medium were superimposed and averaged for some smaller area. In Fig. 7.5 (b), the minus-high-field image is superimposed to the plus-high-field image. The structure is largely the same in both images. This confirms the

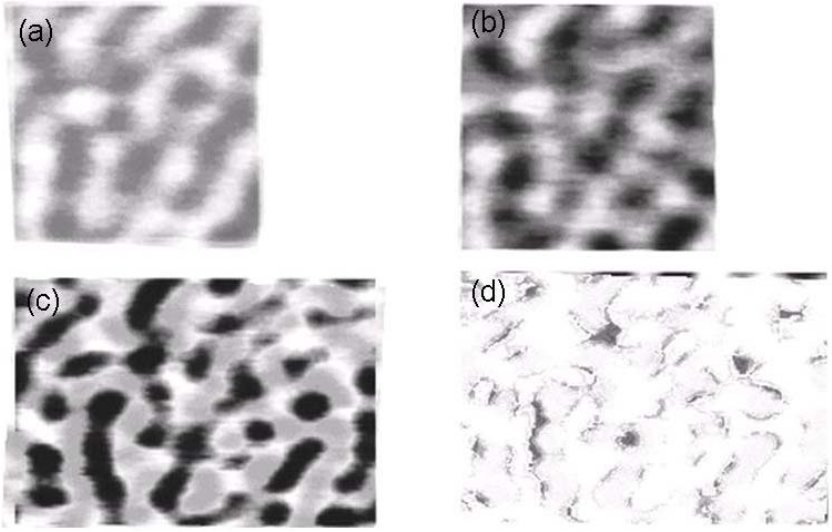

Fig. 7.5 (a) Superposition of all images from minus-medium to plus-medium, (b) superposition of the plus-high field image and the minus-high-field image, (c) black dots in the plus-high-field image are displayed further in black, the white dots in the minus-high-field image are displayed in gray, and (d) dark areas indicate changes from black in the plus-high-field image to white in the minus-high-field image.

immobility of the dots: A dot may change in size or polarization, but it does not move. In Fig. 7.5 (c), the black dots of the plus-high-field image (displayed in black) are superimposed to the white dots of the minus-high-field image (displayed in grey). The pattern is clearly non-random, with a tendency of black dots to have white neighbors and vice versa. Black and white dots frequently appear in pairs. In Fig. 7.5 (d), an AND operation was applied to the plus-high-field and the inverted minus-high-field

image such that those areas are shown in dark, where the magnetization has changed from black in the plus-high-field to white in the minus-high-field image. This indicates that reversal of dots is rare. Most reversal events take place upon changing from minus-medium to minus-high-field.

In Figs. 7.6 (a) and (b), most dots (indicated by crosses) remain unchanged by the change of the external field. A typical reversal event leads to a simultaneous change of contrast for a pair of domains. Six such pairs are marked by ovals in Figs. 7.6 (a) and (b). They change contrast as the field increases from minus-medium to minus-high. In the following, such pairs of domains are denoted as "dipolar centers." The observed dipolar reversal events are not induced by tip-sample interaction, because we found them oriented in all directions relative to the scan. There is no correlation between the magnetic and the topography image. The magnetization-switching events were observed apart from the dominating background effect: boundaries between black and white areas gradually move as the field sweeps and also the contrast between black and white neighboring areas changes. These observations at submicron scale correspond well with the overall magnetization curve (Fig. 7.2). The magnetization curve is essentially linear and non-hysteretic in the observed regime. This results from the incremental alignment of magnetization within the domains and mainly from the movement of the domain walls. Reversals of dipolar centers contribute to the small hysteresis observed.

In comparison to Ref. [Heh96], the dots appearing at high field can be identified as magnetic "bubble domains". Bubble domains attach themselves to pinning sites [Fos98]. That may explain the immobility of the dots, and their tendency to form dipolar centers in the plus-high-field and minus-high-field regimes (Fig. 7.4). Pinning of bubble domains is a well-known phenomenon. In contrast, magnetization reversal of dipolar centers, as shown in Fig. 7.6, is uncommon, and thus points toward an uncommon type of pinning site.

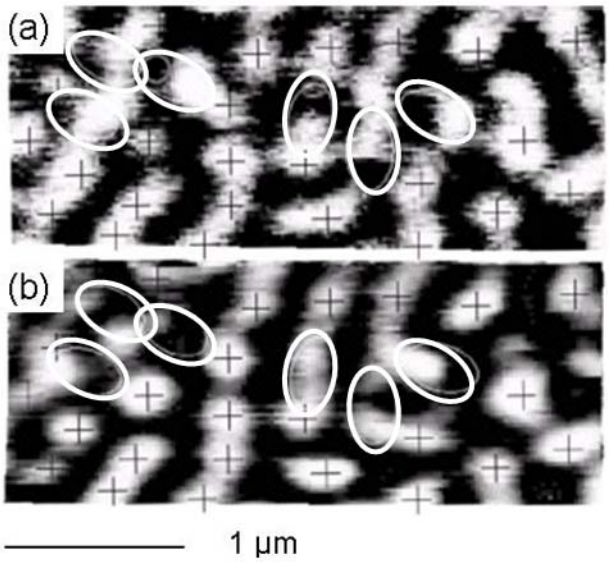

Fig. 7.6 MFM images of magnetite thin films at (a) minus-medium and (b) minus-high fields. Six locations of interest are shown by ovals. These include pairs of domains changing the contrast simultaneously: the black areas within each oval changes to white and vice versa. The magnetization of the environment (referenced by crosses) remains largely unchanged.

In the absence of pinning, a bubble domain of a certain volume V in its equilibrium position $x = 0$ experiences to a first approximation a harmonic potential $E(x)$ generated by the environment. The exchange constant of the defect-free film is A_0 and the effective anisotropy constant is K. The domain-wall width is then given by $d \propto (A/K_{\text{eff}})^{1/2}$ [Hub98]. An interface within the film is assumed to have an effective exchange constant A_1. For a conventional planar pinning site one has $0 \leq A_1 < A_0$, while for a magnetically ineffective interface $A_1 = 0$. An interface with anti-ferromagnetic exchange coupling has a negative exchange constant A_1, where perfect coupling yields $A_1 = -A_0$. The domain-wall energy E_{wall} is proportional to $|AK|^{1/2}$ [Hub98]. Energy can be gained by a shift of the bubble by Δx, placing the domain wall right at the interface. The overall potential experienced by the bubble now is a double potential, with a threshold energy of $\Delta E_{\text{wall}} \propto (A_0^{1/2} - |A_1|^{1/2})K^{1/2}$. There will be a jump of the bubble to another equilibrium position, if there is an additional field gradient of $\partial H/\partial x$ to overcome the threshold energy. This process requires $\mu_0|\partial H/\partial x|\Delta x M_s V > E_{\text{wall}}$. The reversal events seen in Fig. 7.6 can be caused by anti-ferromagnetic interfaces with $A_1<0$, but also by conventional pinning, $0 < A_1 < A_0$.

However, the pinning energy is higher for anti-ferromagnetic coupling: For an ideal anti-ferromagnetic interface, it is twice that of a nonmagnetic interface [Bob01, Eer02b]. The reversal events in Fig. 7.6 do ultimately not allow us to distinguish the difference in pinning energies, because various parameters in the above model cannot be obtained with sufficient precision.

Figure 7.7 displays MFM images of two samples of different APB density. The APB have been revealed by transmission electron microscopy images shown as insets. In both cases (220) two beam imaging conditions were adjusted. As a result the APB in Fig. 7.7 (a) show bright contrast. In Fig. 7.7 (b) APB are identified by the typical fringe contrast arising from phase shifts along inclined defects. For the film in Fig. 7.7 (b) with a thickness of 700 nm the anti-phase domain size is about 250 nm, in comparison to about 50 nm for the 200 nm thick film in Fig. 7.7 (a). For the 100 nm thick films investigated with respect to their magnetic properties, an APB structure similar to that of Fig. 7.7 (a) can be assumed [Eer02b]. The larger anti-phase domain size of the thicker film is expected from Ref. [Eer02b]. The anti-phase domain size in Fig. 7.7 (b) is well above the resolution limit of the MFM of about 80 nm in the present case. Figures 7.7 (a) and (b) further show the magnetic domain structures of 100 nm and 700 nm thick films, respectively. In Fig. 7.7 (b), the magnetic domain structure matches the anti-phase domain structure. The magnetization tends to be oriented in opposite directions at APB, as expected for anti-ferromagnetic coupling. In contrast, in Fig. 7.7 (a) the APB structure in the inset corresponds to the small-scale disorder present in the MFM image, while the magnetic domains are conventional stripe domains.

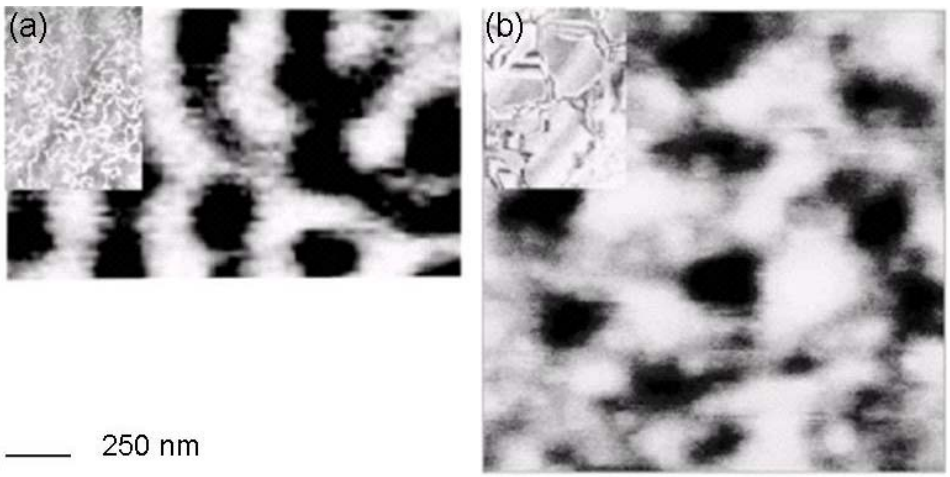

Fig. 7.7 MFM images of magnetite films with a thickness of 100 nm (a) and of 700 nm (b). Insets show TEM images of the APB structure for comparable films. All images are displayed at the same scale. The film in (b) has been thinned for TEM imaging.

A priori, it can again not be excluded that nonmagnetic interfaces with $A = 0$ are present with a respective structure. It is only in the high-field regime where the anti-ferromagnetic coupling leads to qualitatively new behavior. Above the nucleation field, a film with conventional pinning centers is saturated. At anti-ferromagnetic interfaces, a layer of opposite magnetization will persist, resulting in a reduced magnetization at high field. Since this is observed in all magnetization curves of the samples used in this study, there exists a high amount of anti-ferromagnetic coupling APB in the samples. It is therefore plausible that the results if Figs. 7.6 and 7.7 are at least in part caused by anti-ferromagnetic exchange coupling across APB.

7.4 Conclusion

A stripe-like magnetic domain structure has been found in Fe_3O_4 thin films annealed in air. The magnetization is predominantly in-plane. However, small out-of-plane components of the magnetization form the observed stripes, which are transformed into bubble domains in an external magnetic field. Magnetic domain structures are strongly affected by pinning sites. In fields of ±175 mT, MFM images show an irregular array of dots of opposite magnetization. Dots appearing in opposite external

fields are spatially correlated, with a tendency to form pairs. A few of such pairs show magnetization reversal during the field sweep. Reversal of dipolar centers was observed for isolated sites and in small groups. In a thick-film sample, MFM resolution is sufficient to directly resolve a magnetic domain structure mainly determined by APB. A tendency towards anti-parallel magnetization across APB is observed. The appearance of the domain structure is due to the annealing procedure. Chemical modification of APB during annealing is supposed to change the magnetic domain wall energy and gives rise to the perpendicular anisotropy.

Magnetite films have been considered for spin-valve applications. Here, soft magnetic layers are required with low coercivity and high saturation magnetization. The complex and persistent magnetic structure resulting from anti-ferromagnetic coupling across APB is an obstacle to such kind of applications. On most substrates, APB cannot be avoided. Annealing in UHV can only reduce the APB density. Subsequent partial oxidation is able to magnetically deactivate the APB to a certain degree. As a consequence, magnetization is approaching saturation much faster, i.e. the film becomes softer. We showed that partial oxidation also leads to a regular domain structure which is generally unwanted in spin-valve applications. However, film properties would rather be improved if anti-ferromagnetic coupling is reduced by deactivating the APB, while avoiding a perpendicular anisotropy. Alternative ways to chemically modify APB are needed, such as ion bombardment or other means of modifying the interface at an atomic scale.

The maximum magnetic field applied in this MFM study is 175 mT and the magnetite films are far from saturation. In order to fully understand the magnetic behavior of APB, it would be worth performing MFM measurements in a wide range of magnetic fields, where superconducting magnets should be considered.

Chapter 8

Summary

Nanoscale analysis has been performed on biogenic magnetite nanoparticles, synthesized magnetite nanoparticles, magnetite thin films, and hard disk write heads. The basic goal is to precisely characterize the magnetic structures of these interesting objects and investigate the influence of the magnetic structures on the magnetic properties. The main tools employed in the study are atomic force microscopy (AFM) and magnetic force microscopy (MFM). Two variants of MFM, i.e., high-frequency magnetic force microscopy (HF-MFM) and ferromagnetic resonance force microscopy (f-MRFM) have been set up for technical improvement or new applications.

Biogenic magnetite nanoparticles

AFM measurements show that biogenic magnetite nanoparticles produced by *Magnetospirillum gryphiswaldense* MSR-1 bacteria have a narrow size and shape distribution. The influence of the tip curvature on the measured particle size is examined. Based on geometrical models, the average particle size is precisely determined to be about 35.8±5 nm. The result is in agreement with the scanning electron microscopy analysis. According to the MFM results, magnetite particles have a single magnetic domain. In remanence, individual particles are easily polarized by the MFM tip, while particles aligned in chains are less influenced by the MFM tip. This is due to dipolar interactions among particles. In external magnetic fields, the dipolar stray fields of the magnetite nanoparticles are clearly observable by MFM. The dipole moments are switched when the external magnetic field is reversed. The magnetization reversal process of a two-particle chain has been recorded by MFM in a field range of ±68 mT. The change in the magnetic contrast of the two-particle chain

upon changing the external magnetic field was evaluated in a quantitative way. The maximum change occurs at 26 mT. This field magnitude is comparable to the dipolar field exerted on individual magnetite nanoparticles by their chain neighbors. The chain is saturated at 60 mT, which is in agreement with the result obtained by a cantilever magnetometer.

Magnetite particles extracted from salmon are ferromagnetic at habitation temperature and arranged in densely packed clusters according to the AFM and MFM results. The size of single magnetite particles is approximately 30 to 60 nm. The clusters are of spherical shape, and approximately 200 to 300 nm in diameter. The number of the particles within a cluster is in a range of 100 to 200. The MFM contrast is enhanced at the cluster edges, and saturates within a field range of 10 to 35 mT. According to the results of modelling, the remanent state of the clusters is a vortex with negligible total magnetic moment. In a magnetic field, this vortex state transforms into the saturated state by coherent rotation. At a lower field, the clusters can be regarded as spheres of constant permeability. The sensory mechanisms based on the assumption of an ensemble of superparamagnetic particles are thus valid for the investigated salmon samples.

Magnetite particles in various shapes, sizes and arrangements are deposited onto smooth surfaces for FMR investigation. During deposition and during the drying process, nanoparticle aggregates are subjected to external alignment magnetic fields and partially align. In the dry state, FMR measurements are performed with the magnetizing field along various directions. The arrangement of magnetite particles determines the magnetostatic interactions. The latter then influence the FMR spectra. Modelling of the spectra of the magnetite particles in bacterial cells is performed including magnetic dipolar interactions. The results prove that the most distinguished feature of bacterial FMR spectra arises from the chain arrangement of the particles. Other samples of magnetite particles in a more disordered arrangement could be modelled in terms of a random uniaxial anisotropy. In all cases modelling well

reproduces the experimental FMR spectra for the different magnetizing field orientations. Chain structures in biogenic samples can thus be identified by the specific FMR lineshapes.

Effort has been made to *in situ* detect magnetic materials in tissues. Magnetic materials have been detected in Tilapias fishes and Zebra fishes. According to the isothermal remanent magnetization and alternating magnetic field demagnetisation tests, the detected magnetic materials could be groups of interacting magnetic particles. The magnetic material in Tilapias fishes is magnetite, while other metallic iron alloys could not be excluded for Zebra fishes. MFM was performed on tissue slices from the olfactory lamellas of Tilapias fishes. Embedded magnetic materials have been found and are possibly arranged in an elongated structure. However, in order to detect local arrangements of magnetic material in biological tissues, enormous time can be foreseen to be required because of the large number of slices and the slow imaging process by MFM. Furthermore, comparative experiments show that the capability of MFM to detect embedded magnetic particles is much influenced by the roughness of sample surfaces and the depth of the embedded particles.

A ferromagnetic resonance force microscope has been set up *in situ* explore magnetic materials in organisms. The construction of the f-MRFM is explained in details. The set-up has been successfully tested by a piece of yttrium iron garnet film. Two methods have been developed, which allow controllable numbers of bacteria to be prepared on soft cantilevers for measurements. Detection of thousands of bacteria by the f-MRFM is proved to be a big challenge. Only a fraction of magnetite particles can satisfy the resonance condition at a given time due to the field gradient.

Further improvement of the set-up is necessary in order to detect magnetite nanoparticles in tissues, including applications of superconducting magnets for large fields and field gradients, better shielding systems to reduce the noise, and a vacuum system for a high resonance quality factor Q. The field modulation amplitude is suggested to be increased to the order of the FRM linewidth in order to obtain a better

performance of the double modulation scheme.

Synthesized magnetite nanoparticles

Synthesized magnetite nanoparticles are employed to investigate the effect of dipolar interactions on the structure formation and the magnetic property of magnetic particle aggregates.

Magnetic nanoparticle aggregates are formed on solid surfaces in four kinds of external magnetic fields. The formation of the particle aggregates is strongly influenced by dipolar interactions. In in-plane static magnetic fields, elongated particle islands with largely straight edges are built up along the field axis. Irregular particle islands with a rough topography are developed in static vertical magnetic fields. Spherical clusters with relatively small sizes are formed in in-plane rotating magnetic fields. In the absence of external magnetic fields, diverse structures including single particles of a few tens of nanometers to irregular clusters of a few microns in size have been observed. The typical scale and the height of the particle islands depend on the strength of the applied magnetic fields. The experimental results clearly support previously published numerical simulations on ferrofluids in a two-dimensional diffusion-limited system.

Magnetite nanoparticle suspensions with different particle concentrations, particle sizes and dispersion media have been investigated. These parameters can significantly modify the properties of the magnetic nanoparticle aggregates via dipolar interactions. Higher susceptibility per magnetic material weight is obtained for the magnetic particles with a higher particle concentration in the same dispersion medium. The dipolar interactions play a role to stabilize the particle magnetization against thermal agitation, which can be described as an enlargement of the effective particle size in the Langevin equation. The dispersion media can significantly influence the particle mobility and arrangement. This explains that the magnetic particles dispersed in the

fluids have a larger magnetic susceptibility than those in the elastic matrices with the same particle concentration.

Magnetite thin films

Epitaxial magnetite thin films shortly treated by additional annealing in air are investigated by MFM. Annealing leads to a stripe-like magnetic domain structure in the remanent state of the films. The domain structure has been identified as “weak strip domains”. The magnetization is predominantly in-plane. Small out-of-plane components of the magnetization form the observed stripes, which are transformed into bubble domains in an external magnetic field. Magnetic domain structures are strongly affected by pinning sites. Weak stripe domains indicate a moderate perpendicular anisotropy arising during annealing, which may arise from chemical modification of anti-phase boundaries (APB), influencing the anti-ferromagnetic coupling across APB.

In magnetic fields of ±175 mT, MFM images show an irregular array of bubbles of opposite magnetization. Most bubbles are pinned: The bubble structures in opposite fields transform into each other by incremental and reversible change. A few bubbles of opposite orientation however undergo simultaneous reversal during the field sweep. Such ‘dipolar centers’ were observed in isolation and in small groups. In a thicker film sample, MFM resolution is sufficient to resolve a magnetic domain structure on the length scale of the anti-phase domain size. The imaged magnetic structure is at least in part caused by anti-ferromagnetic exchange coupling across APB. The properties of magnetite films would rather be improved for the potential spin-valve applications if anti-ferromagnetic coupling is reduced by deactivating the APB.

High-frequency magnetic force microscopy

The super sharp MFM tips can greatly improve the spatial resolution of the HF-MFM. More details can be resolved in the interesting gap region of hard disk write heads. To image high frequency fields at hundreds of MHz, super sharp tips will be the best choice. However, the high frequency response of standard CoCr coatings is insufficient to image hard disk write heads above 1 GHz.

The ferrite-coated cantilevers can considerably improve the HF-MFM sensitivity as compared to the standard CoCr-coated ones. They allow HF-MFM imaging of hard isk write head with carrier frequencies of 2 GHz. The improvement of high-frequency response by the (Ni, Zn) ferrite-coated tips is due to their low coercivity, high susceptibility and high electrical resistivity. Due to their high cut-off frequency, $Ba_3Co_2Fe_{24}O_{41}$-coatings perform better than (Ni, Zn) ferrite-coatings. However, the overall thickness of these two coatings should be reduced in order to further improve the spatial resolution. This would require a better control of the growth process of ferrites on Si. Alternatively, a super sharp tip fabricated directly from a ferrite-coated MFM tip by the focused ion beam milling technique could be a possible solution.

Acknowledgements

My deepest gratitude goes first and foremost to Prof. Dr. Uwe Hartmann, my supervisor, for his constant encouragement and guidance. Without his consistent support, patience and kind understanding, this thesis would not have reached its present form. I would like to specially mention how much I admire the niceness in him. He is always a model for me in many roles, especially as a scientist and a friend.

I would like to sincerely thank and appreciate Dr. Ivo Knittel for his valuable cooperation and support through all the stages of my work.

I would like to acknowledge our entire group not only for the generous assistance in my research work but also for accompanying me through ups and downs. My thanks specially go to Dr. Yunhui Xu, Stefanie Neumann, Dr. Haibin Gao, Stefan Griesing, Dr. Michael Koblischka, Prof. Dr. Berhard, Möhl, Dr. Huijing Zhang, Dr. Pintu Das, Saleh Getlawi, Andreas English, Dr. Juliane Lösch, Dr. Radu Georgeta, Gabriele Kreutzer-Jungman, Dirk Matus, Adam Janoschka, Martin Loichen, Sandra Fass, Marc Gothe, and Marc Winter.

I am also grateful to Dr. Yang Zhou, Prof. Dr. Igor Shvets, Dr. Markus Gruner, Dr. Claus Lang, Prof. Dr. Dirk Schüler, Joris Peters, Prof. Dr. Sylvia Speller, Dr. Thomas Sulzbach, Dr. Christian Lang, Prof. Dr. Rainer Birringer, Dr. Falvio Soldera, Prof. Dr. Frank Mücklich, Achim Bittner, Luong van Ngo, Prof. Dr. Helmut Seidel, Dr. Birgit Fischer, Prof. Dr. Rolf Hempelmann, Dr. Hao Shen, Prof. Dr. Sanjay Mathur, Dr. Ralf Meckenstock, Dr. Michael Winklhofer, Dr. Alfonso Davila, Prof. Dr. Nikolai Peterson, Dr. Urs Gysin, Dr. Thomas Laeger, Prof. Dr. Uli Müller, for their fruitful cooperation and kind support.

And finally, I could not thank my beloved family enough for their deep love and constant belief in me through all these years. I also owe my sincerely gratitude to all my friends who let me have a feeling of being at home.

Publications (This Ph.D. work)

Articles

1. M. R. Koblischka, *J. D. Wei*, M. Kirsch, and U. Hartmann, High frequency magnetic force microscopy-imaging of harddisk write heads, Jap. J. Appl. Phys., **45**, No.3 B 2238 (2006)
2. * *J. D. Wei*, I. Knittel, U. Hartmann， Y. Zhou, S. Murphy, I. V. Shvets, and F. T. Parker, Influence of the antiphase domain distribution on the magnetic structure of magnetite thin films, Appl. Phys. Lett., **89**, 122517 (2006)
3. I. Knittel, *J. D. Wei*, Y. Zhou, S. K. Arora, I. V. Shvets, M. Luysberg, and U. Hartmann, Observation of antiferromagnetic coupling in epitaxial ferrite films, Phys. Rev. B, **74**, 132406 (2006)
4. *J. D. Wei*, M. Kirsch, M. R. Koblischka, and U. Hartmann, Optimization of high-frequency magnetic force microscopy by ferrite-coated cantilevers, J. Magn. Magn. Mat., **316**, 206 (2007).
5. M. R. Koblischka, M. Kirsch, *J. D. Wei*, T. Sulzbach, and U. Hartmann, Preparation of ferrite-coated MFM cantilevers, J. Magn. Magn. Mat., **316** e666 (2007).
6. M. R. Koblischka, *J. D. Wei*, and U. Hartmann, Optimization of the HF-MFM technique, J. Phys.: Conf. Ser., **61**, 591 (2007).
7. M. R. Koblischka, *J. D. Wei*, M. Kirsch, M. Lessel, R. Pfeifer, M. Brust, U Hartmann, C. Richter, and T Sulzbach, Search for the optimally suited cantilever type for high-frequency MFM, J. Phys.: Conf. Ser., **61**, 596 (2007).
8. M. R. Koblischka, *J. D. Wei*, T. Sulzbach, A. D. Johnston, and U. Hartmann, Observation of stray fields from hard-disk writer poles up to 2 GHz, IEEE Trans. Magn., **43**, 2205 (2007).
9. M. Kirsch, M. R. Koblischka, *J. D. Wei*, and U. Hartmann, Preparation of ferrite-coated magnetic force microscopy cantilevers, J. Vac. Sci. Technol. B, **25**, 1679 (2007).
10. A. Koblischka-Veneva, M. R. Koblischka, *J. D. Wei*, Y. Zhou, S. Murphy, F. Mücklich, U. Hartmann, and I. V. Shvets, Misorientations in [001] magnetite thin films studied by electron backscatter diffraction and magnetic force microscopy, J. Appl. Phys., **101**, 09M507 (2007).
11. M. R. Koblischka, *J. D. Wei*, C. Richter, T. H. Sulzbach, and U. Hartmann, Advanced cantilevers for magnetic force microscopy and high frequency magnetic force microscopy, Scanning, **30**, 27 (2008).
12. M. R. Koblischka, *J. D. Wei*, T. H. Sulzbach, and U. Hartmann, High-frequency MFM characterization of magnetic recording writer poles, Appl. Phys. A, **94**, 235 (2009).

13. I. Knittel, *J. D. Wei*, U. Hartmann, J. Peters, R. A. de Groot, S. Speller, and M. E. Gruner, Magnetic force microscopy of magnetic particle clusters from sensory cells of salmon, accepted by J. Magn. Magn. Mat..
14. *J. D. Wei*, I. Knittel, R. Meckenstock, C. Lang, D. Schüler, and U. Hartmann, Ferromagnetic resonance study on layers nanoparticles and chains of magnetite, submitted.
15. *J. D. Wei*, M. Lessel, I. Knittel, C. Lang, D. Schüler, and U. Hartmann, Atomic force microscopy and magnetic force microscopy study on biogenic magnetite nanoparticles, submitted.
16. *J. D. Wei*, I. Knittel, and U. Hartmann, Formation of magnetite nanoparticle aggregates on solid surfaces in external magnetic fields, submitted.
17. *J. D. Wei*, I. Knittel, U. Hartmann, J. Peters, R. A. de Groot, S. Speller, and M. E. Gruner, Atomic force microscopy and magnetic force microscopy study on magnetic particle clusters from sensory cells of salmon, submitted.

* Elite of Virtual Journal of Nanoscale Science & Technology. (http://scitation.aip.org/)

Conference contributions

German Physical Society 67th annual spring meeting, Dresden, Germany, 2003.
Talk: *J. D. Wei*, M. Oberringer, A. Mueller, Y. H. Xu, A. Janoschka, and U. Hartmann, AFM / MFM studies on the behavior of superparamagnetic clusters in external magnetic fields.

German Physical Society 69th annual spring meeting, Berlin, Germany, 2005.
Talk: *J. D. Wei* and U. Hartmann, Magnetic susceptibility of magnetite nanoparticles in biological Environments.
Poster: *J. D. Wei*, M. Koblischka, U. Hartmann, Y. Zhou, S. Muphy, and I. V. Shvets, Magnetic domain structures in Fe_3O_4 thin films studied by magnetic force microscopy.

German Physical Society 70th annual Meeting and 21st General Conference of the European Physical Society condensed Matter Division, Dresden, 2006.
Talk: *J. D. Wei*, I. Knittel, Y. Zhou, S. Murphy, I. V. Shvets, and U. Hartmann, Influence of the antiphase grain structure on the domain configuration of Fe_3O_4 thin films.

International Conference on Nanoscience and Technology (Nano9 meets STM 6), Basel, Switzerland, 2006.

Poster: *J. D. Wei*, M. Lessel, and U. Hartmann, Magnetic force microscopy on biogenic magnetite nanoparticles.

III Joint European Magnetic Symposia, San Sebastian, Spain, 2006
Talk: *J. D. Wei*, M. Kirsch, M. R. Koblischka, and U. Hartmann, Optimization of high-frequency magnetic force microscopy by ferrite-coated cantilevers.

German Physical Society 72th annual spring meeting, Berlin, Germany, 2008.
Talk: *J. D. Wei*, I. Knittel, R. Meckenstock, C. Lang, and U. Hartmann, Ferromagnetic resonance on biogenic and synthetic magnetite nanoparticles.

Literature

[Abe01] M. Abe and Y. Tanaka, J. Appl. Phys., **89**, 6766 (2001).

[Abe02] M. Abe and Y. Tanaka, IEEE Trans. Magn., **38**, 45 (2002).

[Abe04] M. Abe and Y. Tanaka, IEEE Trans. Magn., **40**, 1708 (2004).

[Abr87] D. L. Abraham and H. Hopster, Phys. Rev. Lett., **58**, 1352 (1987).

[Aha62] A. Aharoni, Rev. Mod. Phys., **34**, 227 (1962).

[Alb91] T. R. Albrecht, P. Grütter, S. Horne, and D. Rugar, J. Appl. Phys., **69**, 668 (1991).

[Alb05] M. Albrecht, V. Janke, S. Sievers, U. Siegner, D. Schüler and U. Heyen, J. Magn. Magn. Mater., **290**, 269 (2005).

[Aml99] I. Amlani, A. O. Orlov, G. Toth, G. H. Bernstein, C. S. Lent, and G. L. Snider, Science, **284**, 289 (1999).

[And99] S. Anders, H. A. Padmore, R. M. Duarte, T. Renner, T. Stammler, A. Scholl, M. R. Scheinfein, J. Stöhr, L. Séve, and B. Sinkovic, Rev. Sci. Instrum., **70**, 3973 (1999).

[Ape05] N. Apetroaie, A. Roca, and D. E. Creanga, J. Optoelectr. Adv. Mater., **7**, 2865 (2005).

[Ash97] K.G. Ashar, *Magnetic Disk Drive Technology*, IEEE Press, New York, 1997.

[Bac01] J. C. Bacri, R. Perzynski, M. I. Shliomis, and G. I. Burde, Phys. Rev. Lett., **75**, 2128 (1995).

[Bai88] M. N. Baibich, J. M. Broto, A. Fert, F. Nguyen Van Dau, F. Petroff, P. Etienne, G. Creuzet, A. Friederich, and J. Chazelas, Phys. Rev. Lett., **61**, 2472 (1988).

[Ban85] S. K. Banerjee and B. M. Moskowitz, *Ferrimagnetic properties of magnetite*, edited by J. L. Kirschvink, D. S. Jones, and B. J. MacFadden, Magnetite Biomineralization and Bagnetoreception in Organisms, Plenum, New York, 1985.

[Ban88] M. Bander and D. L. Mills, Phys. Rev. B, **38**, 12015 (1988).

[Ban05] I. A. Banerjee, L. Yu, M. Shima, T. Yoshino, H. Takeyama, T. Matsunaga, and H. Matsui, Adv. Mater., **17**, 1128 (2005).

[Ber00] G. P. Berman, G. D. Doolen, P. C. Hammel, and V. I. Tsifrinovich, Phys. Rev. B, **61**, 14694 (2000).

[Ber03] C. C. Berry and A. S. G. Curtis, J. Phys. D: Appl. Phys., **36**, R198 (2003).

[Bic50] L . R . Bickford, Phys. Rev., **78**, 449 (1950).

[Bin82] G. Binnig and H. Rohrer, Helv. Phys. Acta., **55**, 726 (1982).

[Bin89] G. Binasch, P. Grünberg, F. Saurenbach, and W. Zinn, Phys. Rev. B, **39**, 4828 (1989).

[Bla75] R. Blakemore, Science, **190**, 377 (1975).

[Blu01] S. Blundell, *Magnetism in Condensed Matter*, Oxford University Press, New York, 2001.

[Bob01] J. F. Bobo, D. Basso, E. Snoeck, C. Gatel, D. Hrabovsky, J. L. Gauffier, L. Ressier, R. Mamy, S. Visnovsky, J. Hamrle, J. Teillet, and A. R. Fert, Eur. Phys. J. B, **24**, 43 (2001).

[Bol05] A. Bollero, M. Ziese, R. Höhne, H. C. Semmelhack, U. Köhler, A. Setzer, and P. Esquinazi, J. Magn. Magn. Mater., **285**, 279 (2005).

[Bro62] W. F. Brown, *Magnetostatic Principles in Ferromagnetism*, North-Holland, Amsterdam, 1962.

[Bro63] W. F. Brown, *Micromagnetics*, Wiley, New York, 1963.

[Bru95] K. J. Bruland, J. Krzystek, J. L. Garbini, and J.A. Sidles, Rev. Sci. Instrum., **66**, 2853 (1995).

[Bru98] K. J. Bruland, W. M. Dougherty, J. L. Garbini, J. A. Sidles, and S. H. Chao, Appl. Phys. Lett., **73**, 3159 (1998).

[But75] R. F. Butler and S. K. Banerjee, J. Geophys. Res., **80**, 4049 (1975).

[But03] K. Butter, P. H. H. Bomans, P. M. Frederik, G. J. Vroege, and A. P. Philipse, Nature Mater., **2**, 88 (2003).

[Ceb83] D. J. Cebula, S. W. Charles, and J. Popplewell, J. Physique, **44**, 207 (1983).

[Cel03] S. Celotto, W. Eerenstein, and T. Hibma, Eur. Phys. J. B, **36**, 271 (2003).

[Cha84] J. N. Chapman, J. Phys. D: Appl. Phys., **17**, 623 (1984).

[Cha02] V. Charbois, V. V. Naletov, J. B. Youssef, and O. Klein, J. Appl. Phys., **91**, 7337 (2002).

[Cho01] B. C. Choi, M. Belov, W. K. Hiebert, G. E. Ballentine, and M. R. Freeman, Phys. Rev. Lett., **86**, 728 (2001).

[Chu86] E. M. Chudnovsky, W. M. Saslow, and R. A. Serota, Phys. Rev. B, **33**, 251 (1986).

[Cis81] S. Cisowski, phys. Earth planet inter., **26**, 56 (1981).

[Coe88] R. Coehoorn, D. B. de Mooij, J. P. W. B. Duchateau, and K. H. J. Buschow, J. Physique Coll. **49**, 669 (1988).

[Coe98] J. M. D. Coey, A. E. Berkowitz, L. Balcells, F. F. Putris, and A. Barry, Phys. Rev. Lett., **80**, 2815 (1998).

[Coe05] J. M. D. Coey, M. Venkatesan, and C. B. Fitzgerald, Nature Mater., **4**, 173 (2005).

[Com99] R. L. Comstock, *Introduction to Magnetism and Magnetic Recording*, Wiley, New York, 1999.

[Cor88] B. W. Corb, IEEE Trans. Magn., **24**, 2838 (1988).

[Cox95] P. A. Cox, *Transition Metal Oxides: An Introduction to Their Electronic Structure and Properties*, Clarendon Press, Oxford, 1995.

[Dah95] E. D. Dahlberg and J. G. Zhu, Phys. Today, April, 35 (1995).

[Dah99] E. D. Dahlberg and R. Proksch, J. Magn. Magn. Mater., **200**, 720 (1999).

[Day77] R. Day, M. Fuller, and V.A. Schmidt, Phys. Earth Planet. Inter., **13**, 260 (1977).

[Dav05] A. F. Davila, M. Winklhofer, V. P. Shcherbakov, and N. Petersen, Biophys. J., **89**, 56 (2005).

[Dec01] M. F. DeCamp, D. A. Reis, P. H. Bucksbaum, B. Adams, J. M. Caraher, R. Clarke, C. Conover, E. Dufresne, R. Merlin, V. Stoica, and J. K. Wahlstrand, Nature, **413**, 825 (2001).

[Die00] C. E. Diebel, R. Proksch, C. R. Green, P. Neilson, and M. M. Walker, Nature, **406**, 299 (2000).

[Don99] L. N. Donselaar, P. M. Frederik, P. Bomans, P. A. Buining, B. M. Humbel, and A. P. Philipse, J. Magn. Magn. Mater., **201**, 58 (1999).

[Dor95] J. L. Dormann, and D. Fiorani, J. Magn. Magn. Mater., **140**, 415 (1995).

[Dun97] D. J. Dunlop and Ö. Özdemir, *Rock Magnetism: Fundamentals and Frontiers*, Cambridge University Press, Cambridge, 1997.

[Ebe05] D. Eberbeck, V. Janke, S. Hartwig, U. Heyen, D. Schüler, M. Albrecht, and L. Trahms, J. Magn. Magn. Mater., **289**, 70 (2005).

[Ede00] R. L. Edelstein, C. R. Tamanaha, P. E. Sheehan, M. M. Miller, D. R. Baselt, L. J. Whitman, and R. J. Colton , Biosen. Bioelectr., **14**, 805 (2000).

[Eer02a] W. Eerenstein, T. T. M. Palstra, T. Hibma, and S. Celotto, Phys. Rev. B, **66**, 201101R (2002).

[Eer02b] W. Eerenstein, T. T. M. Palstra, S. S. Saxena, and T. Hibma, Phys. Rev. Lett., **88**, 247204 (2002).

[Eer03] W. Eerenstein, T. T. M. Palstra, T. Hibma, and S. Celotto, Phys. Rev. B, **68**, 014428 (2003).

[Ele96] Y. Elezzabi, M. R. Freeman, and M. Hohnson, Phys. Rev. Lett., **77**, 3220 (1996).

[Eri89] A. B. Eriksson and M. Jonson, Phys. Rev. B, **40**, 884 (1989).

[Erl88] R. Erlandsson, G. McClelland, C. Mate, and S. Chiang, J. Vac. Sci. Technol. A, **6**, 266 (1988).

[Eva06] P. G. Evans and E. D. Isaacs, J. Phys. D: Appl. Phys., **39**, R245 (2006).

[Eva03] M. E. Evans and F. Heller, *Environmental Magnetism: Principles and Applications of Enviromagnetics*, Academic Press, Oxford, 2003.

[Ewi02] G. A. van Ewijk, G. J. Vroege and A. P. Philipse, J. Phys.: Condens. Matter., **14**, 4915 (2002).

[Fer99] J. Ferré J, J. P. Jamet, and P. Meyer, Phys. Stat. Sol. (a), **175**, 213 (1999).

[Fla88] P. J. Flanders, J. Appl. Phys., **63**, 3940 (1988).

[Fle94] P. E. J. Flewitt and R. K. Wild, *Physical Methods for Materials Characterization*, Institute of physics publishing, Bristol and Philadelphia, 1994.

[Fon96] S. Foner, J. Appl. Phys., **79**, 4740 (1996).

[Fos98] S. Foss, C. Merton, R. Proksch, G. Skidmore, J. Schmidt, E. D. Dahlberg, T. Pokhil, and Y. T. Cheng, J. Magn. Magn. Mater., **190**, 60 (1998).

[Fre96] M. R. Freeman and J. F. Smyth, J. Appl. Phys., **79**, 5898 (1996).

[Fre97] M. R. Freeman, A. Y. Elezzabi, and J. A. H. Stotz, J. Appl. Phys., **81**, 4516 (1997).

[Fru99] O. Fruchart, J. P. Nozieres, W. Wernsdorfer, D. Givord, F. Rousseaux, and D. Decanini, Phys. Rev. Lett., **82**, 1305 (1999).

[Gam07] L. F. Gamarra, G. E. S. Brito, W. M. Pomtuschka, J. B. Mamani, C. A. Moreira-Filho, and E. Amaro, Braz. J. Phys., **37**, 1288 (2007).

[Gar55] M. A. Garstens and J. I. Kaplan, Phys. Rev., **99**, 459 (1955).

[Gif46] J. H. E. Giffiths, Nature, **158**, 670 (1946).

[Gij04] M. A. M. Gijs, Microfluid. Nanofluid., **1**, 22 (2004).

[Giv96] D. Givord and M. F. Rossignol, *Rare-Earth Iron Permanent Magnets*, Clarendon Press, Oxford, 1996.

[Gol90] A. Goldman, *Modern Ferrite Technology*, Van Nostrand, New York, 1990.

[Gri74] D. L. Griscom, Geochim. Cosmochim. Acta, **38**, 1509 (1974).

[Gri81] D. L. Griscom, J. Magn. Reson., **45**, 81 (1981).

[Gri88] D. L. Griscom, J. J. Kerbs, A. Perez, and M. Treilleux, Nucl. Instrum. Methods Phys. Res. Sect. B, **32**, 272 (1988).

[Grü90] P. Grütter, T. Jung, H. Heinzelmann, A. Wadas, E. Meyers, H. R. Hidber, and H. J. Güntherodt, J. Appl. Phys., **67**, 1437 (1990).

[Grü92] P. Grütter, H. J. Mamin and D. Rugar, *Magnetic Force Microscopy*, edited by R. Wiesendanger and H.J. Güntherodt, Springer Series in Surface Sciences, Vol. 28, Springer, Berlin Heidelberg, 1992.

[Grü04] K. Grünberg, E. C. Müller, A. Otto, R. Reszka, D. Linder, M. Kube, R. Reinhardt, and D. Schüler, Appl. Environ. Microbiol., **70**, 1040 (2004).

[Gua03] D. Guarisco and H. Nguy, J. Appl. Phys., **93**, 6745 (2003).

[Gup96] A. Gupta, G. Q. Gong, G. Xiao, P. R. Duncombe, P. Lecoeur, P. Trouilloud, Y. Y. Wang, V. P. Dravid, and J. Z. Sun, Phys. Rev. B, **54**, R15629 (1996).

[Had99] G. C. Hadjipanayis, J. Magn. Magn. Mater., **200**, 373 (1999).

[Han00] M. Hanzlik, C. Heunemann, E. Holtkamp-Rötzler, M. Winklhofer, N. Petersen, and G. Fleissner, BioMetals, **13**, 325 (2000).

[Han02] M. Hanzlik, M. Winklhofer, and N. Petersen, J. Magn. Magn. Mater., **248**, 258 (2002).

[Har88] U. Hartmann, J. Appl. Phys., **64**, 1561 (1988).

[Har91] U. Hartmann, T. Göddenhenrich, and C. Heiden, J. Magn. Magn. Mater., **101**, 263 (1991).

[Har94] U. Hartmann, Adv. Electron. Electron Phys., **87**, 49 (1994).

[Har99] U. Hartmann, Annu. Rev. Mater. Sci., **29**, 53 (1999).

[Hay96] T. Hayashi, S. Hirono, M. Tomita, and S. Umemura, Nature, **382**, 772 (1996).

[Heh96] M. Hehn, S. Padovani, K. Ounadjela, and J. P. Bucher, Phys. Rev. B, **54**, 3428 (1996).

[Hel88] G. Helgesen, A. T. Skjeltorp, P. M. Mors, R. Botet, and R. Jullien, Phys. Rev. Lett., **61**, 1736 (1988).

[Hel02] L. E. Helseth, A. G. Solovyev, R. W. Hansen, E. I. Il'yashenko, M. Baziljevich, and T. H. Johansen, Phys. Rev. B, **66**, 064405 (2002).

[Hem86] K. Hemmes, W. Lisowski, J. C. Lodder, L.J. Hanekamp, and T. J. A. Popma, J. Phys. D: Appl. Phys., **19**, 1311 (1986).

[Her05] R. Hergt, R. Hiergeist, M. Zeisberger, D. Schüler, U. Heyen, I. Hilger, and W. A. Kaiser, J. Magn. Magn. Mater., **293**, 80 (2005).

[Hey03] U. Heyen, and D. Schüler, Appl. Microbiol. Biotechnol., **61**, 536 (2003).

[Hib99] T. Hibma, F. C. Voogt, L. Niesen, P. A. A. van der Heijden, W. J. M. de Jonge, J. J. T. M. Donkers, and P. J. van der Zaag, J. Appl. Phys., **85**, 5291 (1999).

[Hsu07] C. L. Hsu, Y. R. Yang, and K. Wood, Chin. J. Phys, **45**, 686 (2007)

[Hub98] A. Hubert and R. Schäfer, *Magnetic Domains: The Analysis of Magnetic Microstructures*, Springer, Berlin Heidelberg, 1998.

[Isr92] J. Israelachvili, *Intermolecular Surface Force*, Academic Press, London, 1992.

[Jab92] W. Jabssen, *Streifenleiter und Hohlleiter*, Hüthig, Heidelberg, 1992.

[Jac64] R. C. Jacklevic, J. S. Lambe, A. H. Silver, and J. E. Mercerau, Phys. Rev. Lett., **12**, 159 (1964).

[Jai01] L. J. E. Jaick, D. A. Avalos, D. M. S. Esquivel, E. Wajnberg, and M. P. Linhares, Eur. Biophys. J., **29**, 579 (2001).

[Jey01] B. Jeyadevan, I. Nakatani, H. Oka, and K. Thoji, Braz. J. Phys., **31**, 347 (2001).

[Jun95] P. Jund, S. G. Kim, D. Tomanek, and J. Hetherington, Phys. Rev. Lett., **74**, 3049 (1995).

[Kal03] L. A. Kalev and L. Niesen, Phys. Rev. B, **67**, 224403 (2003).

[Kas06] T. Kasama, R. E. Dunin-Borkowski, and W. Eerenstein, Phys. Rev. B, **73**, 104432 (2006).

[Kha91] S. N. Khanna and S. Linderoth, Phys. Rev. Lett., **67**, 742 (1991).

[Kir81] J. L. Kirschvink and J. L. Gould, BioSystems, **13**, 181 (1981).

[Kir83] J. L. Kirschvink, S. J. Williamson, G. L. Romani, L. Kaufman, and I. Modena, *Biomagnetism: An interdisciplinary approach*, Plenum, New York, 1983.

[Kir85a] J. L. Kirschvink, D. S. Jones, and B. J. MacFadden, *Magnetite Biomineralization and Magnetoreception in Organisms: A New Biomagnetism*, Plenum, New York, 1985.

[Kir85b] J. L. Kirschvink, M. M. Walker, S. B Chang, A. E. Dizon, and K. A. Peterson, J. Comp. Physiol. A, **157**, 375 (1985).

[Kir00] K. J. Kirk, Contemp. Phys., **41**, 61 (2000).

[Kir01] L. Kirschvink, M. M. Walker, and C. E. Diebel, Current Opinion in Neurobiology, **11**, 462 (2001).

[Kir07] M. Kirsch, M. R. Koblishka, J. Wei, and U. Hartmann, J. VAc. Sci. Technol. B, **25**, 1679 (2007).

[Kit49] C. Kittel, Rev. Mod. Phys., **21**, 541 (1949).

[Kle03] O. Klein, V. Cahrbois, V. V. Naletov, and C. Fermon, Phys. Rev. B., **67**, 220407 (2003).

[Kob95] A. Kobayashi, J. L. Kirschvink, and M. Blank, *Electromagnetic Fields: Biological Interactions and Mechanisms*, American Chemical Society Books, Washington, DC., 1995.

[Kob03] M. R. Koblischka, U. Hartmann and T. Sulzbach, Mater. Sci. Eng.: C, **23**, 747 (2003).

[Kob04] M. R. Koblischka, U. Hartmann and T. Sulzbach, J. Magn. Magn. Mat., **272**, 2138 (2004).

[Kob06] M. R. Koblischka, J. Wei, M. Kirsch, and U. Hartmann, Jpn. J. Appl.Phys., **45**, 2238 (2006).

[Kob08] M. R. Koblischka, J. Wei, C. Richter, T. H. Sulzbach, and U. Hartmann, Scanning, **30**, 27 (2008).

[Kop06a] R. E. Kopp, C. Z. Nash, A. Kobayashi, B. P. Weiss, D. A. Bazylinski, and J. L. Kirschvink, J. Geophys. Res. B, **111**, B12S25 (2006).

[Kop06b] R. E. Kopp, B. P. Weiss, A. C. Maloof, H. Vali, C. Z. Nash, and J. L. Kirschvink, Earth Planet. Sci. Lett., **247**, 10 (2006).

[Kon88] D. C. Koningsberger and R. Prins, *X-ray Absorption: Priciples, Applications, Techniques of EXAFS, SEXAFS and XANES,* John Wiley & Sons, New York, 1988.

[Kro87] H. Kronmüller, Phys. Stat. Soli. (b), **144**, 385 (1987).

[Kro88] H. Kronmüller, K. D. Durst, and M. Sagawa, J. Magn. Magn. Mater., **74**, 291 (1988).

[Kuk89] Y. Kuk and P. J. Silverman, Rev. Sci. Instrum., **60**, 165 (1989).

[Lal04] Y. Lalatonne, J. Richardi, and M. P. Pileni, Nat. Mater., **3**, 121 (2004).

[Lan06] C. Lang and D. Schueler, J. Phys.: Condens. Matter, **18**, S2815 (2006).

[Len93] C. S. Lent, P. D. Tougaw, W. Porod, and G. H. Bernstein, Nanotechnology, **4**, 49 (1993).

[Li02] S. Li, S. Stokes, Y. Liu, S. Foss-Schroder, W. Zhu, and D. Palmer, J. Appl. Phys., **91**, 7346 (2002).

[Li03] S. Li, *Science, Technology and Education of Microscopy: an Overview*, Formatex, Badajoz, 2003.

[Liu96] F. H. Liu, H. Tong, and L. Miloslavsky, IEEE Trans. Magn., **32**, 3536 (1996).

[Liu00] J. P. Liu, R. Skomski, Y. Liu, and D. J. Sellmyer, J. Appl. Phys., **87**, 6740 (2000).

[Loh99] J. Lohau, S. Kirsch, A. Carl, G. Dumpich, and E. F. Wassermann, J. Appl. Phys., **86**, 3410 (1999).

[Man88] S. Mann, N. H. C. Sparks, M. M. Walker, and J. L. Kirschvink, J. Exp. Biol., **140**, 35 (1988).

[Mar87] Y. Martin and H. K. Wickramasinghe, Appl. Phys. Lett., **50**, 1455 (1987).

[Mar96] D. T. Margulies, F. T. Parker, F. E. Spada, R. S. Goldman, J. Li, R. Sinclair, and A. E. Berkowitz, Phys. Rev. B, **53**, 9175 (1996).

[Mar87] Y. Martin, C. C. Williamus, and H. K.Wickramasinghe, J. Appl. Phys., 61, 4723 (1987)

[Mar97] D. T. Margulies, F. T. Parker, M. L. Rudee, F. E. Spada, J. N. Chapman, P. R. Aitchison, and A. E. Berkowitz, Phys. Rev. Lett., **79**, 5162 (1997).

[Mar98] J. A. Marohn, R. Fainchtein, and D. D. Smith, Appl. Phys. Lett., **73**, 3778 (1998).

[Mat87] T. Matsunaga and S. Kamiya, Appl. Microbiol. Biotechnol., **26** 328 (1987).

[Mat90] J. Matsuda, K. Aoyagi, Y. Kondoh, M. Iizuka, and K. Mukasa, IEEE Trans. Magn., **26**, 2061 (1990).

[Mat02] N. Matsushita, C. P. Chong, T. Mizutani, and M. Abe, J. Appl. Phys., **91**, 7376 (2002).

[Mcl87] G. M. Mclelland, R. Erlandsson, S. Chiang, *Review of Progress in Quantitative Non-destructive Evaluation*, Plenum, New York, 1987.

[Meh97] R. V. Mehta, R. V. Upadhyay, S. W. Charles, and C. N. Ramchand, Biotechnol. Techn., **11**, 493 (1997).

[Mey88] G. Meyer and N. M. Amer, Appl. Phys. Lett., **53**, 1045 (1988).

[Mid00] M. M. Midzor, P. E. Wigen, D. V. Pelekhov, W. Chen, P. C. Hammel, and M. L. Roukes, J. Appl. Phys., **87**, 6493 (2000).

[Mor94] S. Morup and E. Tronc, Phys. Rev. Lett., **72**, 3278 (1994).

[Mor99] H. Morimoto and T. Maekawa, Inter. J. Mod. Phys. B, **13**, 2085 (1999).

[Mor00] H. Morimoto and T. Maekawa, J. Phys. A: Math. Gen., **33**, 247 (2000).

[Mor01] P. Moroz, S. K. Jones, and B. N. Gray, J. Surg. Oncol., **77**, 259 (2001).

[Mor03] J. Moreland, J. Phys. D: Appl. Phys., **36**, R39 (2003).

[Mor04] C. V. Mora, M. Davison, J. M. Wild, and M. M. Walker, Nature, **432**, 508 (2004).

[Mos93] M. B. Moskowitz, R. B. Frankel, and D. A. Bazylinski, Earth Planet. Sci. Lett., **120**, 283 (1993).

[Naz05] A. V. Nazarov, M. L. Plumer, and B. B. Pant, J. Appl. Phys., **97**, 10N902 (2005).

[Nga06] T. N. Nga, N. E. Jenkins, and J. A. Marohn, IEEE Trans. Magn., **42**, 378 (2006).

[Oga98] S. B. Ogale, K. Ghosh, R. P. Sharma, R. L. Greene, R. Ramesh, and T. Venkatesan, Phys. Rev. B, **57**, 7823 (1998).

[Orl97] A. O. Orlov, I. Amlani, G. H. Bernstein, C. S. Lent, and G. L. Snider, Science, **277**, 928 (1997).

[Pan02] Q. Pan, T. G. Pokhil, and B. M. Moskowitz, J. Appl. Phys, **91**, 5945 (2002).

[Pan03] Q. A. Pankhurst, J. Connolly, S. K. Jone, and J. Dobson, J. Phys. D: Appl. Phys., **36**, R167 (2003).

[Par91] S. S. P. Parkin, Phys. Rev. Lett., **67**, 3598 (1991).

[Ped03] F. Pedreschi, J. M. Sturm, J. D. O'Mahony, and C. F. J. Flipse, J. Appl. Phys., **94**, 3446 (2003).

[Per03] J. M. Perez, J. Am. Chem. Soc., **125**, 10192 (2003).

[Pre80] D. Presti and J. D. Pettigrew, Nature, **285**, 99 (1980).

[Pro99] R. Proksch, P. Neilson, S. Austvold, and J. J. Schmidt, Appl. Phys. Lett., **74**, 1308 (1999).

[Psh00] A. F. Pshenichnikov and V. V. Mekhonoshin, J. Magn. Magn. Mater., **213**, 357 (2000).

[Qia99] C. X. Qian, H. C. Tong, F. H. Liu, X. Shi, S. Dey, R. B. Proksch, P. Nielson, and H. E. Hachfeld, IEEE Trans. Magn., **35**, 2625 (1999).

[Rad73] C. Radhakrishnamurthy, N. P. Sastry, and E. R. Deutsch, Pramana, **1**, 61 (1973).

[Rad08] G. Radu, D. Mautes, and U. Hartmann, Appl. Phys. Lett., **92**, 011928 (2008).

[Raj80] K. Raj and R. Moskowitz, IEEE Trans. Magn., **16**, 358 (1980).

[Ras02] M. Rasa, B. W. Kuipers, and A. P. Philipse, J. Coll. Int. Sci., **250**, 303 (2002).

[Ras06] S. Rast, U. Gysin, P. Ruff, C. Gerber, E. Meyer, and D. W. Lee, Nanotechnology, **17**, S189 (2006).

[Rit00] T. Ritz, S. Adem, and K. Schulten, Biophys. J., **78**, 707 (2000).

[Rit04] T. Ritz, P. Thalau, J. B. Phillips, R. Wiltschko, and W. Wiltschko, Nature, **429**, 177 (2004).

[Ros69] R. E. Rosensweig, R. Kaiser, and G. Miskolczy, J. Colloid Interface Sci., **29**, 680 (1969).

[Rug90] D. Rugar, H. J. Mamin, P. Guethner, S. E. Lambert, J. E. Stern, I. McFadyen, and T. Yogi, J. Appl. Phys., **68**, 1169 (1990).

[Rug92] D. Rugar, C. S. Yannoni, and J. A. Sidles, Nature, **360**, 563 (1992).

[Rug94] D. Rugar, O. Züger, S. Hoen, C. S. Yannoni, H. M. Vieth, and R. D. Kendrick, Science, **264**, 1560 (1994).

[Rug04] D. Rugar, R. Budakian, H. J. Mamin, and B. W. Chui, Nature, **430**, 329 (2004).

[Sae87] J. J. Saenz, N. Garcia, P. Grütter, E. Meyer, H. Heinzelmann, R. Wiesendanger, L. Rosenthaler, H. R. Hidber, and H. J. Güntherodt, J. Appl. Phys., **62**, 4293 (1987).

[Sai64] N. Saito, H. Fujiwara, and Y. Sugita, J. Phys. Soc. Jap., **19**, 1116 (1964).

[Sar94] Dror Sarid, *Scanning Force Microscopy with Applications to Electric, Magnetic and Atomic Forces*, Oxford University Press, Oxford, 1994.

[Sat96] A. Satoh, R. W. Chantrell, S. Kamiyama, and G. N. Coverdale, J. Magn. Magn. Mater., **154**, 183 (1996).

[Sch01] D. Schuh, J. Biberger, A. Bauer, W. Breuer, and D. Weiss, IEEE Trans. Magn., **37**, 2091 (2001).

[Sch99] D. Schüler and R. B. Frankel, Appl. Microbiol. Biotechnol., **52**, 464 (1999).

[Sel02] D. J. Sellmyer, C. P. Luo, Y. Qiang, and J. P. Liu, *Nanomaterials and Magnetic Thin Films*, edited by H. S. Nalwa, Handbook of Thin Film Materials, vol 5, Academic Press, San Diego, 2002.

[Shc99] V. P. Shcherbakov and M. Winklhofer, Eur. Biophys. J., **28**, 380 (1999).

[Shc05] D. Shcherbakov, M. Winkhofer, N. Petersen, J. Steidle, R. Hilbig, and M. Blum, Curr. Biol., **15**, R161 (2005).

[She85] J. P. Shepherd, R. Aragon, J. W. Koenitzer, and J. M. Honig, Phys. Rev. B, **32**, 1818 (1985).

[She01] L. Shen, A. Stachowiak, S. K. Fateen, P. E. Laibinis, and T. A. Hatton, Langmuir, **17**, 288 (2001).

[Shi92] H. Shinada, H. Suzuki, S. Sakaki, H. Todokoro, H. Takano, and K. Shiiki, IEEE Trans. Magn., **28**, 3117(1992).

[Shu75] R. T. Shuey, *Semiconducting ore minerals*, Elsevier, Amsterdam, 1975.

[Sid91] J. A. Sidles, Appl. Phys. Lett., **58**, 2854 (1991).

[Sid95] J. A. Sidles, J. L. Garbini, K. J. Bruland, D. Rugar, O. Z uger, S. Hoen, and C. S. Yannoni, Rev. Mod. Phys., **67**, 249 (1995).

[Smi59] J. Smit and H. P. J. Wijn, *Ferrites*, Philips Technical Library, Eindhoven, 1959.

[Sko98] R. Skomski, J. P. Liu, J. M. Meldrim, and D. J. Sellmyer, *Magnetic Anisotropy and Coercivity in Rare-Earth Transition Metal Alloys*, edited by L. Schultz and K.-H .Müller, Werkstoffinformationsgesellschaft, Frankfurt/M, 1998.

[Sko99] R. Skomski, J. P. Liu, and D. J. Sellmyer, Phys. Rev. B, **60**, 7359 (1999).

[Sne91] P. K. Sneed and T. L. Phillips, Oncology, **5**, 99 (1991).

[Sto48] E. C. Stoner and E. P. Wohlfarth, Phil. Trans. R. Soc. A, **240**, 599 (1948).

[Sto97] T. D. Stowe, K. Yasumura, T.W. Kenny, D. Botkin, K. Wago, and D. Rugar, Appl. Phys. Lett., **71**, 288 (1997).

[Str98] P. Strekeisen, S. Rast, C. Wattinger, E. Meyer, P. Vettiger, C. Gerber, and H. J. Güntherodt, Appl. Phys. A, **66**, S341 (1998).

[Sut04] A. Suter, Prog. in Nucl. Magn. Reson. Spect., **45**, 239 (2004).

[Sun08] J. B. Sun, F. Zhao, T. Tang, W. Jiang, J. S. Tian, Y. Li, and J. L. Li , Appl. Microbiol. Biotechnol. **79,** 389 (2008).

[Suz01] Y. Suzuki, Annu. Rev. Mater. Res., **31**, 265 (2001).

[Tak02] S. Taketomi and R. D. Shull, J. Appl. Phys., **91**, 8546 (2002).

[Tan69] Y. Tanaka and J. A. Berschauer, Stain Tech., **44**, 255 (1969).

[Tho80] R. Thompson, J. Bloemendal, J. A. Dearing, F. Oldfield, T. A. Rummery, J. C. Stober, and G. M. Turner, Science, **207**, 481 (1980).

[Var05] I. A. Vartanyants, I. K. Robinson, J. D. Onken, M. A. Pfeifer, G. J. Williams, F. Pfeiffer, H. Metzger, Z. Zhong, and G. Bauer, Phys. Rev. B, **71**, 245302 (2005).

[Ver39] E. J. W. Verwey, Nature, **144**, 327 (1939).

[Ver41] E. J. W. Verwey and P. W. Haayman, Physica, **9**, 979 (1941).

[Ver47] E. J. W. Verwey, P. W. Haayman, and F. C. Romeijan, J. Chem. Phys., **15**, 181 (1947).

[Ung82] J. Unguris, D. T. Pierce, A. Galejs, and R. J. Celotta, Phys. Rev. Lett., **49**, 72 (1982).

[Vee96] R. J. M. van de Veerdonk, M. A. M. Gijs, P. A. A. van der Heijden, R. M. Wolf, and W. J. M. de Jonge, Mat. Res. Soc. Symp. Proc., **401**, 455 (1996).

[Vol04] A. Volodin, D. Buntinx, S. Brems, and C. V. Haesendonck, Appl. Phys. Lett., **85**, 5935 (2004).

[Von66] S. V. Vonsovskij, *Feromagnetic resonance*, Pergamon, Oxford, 1966.

[Voo98a] F. C. Voogt, *NO_2 assisted Molecular Beam Epitaxy of Iron Oxide Films*, PhD-Thesis, the University of Groningen, The Netherlands, 1998.

[Voo98b] F. C. Voogt, T. T. M. Palstra, L. Niesen, O. C. Rogojanu, M. A. James, and T. Hibma, Phys. Rev. B., **57**, R8107 (1998).

[Voo99] F. C. Voogt, T. Fujii, P. J. M. Smulders, L. Niesen, M. A. James, and T. Hibma, Phys. Rev. B, **60**, 11193 (1999).

[Wag91] K. Wago, K. Sueoka, and F. Sai, IEEE Trans. Magn., **27**, 5178 (1991).

[Wag97] K. Wago, O. Züger, J. Wegener, R.K.C.S. Yannoni, and D. Rugar, Rev. Sci. Instrum., **68**, 1823 (1997).

[Waj00] E. Wajnberg, D. A. Avalos, L. J. E. Jaick, L. Abracado, J. L. A. Coelho, A. F. Bakuzis, P. C. Morais, and D. M. S. Esquivel, Biophys. J., **78**, 1018 (2000).

[Waj04] E. Wajnberg, G. Cernicchiaro, and D. M. de Souza Esquivel, BioMetals, **17** 467 (2004).

[Wal84] M. M. Walker, J. L. Kirschvink, S. B. Chang, and A. E. Dizon, science, **224**, 751 (1984).

[Wal97] M. M. Walker, C. E. Diebel, C. V. Haugh, P. M. Pankhurst, J. C. Montgomery, and C. R. Green, Nature, **390**, 371 (1997).

[Was73] P. J. Wasilewski, Earth Planet. Sci. Lett., **20**, 67 (1973).

[Wei04] B. P. Weiss, S. Kim, J. L. Kirschvink, R. E. Kopp, M. Sankaran, A. Kobayashi, and A. Komeili, Earth Planet. Sci. Lett., **224**, 73 (2004).

[Wei06] J. Wei, I. Knittel, U. Hartmann, Y. Zhou, S. Murphy, I. V. Shvets, and F. T. Park, Appl. Phys. Lett., **89**, 122517 (2006).

[Wer96] W. Wernsdorfer, D. Mailly, and A. Benoit, J. Appl. Phys., **87**, 5094 (1996).

[Wic00] H. K. Wickramasinghe, Acta Mater., **48**, 347 (2000).

[Wie90] R. Wiesendanger, H. J. Güntherodt, G. Güntherodt, R. J. Gambino, and R. Ruf, Phys. Rev. Lett. **65**, 247 (1990).

[Wie92] R. Wiesendanger and H. J. Güntherodt, *Scanning Tunneling Microscopy II*, *Springer Series Surface Sciences*, Vol. 28, Springer, Berlin Heidelberg, 1992.

[Wie93] R. Wiesendanger, J. Appl. Phys., **73**, 5816 (1993).

[Wil51] H. J. Williams, F. G. Foster, and E. A. Wood, Phys. Rev., **82**, 119 (1951).

[Win01] M. Winklhofer, E. H. Rötzler, M. Hanzlik, G. Fleissner, and N. Petersen, Eur. J. Mineral., **13**, 659 (2001).

[Wit99] J. Wittorn, K. V. Rao, R. Proksch, I. Revenko, E. D. Dahlberg, and D. A. Bazylinski, Nanostruct. Mater., **12**, 1149 (1999).

[Woh58] E. P. Wohlfarth, J. Appl. Phys., **35**, 595 (1958).

[Wor98] H. U. Worm, Geophys. J. Int. **133**, 201 (1998)

[Wyc82] R. W. G. Wyckoff, *Crystal Structures*, Krieger, Malabar, 1982.

[Yan84] A. Yanase and K. Siratori, J. Phys. Soc. Jap., **53**, 312 (1984).

[Yan99] A. Yanase and N. Hamada, J. Phys. Soc. Jap., **68**, 1607 (1999).

[Yaf86] Y. Yafet, J. Kwo, and E. M. Gyorgy, Phys. Rev. B, **33**, 6519 (1986).

[Yoz03] B. Yoza, A. Arakaki, and T. Matsunaga, J. Biotechnol., **101** 219 (2003).

[Zaa00] P. J. van der Zaag, P. J. H. Bloemen, J. M. Gaines, R. M. Wolf, P. A. A. van der Heijden , R. J. M. van de Veerdonk, and W. J. M. de Jonge, J. Magn. Magn. Mater., **211**, 301 (2000).

[Zah01] M. Zahn, J. Nanopart. Res., **3**, 73 (2001).

[Zho04] Y. Zhou, X. S. Jin, and I. V. Shvets, J. Appl. Phys., **95**, 7357 (2004).

[Zha96] Z. Zhang, P. C. Hammel, and P. E. Wigen, Appl. Phys. Lett., **68**, 2005 (1996).

[Zha98] Z. Zhang, P. C. Hammel, M. Midzor, M. L. Roukes, and J. R. Childress, Appl. Phys. Lett., **73**, 2036 (1998).

[Zha06] R. Zhang, X. Wang, C. Wu, M. Song, J. Li, G. Lv, J. Zhou, C. Chen, Y. Dai, F. Gao, D. Fu, X. Li, Z. Gua, and B. Chen, Nanotechnology, **17**, 3622 (2006).

[Zhu02] X. Zhu, P. Grütter, V. Metlushko, and B. Ilic, Appl. Phys. Lett., **80**, 4789 (2002).

[Zie00] M. Ziese and H. J. Blythe, J. Phys.: Condens. Matter, **12**, 13 (2000).

[Zie02] M. Ziese, R. Höhne, P. Esquinazi, and P. Busch, Phys. Rev. B, **66**, 134408 (2002).